

Electronic Thesis and Dissertation Repository

---

8-17-2015 12:00 AM

## Stochastic Stability and Uncertainty Quantification of Ring-based Vibratory Gyroscopes

Soroush Arghavan  
*The University of Western Ontario*

Supervisor  
Prof. Samuel F Asokanathan  
*The University of Western Ontario*

Graduate Program in Mechanical and Materials Engineering  
A thesis submitted in partial fulfillment of the requirements for the degree in Master of Engineering Science  
© Soroush Arghavan 2015

Follow this and additional works at: <https://ir.lib.uwo.ca/etd>



Part of the [Computational Engineering Commons](#), and the [Electro-Mechanical Systems Commons](#)

---

### Recommended Citation

Arghavan, Soroush, "Stochastic Stability and Uncertainty Quantification of Ring-based Vibratory Gyroscopes" (2015). *Electronic Thesis and Dissertation Repository*. 2986.  
<https://ir.lib.uwo.ca/etd/2986>

This Dissertation/Thesis is brought to you for free and open access by Scholarship@Western. It has been accepted for inclusion in Electronic Thesis and Dissertation Repository by an authorized administrator of Scholarship@Western. For more information, please contact [wlsadmin@uwo.ca](mailto:wlsadmin@uwo.ca).

STOCHASTIC STABILITY AND UNCERTAINTY QUANTIFICATION OF  
RING-BASED VIBRATORY GYROSCOPES

(Thesis format: Monograph)

by

Soroush Arghavan

Graduate Program in Mechanical and Materials Engineering

A thesis submitted in partial fulfillment  
of the requirements for the degree of  
Masters of Engineering Science

The School of Graduate and Postdoctoral Studies

The University of Western Ontario

London, Ontario, Canada

© Soroush Arghavan 2015

## Abstract

Effect of stochastic fluctuations in angular velocity on the stability of two DOF ring-type MEMS gyroscopes is investigated. The governing Stochastic Differential Equations are discretized using the higher-order Milstein scheme in order to numerically predict the system response assuming the fluctuations to be white noise. Simulations via Euler scheme as well as a measure of Largest Lyapunov Exponents are employed for validation purposes due to lack of similar analytical or experimental data. The stability investigation predicts that the threshold fluctuation intensity increases nonlinearly with damping ratio. Under typical gyroscope operating conditions, nominal input angular velocity magnitude and mass mismatch appear to have minimal influence on system stability.

Furthermore, construction, electrical improvements, testing and troubleshooting of a macro-scale ring-type gyroscope prototype is completed. Experiments have been conducted in order to investigate the linearity of system response, system behavior when subjected to environmental fluctuation in angular rate as well as the effects of angular rate and mass mismatch on system natural frequency. It is shown that the system natural frequency decreases with input angular rate and mass mismatch. It is also revealed that the system exhibits a more efficient damping behavior when subjected to stochastic speed fluctuations with fixed intensity at higher input angular rates.

**Keywords:** MEMS, gyroscope, stochastic differential equation, dynamic stability, white noise.

## **Acknowledgements**

I am forever in debt to my supervisor Professor Samuel F. Asokanthan who kindly provided me with guidance in the arduous path of research and introducing me to an exciting research field. I owe my knowledge to him and I thank him for helping me in this thesis which was made possible through him.

I would also like to thank the National Sciences and Engineering Research Council (NSERC) of Canada Discovery Grant and The University of Western Ontario for the Western Graduate Research Scholarship (WGRS) for supporting this thesis.

*To my lovely mother Hangameh,  
my caring father Mohammadhassan  
and my wise and motivating brother Sina.*

*I would not have been here without your love and support.*

*I have been blessed with the gift of a cherished family.*

# Contents

<b>Acknowledgements</b>	<b>iii</b>
<b>List of Figures</b>	<b>viii</b>
<b>List of Tables</b>	<b>x</b>
<b>Nomenclature</b>	<b>xi</b>
<b>1 Introduction and Literature Survey</b>	<b>1</b>
1.1 Introduction . . . . .	1
1.2 Literature Review . . . . .	2
1.2.1 A Short History of Gyroscopes . . . . .	2
1.2.2 Vibrating String . . . . .	5
1.2.3 Mass-Spring . . . . .	5
1.2.4 Tuning Fork . . . . .	6
1.2.5 Vibrating Shell . . . . .	6
1.2.6 Ring-type . . . . .	7
1.3 Thesis Objectives . . . . .	13
1.4 Thesis Outline . . . . .	14
<b>2 Governing Equations</b>	<b>16</b>
2.1 Introduction . . . . .	16
2.2 Model Description . . . . .	16
2.3 Governing Equations . . . . .	18

2.4	Natural Frequency Variations . . . . .	22
2.5	Closure . . . . .	23
<b>3</b>	<b>Stochastic Model Incorporating Uncertainty in Input Angular Rate</b>	<b>25</b>
3.1	Introduction . . . . .	25
3.2	Gaussian White Noise . . . . .	26
3.2.1	Stochastic Calculus . . . . .	26
3.3	Stochastic Fluctuation in Angular Rate . . . . .	27
3.4	Itô-Taylor Expansion . . . . .	30
3.5	Lyapunov Characteristic Exponent . . . . .	34
3.6	Closure . . . . .	35
<b>4</b>	<b>Stability Analysis Using Numerical Methods</b>	<b>36</b>
4.1	Introduction . . . . .	36
4.2	Numerical Predictions . . . . .	37
4.3	Parametric Study . . . . .	42
4.4	Closure . . . . .	44
<b>5</b>	<b>Experimental Results</b>	<b>46</b>
5.1	Introduction . . . . .	46
5.2	Experimental Setup . . . . .	47
5.3	Experimental Results and Discussion . . . . .	53
5.4	Stochastic Fluctuation in Angular Rate . . . . .	61
5.5	Closure . . . . .	64
<b>6</b>	<b>Conclusion</b>	<b>65</b>
6.1	Thesis Contributions . . . . .	66
6.2	Recommendations for Future Research . . . . .	67
	<b>Bibliography</b>	<b>69</b>

<b>A</b>	<b>Derivation of Equations of Motion</b>	<b>74</b>
A.1	Introduction . . . . .	74
A.2	Energy Equations . . . . .	74
A.3	Natural Frequencies . . . . .	76
A.4	Normalized Equations of Motion . . . . .	78
<b>B</b>	<b>Matlab Codes</b>	<b>81</b>
B.1	Introduction . . . . .	81
B.2	Time Series Simulation . . . . .	81
B.3	Largest Lyapunov Exponent Calculation . . . . .	85
B.3.1	Calculating Mutual Average Information . . . . .	85
B.3.2	Calculating Mean Period . . . . .	87
B.3.3	Calculating Lyapunov Exponents . . . . .	88
B.3.4	Finding Largest Lyapunov Exponent of The Simulated Time Series . . . . .	90
<b>C</b>	<b>Experimental Setup</b>	<b>92</b>
C.1	Startup Procedure . . . . .	95
C.1.1	Rate Table Initial Startup . . . . .	96
C.2	Shutdown Procedure . . . . .	98
	<b>Curriculum Vitae</b>	<b>108</b>



# List of Figures

1.1	A simple gyroscope. (Scarborough, 1958) . . . . .	3
1.2	Schematics of a spring-mass type gyroscope (Reproduced from Clark, 1999) . . . . .	6
1.3	SEM view of a tuning fork gyroscope. (Günthner et al., 2006) . . . . .	7
1.4	SEM view of a polysilicon ring gyroscope 1 mm in diameter. (Ayazi and Najafi, 1998) . . . . .	8
1.5	Schematic of a BAW inertial sensor. (Kempe, 2011) . . . . .	10
2.1	Schematic of the rotating ring geometry. (Cho, 2005) . . . . .	17
2.2	Visualization of the second flexural modes of the ring. (Cho, 2005) . . . . .	17
2.3	Variation of natural frequencies with angular rate with non-uniform mass assumption. (Cho, 2005) . . . . .	23
4.1	Example of stable time response. . . . .	37
4.2	Example of marginally stable time response. . . . .	39
4.3	Example of unstable time response. . . . .	39
4.4	Under-prediction of results by Euler scheme in a marginally stable case. . . . .	40
4.5	Under-prediction of results by Euler scheme in a marginally unstable case. . . . .	41
4.6	Stability boundary in the $\mu$ - $\zeta$ space ( $\Omega = 2\pi$ rad/s). . . . .	43
5.1	Experimental setup . . . . .	48
5.2	Configuration of an electromagnetic exciter. . . . .	49
5.3	Configuration of the Eddy-Current probes. . . . .	49
5.4	Schematic location of sensors and actuators. . . . .	50

5.5	Implementation of stochastic angular rate fluctuation setup. . . . .	51
5.6	Block diagram representation of the experimental setup. . . . .	52
5.7	Schematic representation of the experimental setup. . . . .	53
5.8	Natural frequency shift in the Cross Spectrum Magnitude diagram due to an- gular rotation. . . . .	54
5.9	Linearity of nodal and anti-nodal measurements. . . . .	55
5.10	Suggested locations for mass anomaly. . . . .	56
5.11	Anti-nodal measurements of time response for 2.5% mass mismatch located at points 1 to 3. . . . .	57
5.12	Anti-nodal measurements of time response for 2.5% mass mismatch located at points 4 to 6. . . . .	58
5.13	Nodal measurements of time response for 2.5% mass mismatch. . . . .	58
5.14	Variation of natural frequency with mass mismatch - experimental results. . . .	59
5.15	Effects of fluctuations in angular rate on raw sensor measurements, $\Omega = 0$ rad/s.	61
5.16	Effects of fluctuations in angular rate on raw sensor measurements, $\Omega = 2\pi$ rad/s.	62
5.17	Variation of output standard deviation with angular rate. . . . .	63
C.1	Experimental setup. . . . .	92
C.2	Experimental setup close-up . . . . .	93
C.3	Configuration of an electromagnetic exciter. . . . .	94
C.4	Configuration of the Eddy-Current probes. . . . .	94
C.5	Layout of a junction box. . . . .	95
C.6	Block diagram representation of the experimental setup. . . . .	99
C.7	Schematic view of the experimental setup. . . . .	100
C.8	Wiring diagram for single sensor operation. . . . .	101
C.9	Wiring diagram for dual sensor operation. . . . .	102
C.10	Front panel of the LabView script. . . . .	106
C.11	Block diagram view of the LabView script. . . . .	107

# List of Tables

1.1	Grade requirements of gyroscopes (Yazdi et al., 1998)	4
1.2	Applications of gyroscopes with estimated typical grades	9
2.1	Physical properties of the MEMS ring	22
4.1	Summary of LLE values for predicted time responses.	42
4.2	Variation of system natural frequencies with input angular rate.	44
4.3	Variation of system natural frequencies with mass mismatch.	44
5.1	Physical properties of the experimental ring	48
5.2	Summary of measurements with concentrated mass located at different points on the ring.	60
C.1	Input 37-pin connection pinout (Rate table J100 and J101)	103
C.2	Output 37-pin connection pinout (Rate table J102 and J103)	104
C.3	ECL134 15-pin output connection pinout	105

# Nomenclature

$\alpha$  Rotational coordinate

$\delta m$  Mass mismatch

$\delta(t)$  Dirac's delta function

$\gamma$  Ring model constant

$\kappa_1$  Ring model constant

$\kappa_2$  Ring model constant

**M** Mass matrix

**q** Flexural generalized coordinate vector

$\mu$  Relative noise intensity measure

$\mu_0$  White noise intensity

$\Omega$  Angular rate

$\omega$  Frequency, Excitation frequency

$\omega_{01}$  Natural frequency of the first degenerate configuration of the second flexural mode shape

$\omega_{02}$	Natural frequency of the second degenerate configuration of the second flexural mode shape
$\Phi$	Variable space
$\rho$	Density
$\sigma$	Stress component
$\sigma_a$	Averaged standard deviation
$\mathbf{v}$	Velocity vector
$\varepsilon$	Strain component
$\xi$	White noise
$\zeta$	Damping ratio
$A$	Cross-section area
$a[X(t)]$	Drift coefficient
$b$	Axial thickness
$b[X(t)]$	Diffusion coefficient
$D$	Damping matrix
$d$	Number of dimensions in Milstein scheme
$E$	Young's elasticity modulus
$F$	Generalized excitation force vector
$f$	External force component
$f_1$	Excitation force amplitude

$G$	Gyroscopic matrix
$h$	Radial thickness
$I$	Mass moment of inertia
$K$	Stiffness matrix
$k$	Stiffness component
$m$	Number of independent Wiener processes
$N$	Normal distribution
$n$	Mode shape number
$O$	Terms in the order of $\delta t^{3/2}$ or higher
$q$	Flexural generalized coordinate
$r$	Mean radius
$S$	Power spectral density function
$T$	Time interval
$u$	Displacement
$W$	Brownian motion, Wiener process
$X$	Stochastic process

# Chapter 1

## Introduction and Literature Survey

### 1.1 Introduction

The ancient civilizations designed a simple toy called a "top" for the sole purpose of entertainment, unaware of the applications of the device in the millennia to come. The invention of the spinning top opened the door to exquisite, then unimaginable advancements in low-cost high-accuracy navigation devices used worldwide in a diverse list of applications from long-haul transportation to entertainment. A wide variety of gyroscopic devices have been developed in the past century in order to quantify rotation and, essentially, simplify navigation.

In the past two decades, the world of Micro Electro-Mechanical Systems (MEMS) offered unprecedented opportunities in reducing the weight, size, production cost and power consumption of the sensors as well as increasing their accuracy in by omitting unnecessary moving parts and fluids. It was only logical that MEMS methods were applied to gyroscopes and gave birth to a new range of navigation devices. Although these devices offer countless possibilities, they are still prone to sources of error such as drift, effects of temperature change and unwanted vibration.

The present thesis is a continuation of ongoing research at the Dynamics and Sensing Systems

Laboratory at Western University and focuses on a modern type of MEMS gyroscopes called the ring-type gyroscopes. In an effort to model and study the effects of environmental fluctuations in angular rate of ring gyroscopes, stochastic methods are utilized and integrated using numerical methods.

Although ring-type gyroscopes have been studied and manufactured in MEMS scale, more research needs to be done on the behavior of MEMS and macro-scale ring-type gyroscopes and problems associated with this class of devices. For this purpose, an experimental macro-scale prototype previously developed by Cho (2009) has been completed and complementary experiments were conducted in order to visualize the behavior of the device and the effects of low natural frequencies associated with such macro-scale devices.

## **1.2 Literature Review**

### **1.2.1 A Short History of Gyroscopes**

Beginning in the 18th and early 19th centuries, explorers required a device for measurement of horizon and direction regardless of the orientation of the surface it was placed on. The English scientist, John Serson (in 1742 or 1743) was one of the first to notice that spinning tops tend to remain level regardless of the supporting surface being tilted. He suggested that the top has the potential to be used as artificial horizon on ships. Modern gyroscopes are, in essence, modified tops. The first known prototype of modern gyroscopes was introduced by G. C. Bohnenberger in 1810. His prototype, however, consisted of a heavy ball instead of a wheel and hence was not credited by the scientific community due to its limited applications (Wagner, 2005).

In 1852, Foucault who was experimenting with the effects of earth rotation on pendulums, constructed a device consisting of a high-speed rotating wheel which could move independently with respect to a supporting rigid gimbal based on previous work by Bohnenberger (1810,



Germany) and Johnson (1832, United States). The orientation of the wheel stayed consistent, therefore confirming that the Earth is rotating constantly since the supporting gimbal is directly connected to the Earth (Foucault, 1852). The device acquired the name "gyroscope", from the Greek words "gyros" (revolution) and "skopein" (to see); a device that allows the user to see the revolution of the Earth. Although the word "gyroscope" is used by some authors exclusively for rotary sensors with spinning wheels, it can be generally used for any device that is used to demonstrate or measure rotation (Lawrence, 1993). George M. Hopking, American inventor, employed an electric motor to maintain the angular velocity of the wheel at any desired speed in 1878. An example of this type of gyroscopes can be seen in Figure 1.1. In 1898, Ludwig Obry patented a torpedo steering mechanism that operated based on gyroscopic inertia which might have inspired Elmer A. Sperry, who developed the first automatic airplane pilot using gyroscopes and the first gyro-stabilizer for reducing roll in ships (see Lawrence, 1993; Scarborough, 1958).



Figure 1.1: A simple gyroscope. (Scarborough, 1958)

Gyroscopes can generally be categorized into three grades based on their accuracy and perfor-

mance, namely rate, tactical and inertial grade, where the inertial grade provides the highest accuracy possible while the rate grade is used for low-accuracy demanding applications. Table 1.1 displays the different grades of gyroscopes and the requirements that need to be met for categorizing a device under each grade.

Specification	Rate Grade	Tactical Grade	Inertial Grade
Angle Random Walk (deg / $\sqrt{hr}$ )	>0.5	0.5~0.05	<0.001
Bias Drift (deg /hr)	10~1000	0.1~10	<0.01
Full Scale Range (deg /s)	50~1000	>500	>400
Dynamic Range (dB)	40	100	100
Noise (deg /s. $\sqrt{Hz}$ )	>0.1	0.5~0.05	<0.001
Absolute Accuracy (%)	0.1~1	0.01~0.1	<0.001
Bandwidth (Hz)	>70	~100	~100

Table 1.1: Grade requirements of gyroscopes (Yazdi et al., 1998)

The most usual form of a gyroscope was a mechanical device consisting of a heavy flywheel rotating at high speeds until mid 1950s. These types of gyroscopes formed the majority of navigation devices in vessels (Kempe, 2011; Scarborough, 1958). New types of gyroscopes emerged beginning in the 1950s with the introduction of the Sperry rate Gyrotron (Morrow, 1955) opening the way to new classes of angular rate measurement devices that would not fit under the conventional definition of a gyroscope. Various types of gyroscopes have been developed ever since for specific range of applications, such as angle and angular rate measurement, remote sensing, photogrammetry, terrestrial surveying and terrain profiling (Jekeli, 2001). In 1963, a new class of gyroscopes were born with the introduction of Ring Laser Gyroscopes (RLG) and Fiber Optic Gyroscopes (FOG). This class of gyroscopes which take advantage of the phase shift of light beams, commonly known as the Sagnac effect, are able to measure angular rate with exceptionally high accuracy and form the majority of inertial grade gyroscopes (Loukianov et al., 1999).

At the same time, another class of gyroscopes were being developed which took advantage of Coriolis effect in a different way in order to measure angular velocity. This class, commonly

referred to as vibratory gyroscopes have been developed in pursuit of reducing the production cost and size of the sensors. However they did not attract the attention of the scientific community until the rise of MEMS devices due to apparent lack of advantages over conventional gyros. With the introduction of MEMS devices, a unique characteristic of the vibratory gyros gave popularity to these sensors which is feasibility of production in micro-scale. Ever since, vibratory angular rate sensors have been the focus of researchers with the hope to develop more cost-effective and accurate devices. This research has led to development of several types of vibratory gyros including the vibrating string, mass-spring and vibrating shell resonator gyroscopes which currently fall under the rate or tactical grade accuracy classification.

### **1.2.2 Vibrating String**

The vibrating string gyro, as the name suggests, consists of an oscillating string. The string is fixed on both ends and the vibration plane of the string tends to remain stationary in case the supports rotate about the string axis (Quick, 1964). Quick, in 1964, realized that the Coriolis acceleration causes the vibration to be coupled into the plane perpendicular to the vibration plane and hence the vibration plane appears to not be affected by the rotation. Quick designed an apparatus which measures the coupling due to rotation and essentially acts as an angular measurement sensor.

### **1.2.3 Mass-Spring**

This type of gyroscopes usually contains a proof mass oscillating along the  $X$ -axis using a driving force ( $F_D$ ) with the frame free to rotate about the  $Z$ -axis as shown in Figure 1.2. Coriolis force  $F_C$ , due to rotation combined with oscillation results in deflection of the proof mass in the  $Y$ -axis. The Coriolis acceleration and deflection in the  $Y$ -axis can then be used in order to measure the angular velocity about the  $Z$ -axis.

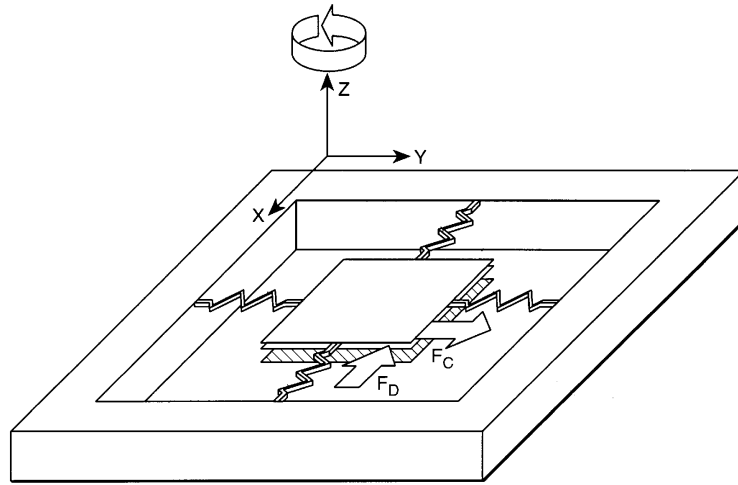


Figure 1.2: Schematics of a spring-mass type gyroscope (Reproduced from Clark, 1999)

### 1.2.4 Tuning Fork

Rotation of a vibrating tuning fork about its base produces periodically varying Coriolis forces along the rotation axis. The variations in the angular rate can be qualitatively explained through conservation of angular momentum with the fork rotating more rapidly when the tines are closer to each other and the fork rotating more slowly when the tines are apart (Morrow, 1955). Hence, forcing the fork to rotate about its axis at a steady speed results in the varying motion of the tines which can be calibrated against the angular speed of the base. An example of a MEMS tuning fork gyroscope under a Scanning Electron Microscope (SEM) is shown in Figure 1.3.

### 1.2.5 Vibrating Shell

The tuning fork gyros operate using energy transfer between two different vibration modes. Therefore, this type of gyroscopes is highly sensitive to environment temperature due to differ-

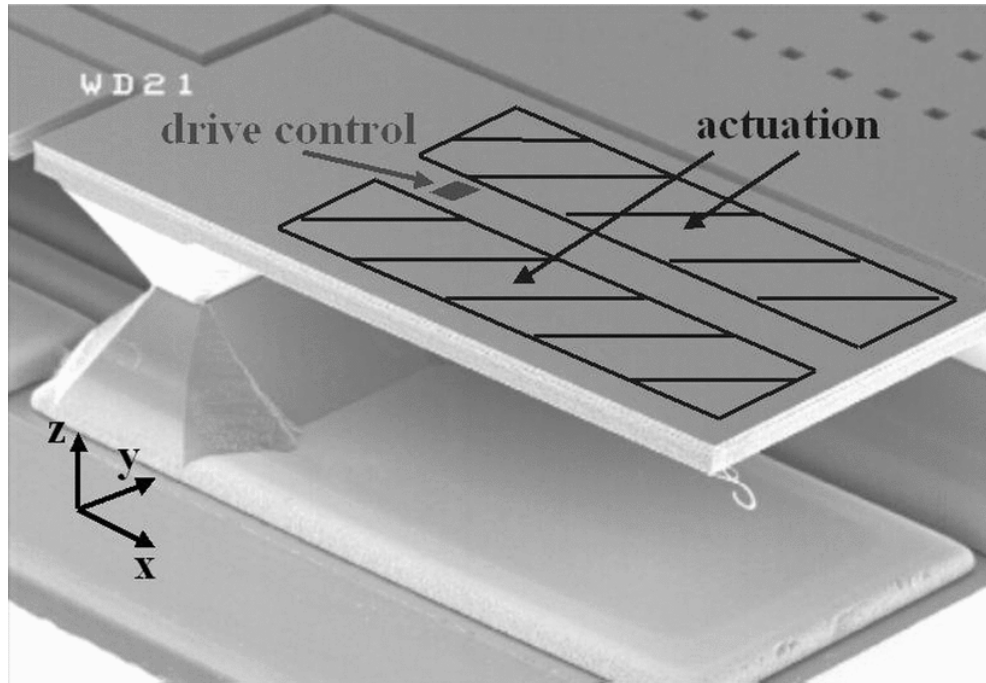


Figure 1.3: SEM view of a tuning fork gyroscope. (Günthner et al., 2006)

ent temperature sensitivities of the natural frequencies of the two modes. Vibrating shell gyroscopes, however, overcome this problem by taking advantage of two identical mode shapes. Bryan (1890) analyzed the vibration of cylindrical and bell-shaped shells using a wine glass analogy. Bryan noted that a wine glass produces a pure and continuous tone when struck. However, twisting the wine glass around results in audible beats demonstrating that the nodal meridians do not remain fixed in space. Furthermore, Bryan concludes that since the beats can still be heard with the observer turning around while holding the vibrating glass, the nodes do not rotate with the same angular velocity as the glass or the observer.

### 1.2.6 Ring-type

Ring-type or ring-structure gyroscopes operate similar to vibrating shell gyros. Ring-type gyroscopes were first developed by Delco Electronics Corporation and British Aerospace Systems incorporating a batch-manufactured silicon ring held in place by eight spider-leg spring sus-

penders (Maluf and Williams, 2004). This type of gyros gained popularity for their minimal drift to temperature fluctuation and high sensitivity to rotation. Moreover ring-type and in general the vibrating shells gyros exhibit higher immunity to unwanted environment vibration as opposed to e.g., tuning forks due to their weak interaction with the supporting structure (see Asokanthan et al., 2006; Lawrence, 1993).

Ring-type vibratory gyroscopes rely on Coriolis effect for operation similar to other types of modern angular rate sensors with the exception of ring-laser sensors. A ring-type angular rate sensor is usually composed of a thin, light-weight ring, an exciter and a sensor. An example of a MEMS ring gyroscope can be seen in Figure 1.4. Vibration in a certain vibratory mode is excited in the ring using an exciter. Coriolis forces induced in the ring during rotation of the ring cause the excited ring to shift vibration into the next resonance mode. A well-placed sensor is able to detect the resultant shift and the sensor output is then calibrated against the rotation (Kempe, 2011).

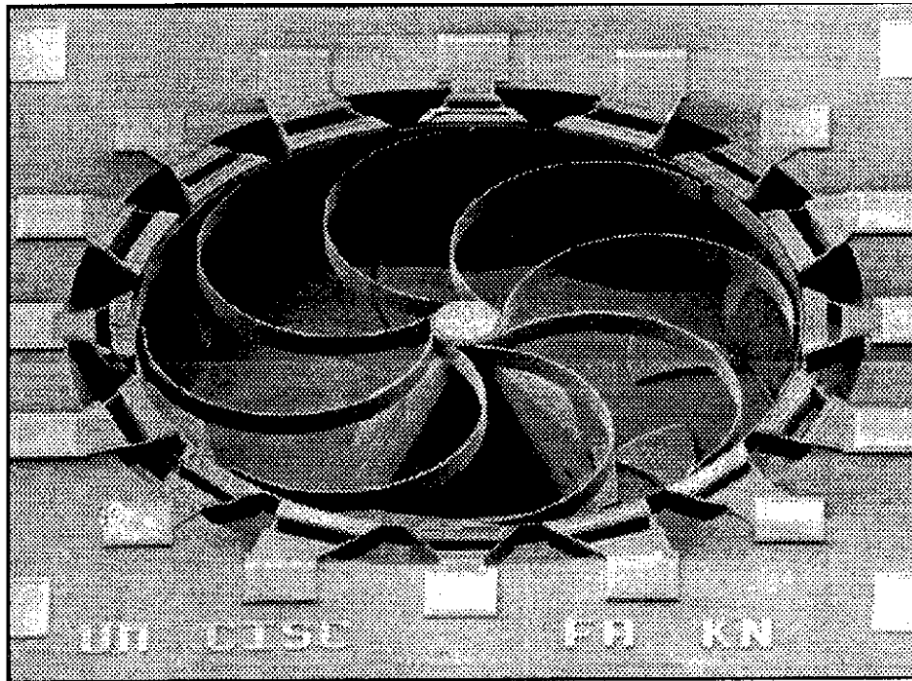


Figure 1.4: SEM view of a polysilicon ring gyroscope 1 mm in diameter. (Ayazi and Najafi, 1998)

More recently, the advancements in the fields of micro-machining and Micro Electro-Mechanical Systems (MEMS) have enabled development of gyroscopes and accelerometers in a small package. Low power consumption, small size, low manufacturing cost as well as moderate accuracy are the main advantages offered by MEMS angular rates sensors which makes them ideal for usage in everyday and practical applications. MEMS packages are used nowadays in vehicles for applications such as designing active suspension and navigation, in cameras for image stabilization and in consumer electronics (such as smartphones) for a range of application from navigation to entertainment (Abedin, 2014). Table 1.2 shows the typical applications of a MEMS inertial sensor with the estimated grade requirements (Söderkvist, 1994; Yates, 1999).

Application	Range	Accuracy	Grade
Automotive Safety	50 ~ 200°/s	1 ~ 10°/s	Rate
Consumer	50 ~ 100°/s	0.5 ~ 2°/s	Rate
Medical	20 ~ 100°/s	0.1 ~ 2°/s	Rate/Tactical
Industrial	10 ~ 50°/s	0.01 ~ 0.2°/s	Tactical

Table 1.2: Applications of gyroscopes with estimated typical grades

MEMS-based sensors primarily fall in the rate grade. Improvements in accuracy as well as their drift performance are warranted before they can be accepted as a true tactical or inertial grade device. To this end, several recent research as well as development efforts are underway. In the recent years, another type of sensors similar to ring gyroscopes called the Bulk Acoustic Wave (BAW) inertial sensors have been developed by Ayazi and Johari (2009) and currently in production by Qualtré Inc. BAW sensors are composed of a silicon disk which is manufactured in the HARPSS process and detect energy transfer as a result of rotation between two modes of high frequency (1 to 5 MHz) of the disk. BAW sensors offer full-scale ranges of 300 ~ 3000 °/s as well as temperature sensitivities as low as 0.05 °/s/°C. A schematic of a BAW inertial sensor is displayed in Figure 1.5, showing the vibration modes of the disk as well as the sensing and actuation devices.

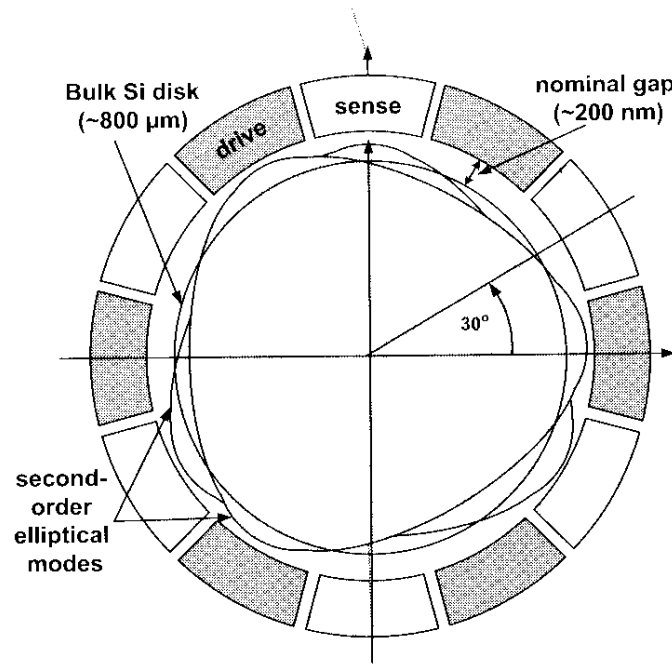


Figure 1.5: Schematic of a BAW inertial sensor. (Kempe, 2011)

Although the operating principles of the ring-type gyroscopes are fairly simple, complication might arise during typical manufacturing and operating conditions. Stability of the sensor is compromised when the device is subjected to disturbance caused by environmental fluctuations. Furthermore, development of a perfectly uniform ring is improbable resulting in non-uniform mass distribution of the ring, called mass mismatch. Introduction of mass mismatch affects the natural frequencies of the ring and essentially the operation as well as accuracy of the gyroscope. Hence, the main objective of the present thesis is assessment of dynamic stability of MEMS-based ring-type vibratory gyroscopes under external disturbance as well as design and production of a macro-scaled prototype for the purposes of studying the physical and vibratory characteristics as well as the general behavior of the device.

To Further this development, dynamics and stability of ring-structure gyroscopes have been of interest in the recent past. In-plane motion of vibrating rings considering the effects of both centrifugal and Coriolis forces on the dynamic response has been investigated in (see Huang and Soedel, 1987). Moreover, the coupling between the in-plane and out-of-plane vibratory



motion was studied by Eley et al. (2000). Focusing on the system stability, a method for investigating the stability of a linear gyroscopic system via a model of a rotating beam has been developed by Kammer and Schlack Jr. (1987). Recently, stability of a ring-based gyroscope when it is subjected to harmonic perturbation in angular rate has been studied via the method of averaging (Asokanathan and Cho, 2006). Although harmonic vibration may be a simple approximation useful for modeling angular speed fluctuation emanating from the environment, white noise, which covers a wide range of frequencies, may be a more realistic representation. Hence, introduction of the white noise is envisaged to aid in a more accurate prediction of the dynamic behavior of these devices as well as the physical systems they are mounted on. Asokanathan and Wang (2009) studied the effects of angular rate perturbations on mass spring systems using the second moment stability criteria and the method of averaging. The present investigation focuses on the dynamic stability of ring-structure gyroscopes based on their dynamic response, considering random perturbation in input angular velocity.

One of the most important factors that affect the operation of a ring gyroscope is deviation of the geometry from the intended axisymmetric design. Imperfections could occur mostly during the manufacturing stage. Non-uniformities in mass result in high levels of mechanical coupling and reduced secondary response which in return limits detection of low angular rates. To this end, previous research has shown that near-perfect aspect ratios are achieved using deep reactive ion etching as well as finer line photolithography is the fabrication process of silicon rings (Harris et al., 1998).

In another effort to increase the accuracy of ring gyroscopes Wang et al. (2010) designed and fabricated a sensor with harsh environmental conditions in mind. The final product demonstrated a low frequency split of 0.5 Hz between the sensing mode and driving mode frequencies due to high symmetry. Furthermore, it was shown that the frequency split remains consistent under different environmental conditions.

The present thesis consists of two parts. The first part focuses on studying the effects of envi-

ronmental fluctuations on ring-type gyroscopes through numerical simulation. The developed schemes take advantage of the equations of motion for the ring-type gyroscopes which have been developed by Asokanthan and Cho (2006) based on the previous work by Huang and Soedel (1987). The present study further extends the work performed by Asokanthan and Cho (2006) for the periodic fluctuation by introducing a random perturbation in the angular rate. For this purpose, considering the random fluctuation, the governing equations that represent the motion of the gyroscopic system under investigation are written in the form of a system of standard Stochastic Differential Equations (SDE).

It is known that closed-form analytical solutions cannot be obtained for this class of systems owing to their highly non-differentiable character of the realization of the Wiener process (Higham, 2001). In the present study, the higher-order Milstein scheme is employed to simulate the time response. The stochastic response of ring-based gyroscopes is then quantified for certain parameters of interest. The stability analysis is then performed based on the simulated responses so that the stability behavior of this class of gyroscopes can be predicted. To this end, an algorithm for computing the characteristic Lyapunov exponents of the response have been employed for validating the stability predictions via the stochastic response. Effects of damping and angular speed fluctuation magnitude on system stability have been quantified for different input angular velocities. In addition, these effects have also been quantified for a parameter that represents the non-uniformity in ring mass distribution.

The objective of the second part of the present thesis is further investigation of the results obtained through numerical and analytical studies as well as the non-linearities of macro-scale ring-type gyroscopes. A macro-scale experimental setup was developed for this purpose and studies were performed in order to quantify the energy transfer between different mode shape configurations and assess the effects of angular rotation on the natural frequency of the ring. Furthermore, the effects of non-uniform mass distribution along the circumference of the ring as well as effects of fluctuations in input angular rate on system behavior have been quantified.

### 1.3 Thesis Objectives

Although vibratory sensors are manufactured for common applications in MEMS-scale, it is not feasible to study the effects of environmental fluctuations on a MEMS-scale sensor due to the complexities of changing the geometry of the ring as well as selection of suitable measurement devices for a rotating MEMS ring. Moreover, numerical simulation of such devices poses another problem due to the barriers caused by the limitations of analytical and numerical methods. Considering the problem in hand, the present thesis aims to:

- Introduce environmental fluctuations in the input angular rate of ring-type vibratory gyroscopes by employing a white noise function and develop the corresponding stochastic differential equations of motion considering the newly introduced noise intensity variable.
- Develop the required numerical tools using the available schemes in order to numerically solve the resulting SDE and apply the developed scheme to the SDE. For this purpose, the goal is to employ the higher-order available schemes in order to obtain a novel method with higher accuracy than the simpler schemes and to implement the developed higher-order numerical equations using a Matlab script and validate the results against the commonly-used schemes using Largest Lyapunov Exponents stability assessment tools.
- Perform a dynamic stability analysis using the developed script and study the effects of fluctuations in angular rate on system stability via a parametric study using an array of noise intensity and damping ratio values in order to obtain a noise intensity threshold for a prescribed system damping ratio. Further research is also envisioned in order to assess the effects of angular rate and decreased uniformity of mass along the circumference of the ring on bifurcation of system natural frequencies and essentially, system stability.

- Develop a macro-scale ring-type vibratory sensor prototype using the experimental project previously initiated by Cho (2009). The project agenda includes development of reliable wiring of the device, installation and testing of sensors, development of a LabView script for data acquisition, monitoring and analysis, development of an instruction manual for safe operation and maintenance of the device as well as implementation of safety measure to ensure safe operation of the experimental setup.
- Conduct experiments on the bifurcation of natural frequencies of a ring-type gyroscope and demonstrate the reduction of natural frequency due to angular rotation as well as the non-linear behavior of the macro-scale device as a result of large-amplitude vibrations and relatively low natural frequency close to operating angular rates.
- Investigate the effect of increased non-uniform mass distribution due to manufacturing defects on natural frequencies of the system and compare the results with previous theoretical analysis in literature. Furthermore, the goal is to demonstrate the effects of fluctuations in angular rate on system behavior which can be used to further the experimental research into dynamic stability of macro-scale systems similar to the numerical study performed in the present thesis.

## 1.4 Thesis Outline

The present thesis is comprised of a numerical and an experimental study on the behavior of ring-type gyroscopes. Conforming to the objectives of the thesis, the thesis is presented in the following chapters:

In *Chapter 2*, the previously obtained equations of motion for the ring-type sensors are further developed in order to incorporate the effects of fluctuations in angular velocity. Furthermore, the equations are simplified and rewritten in order to take the form of standard Stochastic

Differential Equations.

*Chapter 3* reviews the stochastic calculus tools required in order to numerically solve the developed equations. Moreover, the common numerical schemes are introduced, explained and compared and the higher-order Milstein numerical scheme is applied to the stochastic differential equation at hand.

The results of the numerical study are discussed in *Chapter 4*. This chapter starts by validating the developed method using Largest Lyapunov Exponent method and comparing the method with the more commonly used Euler method. Times responses obtained using the Milstein method are analyzed and a parametrical study is performed in order to obtain an intensity threshold for fluctuations in angular rate using a prescribed system damping ratio. Effects of angular rate and mass uniformity on system natural frequencies are also discussed in *Chapter 4* and the discussion on the findings is ensued.

The details of the experimental setup are discussed in *Chapter 5* as well as the experimental results on effects of angular rate, environmental fluctuations and mass uniformity on system natural frequency.

Finally, *Chapter 6* discusses the conclusion of the obtained numerical and experimental results as well as a summary of the developed numerical and experimental tools employed in the research. Contributions of the present work are also highlighted in this chapter and recommendations for future research are explored.

# Chapter 2

## Governing Equations

### 2.1 Introduction

The governing equations for the system developed using Hamilton's principle by Cho (2005) have been employed to study the effect of stochastic fluctuation in input angular rate. Complex Fourier series are then used to derive the modal shapes of the ring. In this chapter, the employed model is reviewed in order to better understand the experiments and implementation of the numerical models.

### 2.2 Model Description

The ring is assumed to be of uniform rectangular cross section of width  $b$  and sufficiently thin with the ratio of radial thickness  $h$  to mean radius  $r$ , i.e.,  $(h/r)^2 \ll 1$  (see Love, 2013). The material chosen for the ring is assumed to be isotropic and homogeneous while the transverse shear deformation of the ring is considered negligible in accordance with the thin ring assumption and the Euler-Bernoulli theory (see Soedel, 2004). It is assumed that the circumferential

strain in mid-surface is zero and Galerkin's procedure is employed to obtain the equations of motion in terms of suitable generalized coordinates. Figure 2.1 shows the geometry and parameters used in the present research.

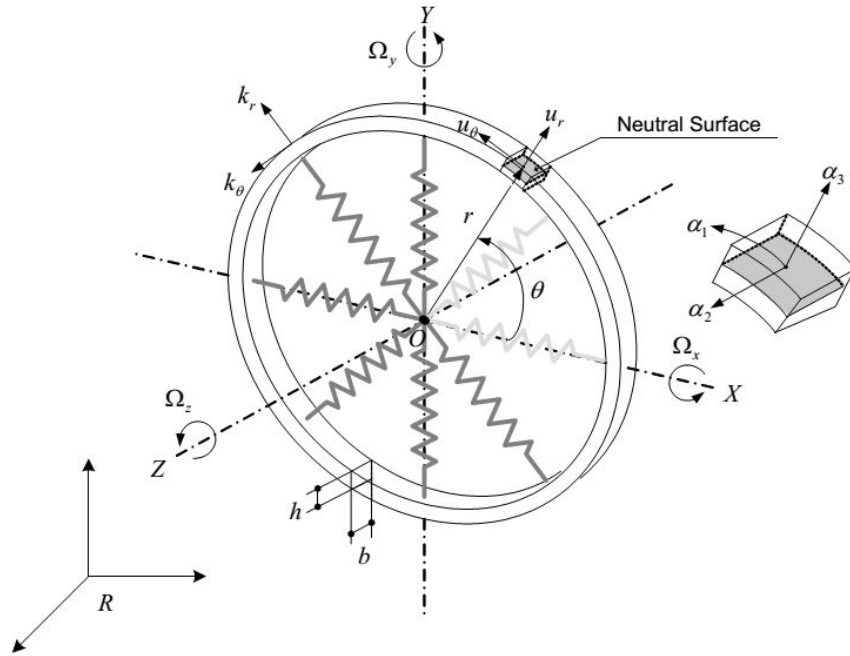


Figure 2.1: Schematic of the rotating ring geometry. (Cho, 2005)

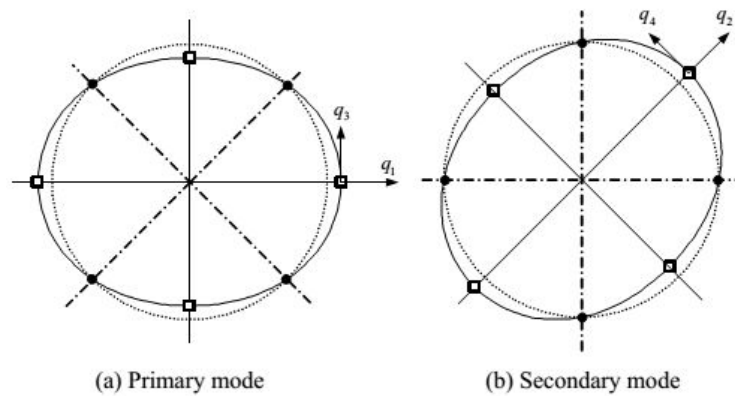


Figure 2.2: Visualization of the second flexural modes of the ring. (Cho, 2005)

Rotational coordinates  $\alpha_1$ ,  $\alpha_2$  and  $\alpha_3$  are used for locating the neutral surface elements and  $u_r$  and  $u_\theta$  represent the transverse and circumferential displacements, respectively. In order to incorporate the stiffness of the ring into the model, eight radial springs are considered with the stiffness components  $k_r$  and  $k_\theta$  representing the radial and circumferential components, respectively. Furthermore, the three components of the angular rate  $\Omega$  are shown in the figure. However, the current analysis is focused on effects of angular rotation in the Z-axis direction and the other components are assumed to be zero. Due to the symmetry of the geometry, the ring exhibits different mode shapes with identical natural frequencies as shown in Figure 2.2, referred to as degenerate mode shapes. Energy transfer between these degenerate configurations due to angular rotation can be used in order to measure angular rate.

## 2.3 Governing Equations

The general equations of motion to the ring can be derived using Hamilton's principle. To this end, the expressions for kinetic, potential, strain and external energy for the ring have been considered. Keeping the flexural vibration modes of the ring in mind, it can be shown that when vibration is excited in a particular mode in the ring and the ring is subjected to an external angular rate  $\Omega$ , the vibration mode shape tends to shift from one degenerate shape to the other, e.g., from the primary mode to the secondary mode or vice versa in Figure 2.2. This shift is due to the energy transfer between the extensional displacements of the two configurations as a result of Coriolis effect (Cho, 2005). This phenomenon can be employed in order to measure angular rate by detecting the shift between configurations. A number of mode shapes can be chosen for this purpose. However, excitation and measurement is more practical in some vibration modes. In the present research, the second mode, i.e.  $n = 2$ , is chosen due to the larger vibration amplitudes, simplicity in excitation and sensing methods and familiar shape of the vibration mode, commonly known as the "wineglass mode".



For this particular mode, four generalized coordinates can be defined as shown in Figure 2.2, where the generalized coordinates  $q_1(t)$  and  $q_2(t)$  represent the flexural displacements and  $q_3(t)$  and  $q_4(t)$  represent circumferential displacements. It can be seen that the two configurations of this mode are separated by  $45^\circ$  due to symmetry. In addition, the reversal of nodes and anti-nodes in the two degenerate configurations has also been depicted in the figure. Furthermore, the derived equations of motion can be rewritten in terms of only the flexural modes by applying the amplitude ratios described by Huang and Soedel (1987),

$$q_3 = -(1/n)q_1 \quad \text{and} \quad q_4 = (1/n)q_2, \quad (2.1)$$

The reduced discretized form of second order linear gyroscopic equations of motion for the ring using the flexural generalized coordinates  $\mathbf{q} = [q_1 \quad q_2]^T$  as:

$$\mathbf{M}\ddot{\mathbf{q}} + (\mathbf{G} + \mathbf{D})\dot{\mathbf{q}} + \mathbf{K}\mathbf{q} = \mathbf{F}, \quad (2.2)$$

The detailed derivation process can be found in Appendix A and also in Cho (2005). In Equation (2.2),  $\mathbf{G}$  represents the gyroscopic matrix which is a result of the Coriolis effect and provides coupling between the two flexural configurations,  $\mathbf{D}$  is the damping matrix,  $\mathbf{K}$  denotes the stiffness matrix and  $\mathbf{F}$  is the generalized excitation force vector. The system matrices take the form:

$$\mathbf{M} = \begin{bmatrix} 1 & 0 \\ 0 & 1 + \delta m \end{bmatrix} \quad (2.3)$$

$$\mathbf{G} = \begin{bmatrix} 0 & -2\Omega\gamma \\ 2\Omega\gamma & 0 \end{bmatrix}, \quad (2.4)$$

$$\mathbf{D} = \begin{bmatrix} 2\zeta\omega_{01} & 0 \\ 0 & 2\zeta\omega_{02} \end{bmatrix}, \quad (2.5)$$

$$\mathbf{K} = \begin{bmatrix} \kappa_1 + \kappa_2\Omega^2 & -\dot{\Omega}\gamma \\ \dot{\Omega}\gamma & \kappa_1 + \kappa_2\Omega^2 \end{bmatrix}, \quad (2.6)$$

$$\mathbf{F} = \begin{Bmatrix} f_1 \cos \omega t \\ 0 \end{Bmatrix}. \quad (2.7)$$

where,

$$\gamma = \frac{\hat{b} + n^2\hat{a}}{n(\hat{a} + \hat{b})}, \quad \kappa_1 = \frac{\hat{b}\hat{c} - n^2\hat{a}^2}{\rho A(\hat{a} + \hat{b})}, \quad \kappa_2 = \left( \frac{n^2(\hat{b} + \hat{c} - 4\hat{a})}{\hat{a} + \hat{b}} - \frac{(2+n)(\hat{b}\hat{c} - n^2\hat{a}^2)}{(\hat{a} + \hat{b})^2} \right),$$

$$\hat{a} = n^2 \frac{EI}{r^4} + \frac{EA}{r^2}, \quad \hat{b} = n^2 \left( \frac{EI}{r^4} + \frac{EA}{r^2} \right), \quad \hat{c} = n^4 \frac{EI}{r^4} + \frac{EA}{r^2}.$$

The intermediate parameters  $\tilde{a}$ ,  $\tilde{b}$  and  $\tilde{c}$  are defined in Appendix A as the set of Equations (A.23).

The system matrix  $\mathbf{M}$  is called the mass matrix. The effects of non-uniform distribution of mass along the circumference of the ring is incorporated in the mass matrix by employing the assumption that the mass of the ring is slightly higher, by the amount  $\delta m$  in the direction of the sensing coordinate. It may be noted that the stiffness matrix includes the centrifugal force term that depends on a factor  $\kappa_2$ , which takes a negative value for the present system. Hence, overall system stiffness is affected by angular velocity which may lead to lower system stability.

The damping matrix, apart from representing viscous dissipation, includes the gyroscopic cou-

pling term  $2\Omega\gamma$ , which is dependent on the input angular velocity. It is worth noting that owing to the gyroscopic as well as the centrifugal effects, the two undamped system natural frequencies  $\omega_{01}$  and  $\omega_{02}$  vary with the input angular velocity  $\Omega$ . However, at typical low input angular velocities of about  $2\pi$  rad/s, these two frequencies take nearly identical values (Asokanathan and Cho, 2006). The excitation frequency  $\omega$  is usually chosen close to the system natural frequencies  $\omega_{01}$  and  $\omega_{02}$  which is discussed in detail in Section 2.4.

Keeping in mind that during the present research, the ring is excited only in one flexural mode, the force vector can be simplified to the form shown in Equation (2.7), where,

$$f_1 = \frac{2f_r \hat{b}}{\rho A (\hat{a} \hat{b})}.$$

However, focusing on the system stability where the steady state response of the system is not of interest, the homogeneous form associated with Equation (2.2) in the absence of the excitation force  $f_1$  is considered for the numerical analysis chapter of the thesis.

Moreover, the term  $\dot{\Omega}$  can be neglected under the assumption of constant angular rate. On the other hand, this assumption is not practical in the presence of fluctuations in the angular rate. However, for the system under investigation, the contributions of the associated terms,  $\dot{\Omega}\gamma q_1$  and  $-\dot{\Omega}\gamma q_2$  are negligible when compared to  $2\Omega\gamma q_1$  and  $-2\Omega\gamma q_2$  at high angular rates where instability becomes an issue. Therefore, it is sufficient to approximate  $\dot{\Omega}\gamma q_1 = -\dot{\Omega}\gamma q_2 = 0$  for the purpose of stability analysis. Also, for the case of uniform mass distribution of the ring, mass mismatch  $\delta m = 0$ . However, mass mismatch is taken into account for natural frequency computations, hence incorporating the effect of non-uniform distribution of mass in the system equations. Applying the assumed conditions, the governing equations of motion of a ring-based gyroscope take the form of a second order ordinary differential equation,

$$\begin{bmatrix} 1 & 0 \\ 0 & 1 \end{bmatrix} \ddot{\mathbf{q}} + \begin{bmatrix} 2\zeta\omega_{01} & -2\Omega\gamma \\ 2\Omega\gamma & 2\zeta\omega_{02} \end{bmatrix} \dot{\mathbf{q}} + \begin{bmatrix} \kappa_1 + \kappa_2\Omega^2 & 0 \\ 0 & \kappa_1 + \kappa_2\Omega^2 \end{bmatrix} \mathbf{q} = \mathbf{0}. \quad (2.8)$$

It is known that for a typical ring-based gyroscope operation, one of the second flexural modes is harmonically excited while the measurement of angular shift of this mode towards the corresponding degenerate mode is employed in quantifying the angular rate. It may be noted that during the typical operation of a gyroscope an angular shift between  $0^\circ$  and  $45^\circ$  is realized as discussed in Section 2.2 and earlier in Section 2.3. Hence, the coordinate  $q_2$  can be thought of as being associated with the angular rate measurement while the coordinate  $q_1$  can be considered to represent the excitation. For the purposes of numerical simulations, the geometric and material properties of the ring as shown in Table 2.1 have been used. In particular, these properties are employed to calculate the ring parameters  $\gamma$ ,  $\kappa_1$  and  $\kappa_2$ .

Property	Value
Density	$\rho = 8800 \text{ kg/m}^3$
Young's modulus	$E = 210 \times 10^9 \text{ N/m}^2$
Mean radius	$r = 500 \mu\text{m}$
Radial thickness	$h = 12.5 \mu\text{m}$
Axial thickness	$b = 30 \mu\text{m}$

Table 2.1: Physical properties of the MEMS ring

## 2.4 Natural Frequency Variations

The natural frequencies of the two configurations of the second flexural mode depend on the mass mismatch factor as well as the angular rate of the ring. Using a micromachined ring-type sensor with isotropic material properties as described in Table 2.1, the variation of natural frequencies with angular rate can be obtained by Cho (2005) as depicted in Figure 2.3.

It can be seen that the natural frequencies of the two configurations remain the same in the absence of angular rate and mass anomalies. However, due to rotation of the ring about the Z-axis as shown in Figure 2.1, the natural frequencies deviate, with the natural frequency of

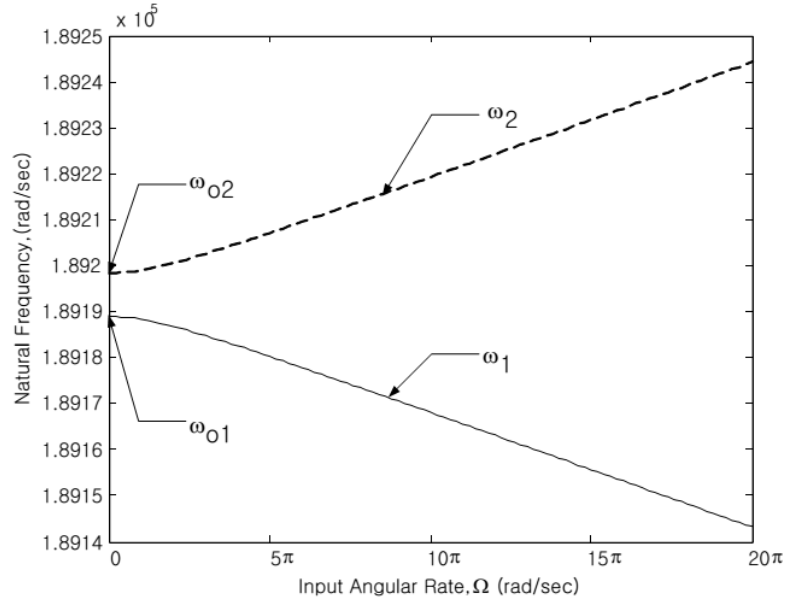


Figure 2.3: Variation of natural frequencies with angular rate with non-uniform mass assumption. (Cho, 2005)

the first flexural configuration decreasing while the second natural frequency is increased.

Introducing mass mismatch to the system by setting  $\delta m$  as low as 0.01% results in the bifurcation of the two natural frequencies in a stationary ring as shown in Figure 2.3. Similar to the ideal case, the first natural frequency is reduced with an increase in angular rate while the second natural frequency increases. Furthermore, increasing the mass mismatch consequently increases the bifurcation of natural frequencies.

## 2.5 Closure

The equations of motion for a thin vibrating ring previously derived by Cho (2005) are reviewed. Two coupled second order differential equations are obtained as a result. The equations are further simplified in order to prepare the equations for the proposed problem and performing numerical operations. Furthermore, the natural frequencies of the second flexural

vibration mode of the ring are visualized for different angular rates and mass mismatch values. It is revealed that bifurcation of natural frequencies occurs with increasing angular rate resulting in the first natural frequency to decrease while the second natural frequency is increased. What is more, the bifurcation gap is affected by the mass mismatch factor.

# Chapter 3

## Stochastic Model Incorporating Uncertainty in Input Angular Rate

### 3.1 Introduction

Many physical phenomena can be modeled as random processes. When such a phenomenon appears in a dynamical system, the physical model takes the form of a Stochastic Differential Equation (SDE). SDEs appear in the modeling of certain phenomena due to the fluctuations which appear in, for example, the physical properties of a system and hence the coefficients of ordinary differential equations are no longer deterministic. Fluctuations may occur in many forms, a number of which are categorized based on the frequencies of the fluctuations.

In the present research, Gaussian white noise is selected to be fit as a wide bandwidth of frequencies is covered by this type of function. Advantages of using white noise include the ability to study the effects of a wider bandwidth of frequencies and perform more realistic simulations.

## 3.2 Gaussian White Noise

White noise contains equal contributions from all visible frequency components. Whilst such processes seem to be physically impossible since the total energy of the signal would be infinity, a white noise model of excitation is used very often and is found to be convenient in representing random processes. The reason is that any causal system only responds to a limited range of excitation frequencies, therefore the components of the excitation which contain frequencies that are too high become irrelevant in predicting the system response. Ideal white noise is often used to simplify calculations and to obtain suitable orders of magnitude of the solution. Understanding the effect of white noise on the dynamic response of the system requires the basics of stochastic calculus which will be discussed in this chapter.

### 3.2.1 Stochastic Calculus

A stochastic process can be defined as any discrete or continuous process that is a collection of random variables associated with a deterministic parameter (Jekeli, 2001). A stochastic process  $X$  can be mathematically defined as

$$(X_t, t \in T) = (X_t(\phi), t \in T, \phi \in \Phi),$$

defined on a space  $\Phi$ , where  $T$  is an arbitrary time interval. Keeping the definition in mind, a stochastic process  $W = (W(t), t \in [0, \infty])$  is called a (standard) Brownian motion or Wiener process if the following conditions are satisfied (Mikosch, 1999; Kloeden and Platen, 1992):

- The process is continuous and starts at zero, i.e.,  $W(0) = 0$ .
- Expected value of the process is zero at any given time, i.e.,  $E[W(t)] = 0$ , and
- The process has independent and stationary increments, i.e.,  $W(t) - W(s)$  has a normal



distribution  $N(0, t - s)$ .

White noise is defined as a wide-range stationary process  $\xi(t)$  with mean zero and constant spectral density function  $S(\omega) = S_0$ , where  $\omega$  represents any arbitrary frequency in the domain  $[-\infty, +\infty]$ . The important properties of white noise can be summarized as:

- $E[\xi(t)] = 0$ , and
- $E[W(t)W(t + \tau)] = S_0\delta(t)$ .

The name, "white", comes from the fact that the average power is distributed uniformly in frequency, similar to white light. Furthermore, considering a function  $W(t)$ , generating a Brownian motion with variance  $S_0$ , it can be show that the first time derivative of  $W(t)$  is in fact Gaussian white noise (Kloeden and Platen, 1992):

$$\xi(t) = \frac{dW}{dt}. \quad (3.1)$$

This result is later on used in introducing noise to the geometrical system by generating a sequence of random number based on a Brownian motion and using the numerical first derivative to simulate white noise.

### 3.3 Stochastic Fluctuation in Angular Rate

It is known that numerical schemes developed for SDE are limited to first order differential equations. Therefore, prior to applying the numerical methods, Equation (2.8) is converted to four first order differential equations. Uncertainty parameters for angular velocity are also introduced in the equations during this process. The resulting equations of motion can then be written in a standard form of an SDE for the purposes of numerical computations. In order to convert Equation (2.8) from two second order equations into four first order equations, the

reduction of order technique is employed. For this purpose four state variables are defined as:

$$q_1 = x_1, \dot{q}_1 = x_2, q_2 = x_3, \text{ and } \dot{q}_2 = x_4.$$

Substituting the defined variables  $x_1$  to  $x_4$  into Equation (2.8) yields:

$$\dot{x}_2 + 2\zeta\omega_{01}x_2 - 2\Omega\gamma x_4 + (\kappa_1 + \kappa_2\Omega^2)x_1 = 0 \quad (3.2)$$

$$(1 + \delta m)\dot{x}_4 + 2\Omega\gamma x_2 + 2\zeta\omega_{02}x_4 + (\kappa_1 + \kappa_2\Omega^2)x_3 = 0 \quad (3.3)$$

In order to represent the random fluctuation in the input angular velocity, these fluctuations are assumed to take the form of a white noise process. Understanding that the first time derivative of a Brownian motion process is Gaussian white noise, a Brownian motion function  $W(t)$  is employed to simulate the white noise (see e.g., Kloeden and Platen, 1992). Introducing the random fluctuation to a nominal input angular velocity  $\Omega_0$ , the input angular velocity is written as:

$$\Omega = \Omega_0 + \mu_0\xi(t), \quad (3.4)$$

where  $\xi(t)$  is white noise and  $\mu_0$  is the noise intensity magnitude. Using Equation (3.4), the centrifugal component of the equations of motion can be evaluated as:

$$\Omega^2 = \Omega_0^2 + 2\mu_0\Omega_0\xi(t) + \mu_0^2\xi^2(t). \quad (3.5)$$

The last term on the right hand side of Equation (3.5) is considered negligible due to its lower order of smallness, since  $\mu_0\xi(t)$  which represents fluctuations in angular rate is small relative to the nominal angular rate  $\Omega_0$  and consequently  $\mu_0^2\xi^2(t) \ll 1$ . In order to better characterize the fluctuation magnitude, a parameter  $\mu$  that represents the noise intensity ratio is introduced as:

$$\mu = \frac{\mu_0 \max(\xi(t))}{\max(\Omega_0)}. \quad (3.6)$$

Substituting Equations (3.4) and (3.5) in Equations (3.2) and (3.3) and multiplying the equations by  $dt$  yields

$$dx_2 = \left[ 2(\Omega_0 + \mu_0 \frac{dW}{dt})\gamma x_4 - 2\zeta\omega_{01}x_2 - (\kappa_1 + \kappa_2(\Omega_0^2 + 2\mu_0\Omega_0 \frac{dW}{dt}))x_1 \right] dt, \quad (3.7)$$

$$dx_4 = \frac{1}{1 + \delta m} \left[ -2(\Omega_0 + \mu_0 \frac{dW}{dt})\gamma x_2 - 2\zeta\omega_{02}x_4 - (\kappa_1 + \kappa_2(\Omega_0^2 + 2\mu_0\Omega_0 \frac{dW}{dt}))x_3 \right] dt. \quad (3.8)$$

The equations for the four state variables can be obtained by simplifying the equations and neglecting the higher order terms:

$$dx_1 = x_2 dt, \quad (3.9)$$

$$dx_2 = (2\Omega_0\gamma x_4 - 2\zeta\omega_{01}x_2 - (\kappa_1 - \kappa_2\Omega_0^2)x_1) dt + (2\mu_0\gamma x_4 - 2\kappa_2\mu_0\Omega_0 x_1) dW, \quad (3.10)$$

$$dx_3 = x_4 dt, \quad (3.11)$$

$$dx_4 = \frac{-2\Omega_0\gamma x_2 - 2\zeta\omega_{02}x_2 - (\kappa_1 - \kappa_2\Omega_0^2)x_3}{1 + \delta m} dt - \frac{2\mu_0\gamma x_2 - 2\kappa_2\mu_0\Omega_0 x_3}{1 + \delta m} dW. \quad (3.12)$$

Rewriting the equations in matrix form, a system of SDEs that represents the motion is obtained as:

$$\begin{aligned} \begin{pmatrix} dx_1 \\ dx_2 \\ dx_3 \\ dx_4 \end{pmatrix} &= \begin{bmatrix} 0 & 1 & 0 & 0 \\ -\kappa_1 - \kappa_2\Omega_0^2 & -2\zeta\omega_{01} & 0 & 2\Omega_0\gamma \\ 0 & 0 & 0 & 1 \\ 0 & \frac{-2\Omega_0\gamma}{1 + \delta m} & \frac{-\kappa_1 - \kappa_2\Omega_0^2}{1 + \delta m} & \frac{2\zeta\omega_{02}}{1 + \delta m} \end{bmatrix} \begin{pmatrix} x_1 \\ x_2 \\ x_3 \\ x_4 \end{pmatrix} dt \\ &+ \begin{bmatrix} 0 & 0 & 0 & 0 \\ -2\kappa_2\mu_0\Omega_0 & 0 & 0 & 2\mu_0\gamma \\ 0 & 0 & 0 & 0 \\ 0 & \frac{-2\mu_0\gamma}{1 + \delta m} & \frac{-2\kappa_2\mu_0\Omega_0}{1 + \delta m} & 0 \end{bmatrix} \begin{pmatrix} x_1 \\ x_2 \\ x_3 \\ x_4 \end{pmatrix} dW, \end{aligned} \quad (3.13)$$

where the resultant  $4 \times 1$  coefficient matrix associated with the term  $dt$  is called the drift matrix,  $\mathbf{a}[\mathbf{X}(t)]$  and the resultant  $4 \times 1$  coefficient matrix associated with the term  $dW$  is called

the diffusion matrix,  $\mathbf{b}[\mathbf{X}(t)]$ , with the state vector  $\mathbf{X}(t) = [x_1 \ x_2 \ x_3 \ x_4]^T$  (see e.g., Higham, 2001; Kloeden and Platen, 1992; Higham and Kloeden, 2002). In the present numerical study, a smooth increase of the input angular rate  $\Omega_0$  from zero to  $2\pi$  rad/s is employed for the purposes of response predictions.

### 3.4 Itô-Taylor Expansion

It is known that an exact analytical solution does not exist for the stochastic differential equations that represent the motion of a gyroscope. A numerical simulation of the system seems to be the most efficient method. For this purpose, a number of iterative approaches to integrate SDEs numerically have been developed in the recent past. The most widely-used ones are Euler-Maruyama, Euler-Heun, Milstein, derivative-free Milstein (Runge-Kutta approach), and Stochastic Runge-Kutta (see Schaffter, 2010). The higher-order Milstein scheme which takes advantage of the Itô-Taylor expansion for discretization of the SDE (Higham and Kloeden, 2002) is the most suitable for the present governing equations.

In an effort to describe this method, the Itô-Taylor expansion of the SDE for a scalar dependent variable  $X$ ,

$$dX(t) = a[X(t)]dt + b[X(t)]dW(t) \quad (3.14)$$

is presented, where  $a[X(t)]$  and  $b[X(t)]$ , respectively, denote the drift and the diffusion terms while  $dW(t)$  represents the driving Wiener Process. Use of the Itô's Lemma (Higham and Kloeden, 2002) leads to

$$df[X(t)] = L^0 a[X(t)]dt + L^1 b[X(t)]dW(t), \quad (3.15)$$

where

$$L^0 \equiv \frac{\partial}{\partial t} + a \frac{\partial}{\partial X} + \frac{1}{2} b^2 \frac{\partial^2}{\partial X^2},$$

$$L^1 \equiv b \frac{\partial}{\partial X},$$

and  $f(X[t])$  is any function of  $X[t]$  with all functions evaluated at  $(t, x)$ . The Itô formula can then be written in the form of the Itô stochastic integral equation:

$$f[X(t)] = f[X(t_0)] + \int_{t_0}^t L^0 f[X(s)] ds + \int_{t_0}^t L^1 f[X(s)] dW_s. \quad (3.16)$$

Setting  $f(X) = X$  and assuming that  $a$  and  $b$  do not depend on  $t$  explicitly, the equation becomes

$$X(t) = X(t_0) + \int_{t_0}^t a[X(s)] ds + \int_{t_0}^t b[X(s)] dW_s. \quad (3.17)$$

Itô's Lemma may be iterated to obtain constant integrands for the higher order terms. Choosing  $f(X) = a[X(t)]$  and  $f(X) = b[X(t)]$  and applying Equation (3.16), the higher order coefficients are derived as

$$a[X(t)] = a[X(t_0)] + \int_{t_0}^t L^0 a[X(s)] ds + \int_{t_0}^t L^1 a[X(s)] dW_s, \quad (3.18)$$

and

$$b[X(t)] = b[X(t_0)] + \int_{t_0}^t L^0 b[X(s)] ds + \int_{t_0}^t L^1 b[X(s)] dW_s. \quad (3.19)$$

Substituting into Equation (3.17), yields

$$\begin{aligned} X(t) = X(t_0) &+ \int_{t_0}^t \left\{ a[X(t_0)] + \int_{t_0}^{s_1} L^0 a[X(s_2)] ds_2 + \int_{t_0}^{s_1} L^1 a[X(s_2)] dW(s_2) \right\} ds_1 \\ &+ \int_{t_0}^t \left\{ b[X(t_0)] + \int_{t_0}^{s_1} L^0 b[X(s_2)] ds_2 + \int_{t_0}^{s_1} L^1 b[X(s_2)] dW(s_2) \right\} dW(s_1). \end{aligned} \quad (3.20)$$

Evaluation of the integrals follows:

$$\begin{aligned}
X(t) = & X(t_0) + a[X(t_0)] \int_{t_0}^t ds_1 + b[X(t_0)] \int_{t_0}^t ds_2 \\
& + \int_{t_0}^t \int_{t_0}^{s_1} L^0 a[X(t)] ds_2 ds_1 + \int_{t_0}^t \int_{t_0}^{s_1} L^1 a[X(s_2)] dW(s_2) ds_1 \\
& + \int_{t_0}^t \int_{t_0}^{s_1} L^0 b[X(s_2)] ds_2 dW(s_1) + \int_{t_0}^t \int_{t_0}^{s_1} L^1 b[X(s_2)] dW(s_2) dW(s_1).
\end{aligned} \tag{3.21}$$

Substituting the functions  $L^0$  and  $L^1$  as defined and carrying the integrals, the equation can be rewritten as

$$\begin{aligned}
X(t) = & X(t_0) + a[X(t)] \int_{t_0}^t ds_1 + b[X(t)] \int_{t_0}^t dW(s_1) \\
& + b[X(t_0)]b'[X(t_0)] \int_{t_0}^t \int_{t_0}^{s_1} dW(s_2) dW(s_1) + O(\delta t^{3/2}),
\end{aligned} \tag{3.22}$$

where  $O(\delta t^{3/2})$  represents terms that include  $\delta t^{3/2}$  or terms of higher order and  $b'$  denotes derivative of function  $b$  with respect to variable  $X$ . The order of the terms are assessed with the the properties of Wiener process in mind, where  $E[dW^2(t)] = dt$  and hence each  $dW^2$  term is weighed similar in order as a first order  $dt$  term.

It should be noted that the double integral in Equation (3.22) is an Itô integral and therefore cannot be evaluated by classical calculus methods such as the conventional Reimann method. The double integral in Equation (3.22) can be evaluated using Itô integral rules as (Kloeden and Platen, 1992):

$$\int_{t_0}^t \int_{t_0}^{s_1} dW(s_2) dW(s_1) = \frac{1}{2}[W(t) - W(t_0)]^2 - \frac{1}{2}(t - t_0). \tag{3.23}$$

Substitution of the double integral in Equation (3.22) yields

$$\begin{aligned}
X(t) = & X(t_0) + a[X(t)] \int_{t_0}^t ds_1 + b[X(t)] \int_{t_0}^t dW(s_1) \\
& + b[X(t_0)]b'[X(t_0)]\left\{\frac{1}{2}[W(t) - W(t_0)]^2 - \frac{1}{2}(t - t_0)\right\} + O(\delta t^{3/2}).
\end{aligned} \tag{3.24}$$

This equation forms the theoretical basis for both Euler and Milstein schemes (Higham and Kloeden, 2002). It may be noted that the Euler scheme is constructed using the first three terms of this expansion while incorporation of the fourth term yields the Milstein scheme. Considering the time interval  $[t_i, t_{i+1}]$ , by choosing

$$t_0 = t_i, t = t_{i+1}, \Delta t = t_{i+1} - t_i, \text{ and } \Delta W_i = W(t_{i+1}) - W(t_i),$$

the discretized form for the use of Milstein method is formulated as:

$$X(t_{i+1}) = X(t_i) + a[X(t_i)]\Delta t + b[X(t_i)]\Delta W_i + \frac{1}{2}b[X(t_i)]b'[X(t_i)]\{(\Delta W_i)^2 - \Delta t\}, \quad (3.25)$$

where  $\Delta W$  is a Wiener process with the properties  $E[W(t)] = 0$  and  $E[W^2(t)] = \Delta t$ . For the purposes of numerical approximation,  $\Delta W$  can be generated using a uniformly distributed sequence of random numbers as (Kloeden and Platen, 1992):

$$\Delta W(t_i) = N(0, 1)\Delta t_i \quad (3.26)$$

Equation (3.25) when extended to multi-dimensional systems yields the component of the state vector employing Milstein scheme for numerical computations and takes the general form

$$\mathbf{X}^u(t)_{i+1} = \mathbf{X}^u(t)_i + \mathbf{a}^u[\mathbf{X}^u(t)_i]\Delta t + \sum_{j=1}^m \mathbf{b}^{u,j}[\mathbf{X}^u(t)_i]\Delta \mathbf{W}_i^j + \sum_{j_1, j_2=1}^m L^{j_1} \mathbf{b}^{u, j_2}[\mathbf{X}^u(t)_i] I_{j_1, j_2}, \quad (3.27)$$

where the drift and diffusion terms, the driving Wiener process and the variables are written in vector form. In Equation (3.27),

$$L^{j_1} = \sum_{k=1}^d \mathbf{b}^{k, j_1}[\mathbf{X}^u(t)_i] \frac{\partial}{\partial \mathbf{X}^k}, \quad I_{j_1, j_2} = \int_{t_i}^{t_{i+1}} \int_{t_i}^{s_1} d\mathbf{W}_{s_2}^{j_1} d\mathbf{W}_{s_1}^{j_2},$$

$\mathbf{b}[X(t_i)]$  is the diffusion coefficient matrix,  $d$  is the number of dimensions and  $m$  represents the number of independent Wiener processes (Higham and Kloeden, 2002).

The vector-based scheme presented in Equation (3.27), considering the system drift and diffusion coefficient matrices, is employed for the purposes of performing numerical computations to solve the system of equations that govern the gyroscope response. To this end, considering Equation (3.13) and setting  $d$  to 4 and  $m$  to 1 in Equation (3.27), the response takes the form:

$$\begin{aligned} \mathbf{X}^u(t_{i+1}) = & \mathbf{X}^u(t_i) + \mathbf{a}^u[\mathbf{X}^u(t_i)]\Delta t + \mathbf{b}^{u,1}[\mathbf{X}^u(t_i)]\Delta W_i \\ & + \sum_{k=1}^4 \frac{1}{2} \mathbf{b}^{k,1}[\mathbf{X}^u(t_i)] \frac{\partial \mathbf{b}^{u,1}[\mathbf{X}(t_i)]}{\partial \mathbf{X}^k} \left\{ (\Delta W_i)^2 - \Delta t \right\}, \quad u = 1, 2, \dots, 4. \end{aligned} \quad (3.28)$$

The resulting four equations are employed in the prediction of gyroscope response.

Conforming to the goal of the present study, namely the stability investigation, free vibration of the gyroscope when subjected to an initial disturbance is examined.

### 3.5 Lyapunov Characteristic Exponent

The Lyapunov characteristic exponent for determining stability of dynamic systems was first introduced by Wolf et al. (1985). Lyapunov exponents are defined as the average rate of divergence or convergence of nearby orbits in the  $n$ -dimensional phase space (Baker and Gollub, 1990). Any system with at least one positive Lyapunov exponent will inevitably become unpredictable, with the magnitude of the exponent reflecting on the time scale that system dynamics will diverge. Therefore, it is sufficient to only calculate the largest of the characteristic exponents in order to determine system stability. In order to calculate Lyapunov exponents, the long-term evolution of an infinitesimal  $n$ -sphere of initial conditions is observed as the spheres turn into  $n$ -ellipsoids. The  $i$ th one-dimensional Lyapunov exponent is then defined in terms of the ratio between the principal axes of the ellipsoid:

$$\lambda_i = \lim_{t \rightarrow \infty} \frac{1}{t} \frac{p_i(t)}{p_0(t)}. \quad (3.29)$$



The method was further developed by Rosenstein et al. (1993) applied to small data sets with less computational effort. For the present work, the algorithm used was based on the method developed by Rosenstein et al. This method, as previously mentioned, requires reconstruction of the time response in phase space. For this purpose, the method of time delay as explained by Kliková and Raidl (2011), which is one of the most frequently used methods of phase space construction, was used. Using this algorithm, a parameter sweep was performed on noise intensity for different values of damping ratios. The details of the computer code used for this purpose can be found in Appendix B.

### **3.6 Closure**

The necessary stochastic tools are reviewed and fluctuations in input angular rate are introduced in the form of a Gaussian white noise function. An order reduction operation is performed on the second order equations of motion in order to obtain four first order differential equations. Fluctuations in angular rate are implemented in the resulting equations and the equations are rearranged as a Stochastic Differential Equation (SDE). The Euler numerical scheme as well as the higher-order Milstein numerical scheme are introduced and explained and the higher-order Milstein scheme is applied to the SDE in order to achieve higher accuracy. Furthermore, the Lyapunov characteristic exponent and the Largest Lyapunov Exponent stability criterion are introduced for the purposes of verification of the final Matlab script.

# Chapter 4

## Stability Analysis Using Numerical Methods

### 4.1 Introduction

For the purposes of studying the stability of the gyroscope, time response for the free vibration of the system is examined, when the system is subjected to suitable initial conditions. Simulations performed are based on an assumption that an initial displacement of  $10^{-5}$  m being exerted on the driving coordinate,  $q_1$ , while stochastic fluctuations in input angular rate are applied as described in Equation (3.4). The sensing coordinate  $q_2$  is then quantified for the purposes of characterizing the gyroscope response.

Initially, the predicted responses using the higher-order Milstein scheme are compared with the results obtained using the simpler Euler scheme in order to assess the validity of the developed Milstein algorithm and also investigate the benefits of using a higher-order scheme. Moreover, the Largest Lyapunov Exponents of the predicted responses are evaluated in order to study the stability of the system. Finally, the higher-order Milstein scheme is used in order to find the stability threshold of the system under stochastic fluctuation and considering different damping

ratio values. The developed Matlab code is discussed in detail in Appendix B. The hardware used for numerical calculations consisted of a Windows 7 PC with an AMD Phenom™ Quad Core processor clocked at 2.2 GHz and 8GB of memory.

## 4.2 Numerical Predictions

In order to ascertain the accuracy of the developed model, the convergence of the simulation algorithm is tested with four different damping ratio values, namely 0.03, 0.05, 0.09 and 0.13. Numerical convergence is reached in 150000 or more time steps for a duration of 0.009 seconds of simulation time and the number of time steps is considered adequate for the remainder of the study.

The vector-based higher-order Milstein scheme has been chosen for this study instead of the

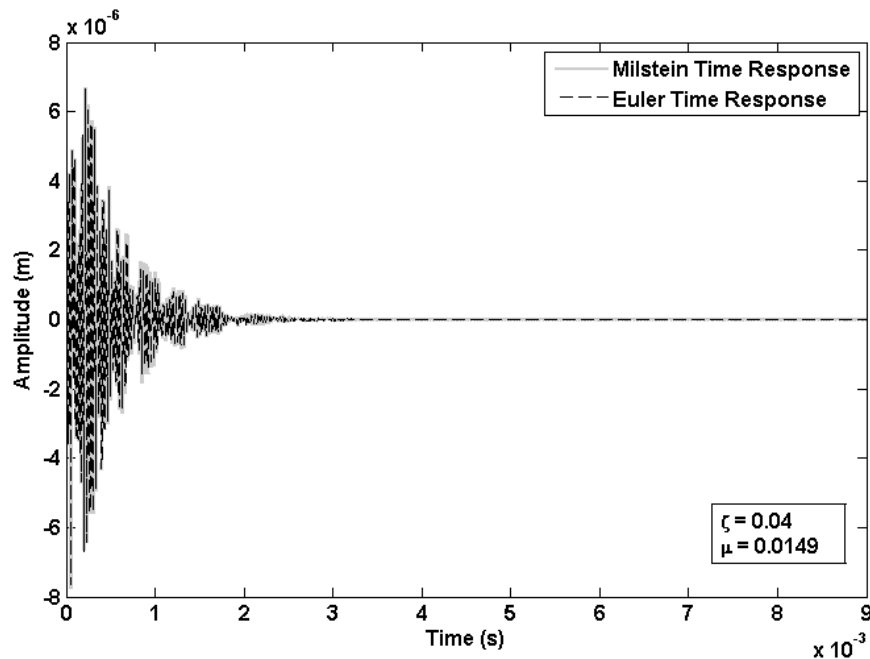


Figure 4.1: Example of stable time response.

simpler Euler approach in order to investigate whether higher accuracy will be achieved for

the numerical simulations by employing a higher-order scheme. System time responses generated by the two methods were compared for the purposes of verifying the response predictions. Figures 4.1 to 4.3 show the responses of the gyroscope under different fluctuation magnitudes and displaying both stable and unstable behavior of the system. The Wiener process is numerically simulated using the random number generation function in MATLAB and employing the method discussed in Equation (3.26). The details of the developed MATLAB code used for generation of the Wiener process are available in Appendix B.2. Maximum relative noise intensity, as defined in Equation (3.6) has been used as a magnitude measure for representing environment fluctuation. Figure 4.1 shows the response of the system for a damping ratio of 0.04 and maximum relative noise intensity measure  $\mu = 0.0149$ .

It can be seen that with sufficient damping, the system is observed to remain stable. However, as shown in Figure 4.2, as noise intensity is increased to a sufficiently high value to cause noticeable disturbance in the system, yet low enough to be damped, the system shows oscillatory motion until complete decay. It may be noted that a certain threshold intensity measure for each damping ratio is associated with transition to instability and this measure can be computed using the time responses.

For damping ratios less than the threshold value or, alternatively with sufficiently high noise measure, the system response becomes unstable, as shown in Figure 4.3. Furthermore, it may be noted that Euler and Milstein schemes both predict similar time responses, with Milstein scheme which accounts for additional higher-order terms showing slightly larger values for the response compared with those predicted via the Euler scheme. Further, the Euler scheme which does not take the higher order terms into account results in an under-predicted response, hence exhibiting increased system stability. As a result, under certain conditions where noise intensity is close to the threshold values, it appears that Euler scheme can predict a stable system behavior while Milstein scheme predicts an unstable behavior. An example of such conditions is shown in Figure 4.4. There are also cases where Euler scheme might predict a marginally stable behavior while Milstein scheme, accounting for higher order terms predicts a clearly

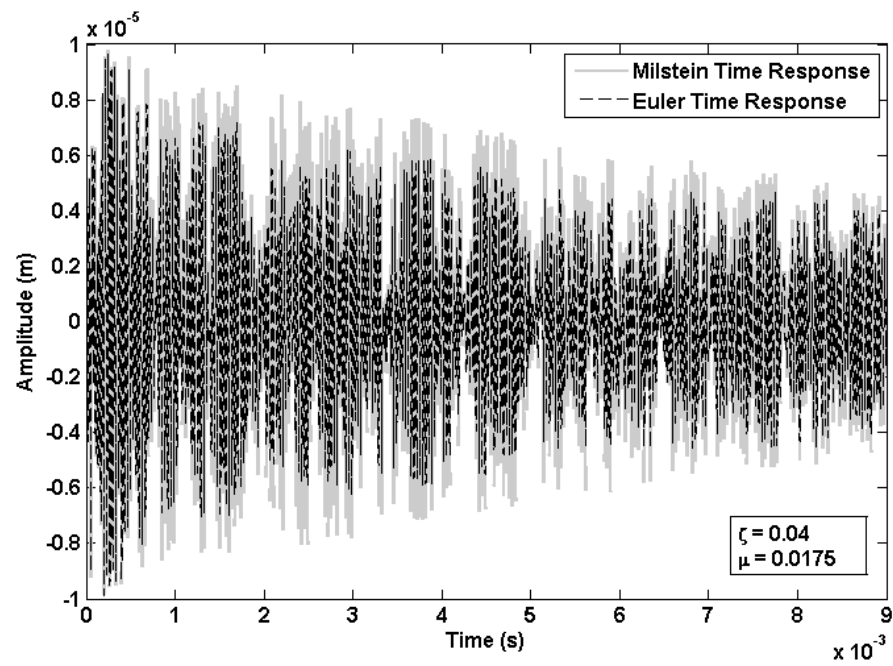


Figure 4.2: Example of marginally stable time response.

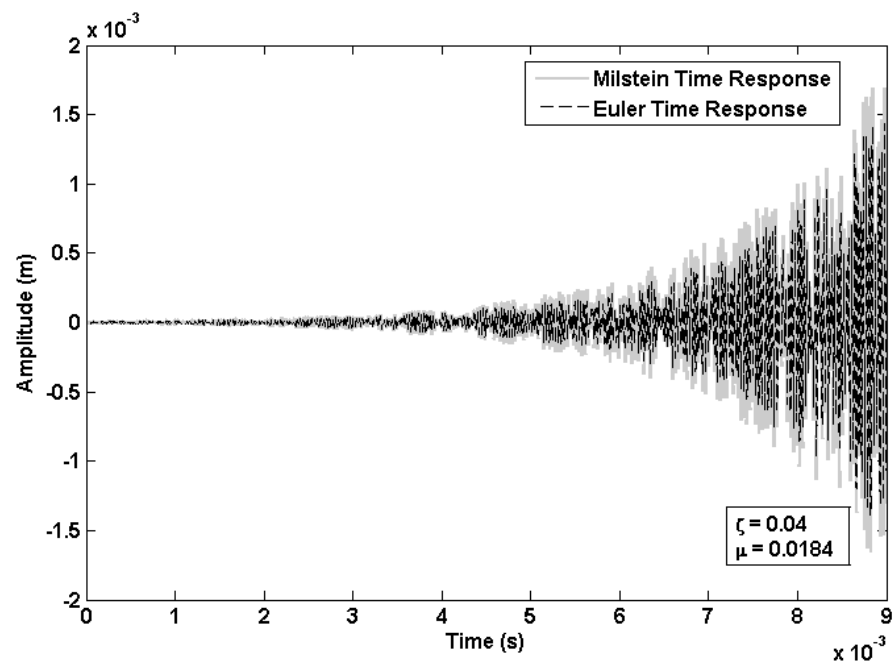


Figure 4.3: Example of unstable time response.

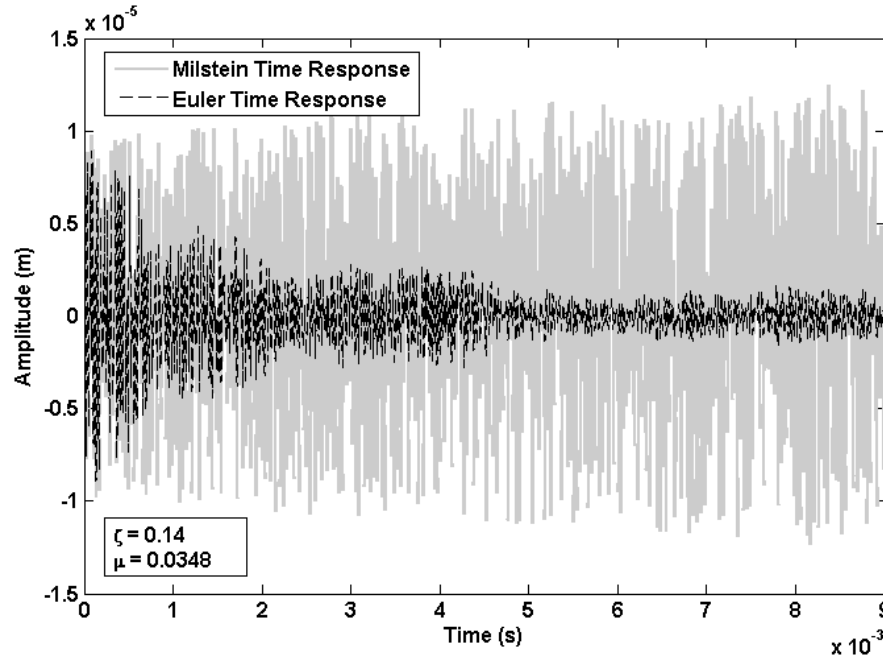


Figure 4.4: Under-prediction of results by Euler scheme in a marginally stable case.

unstable behavior as shown in Figure 4.5. Therefore, due to lack of any exact analytical or experimental results to verify the acquired data against, it is necessary that the accuracy of the employed model is assessed before proceeding to the parameter sweep for characterizing the system behavior under changes in pertinent system parameters. For this purpose, dynamic stability of the system is studied employing the two schemes using the Largest Lyapunov Exponent (LLE) method as a stability measure. Lyapunov exponents are defined as the average rate of divergence or convergence of nearby orbits in the  $n$ -dimensional phase space (see, e.g., Kliková and Raidl, 2011). Any system with at least one positive Lyapunov exponent will inevitably become unstable, with the magnitude of the exponent reflecting on the time scale that system dynamics will diverge. Therefore, it is sufficient to calculate the largest Lyapunov exponent for characterizing system stability. In the present study, a practical implementation of the LLE search algorithm, based on the method of time delay as presented in Kliková and Raidl (2011), is employed. Figure 4.6 shows the values of threshold noise intensity factors obtained at which the system starts to exhibit instability.

For the purposes of confirming that the results from Milstein and Euler schemes are compatible, and also for studying the error introduced by neglecting higher-order terms in Euler scheme, a number of points have been chosen for the LLE study. Three highly stable points that correspond to damping ratios of 0.03, 0.08 and 0.13 and the respective maximum relative noise intensity values of 0.0114, 0.0225 and 0.0294 as displayed in Figure 4.6 have been chosen. LLE values evaluated at these points resulted in the same sign, in this case being negative confirming that the system is stable under such conditions. However, LLE values predicted by Eulers scheme have been found to be lower than those predicted by Milstein Scheme by 3.8 to 8.5 percent. Further, comparison of the time responses predicted by these two schemes reveals that the Euler scheme tend to under-predict the response for the present gyroscopic system. Hence, it may be concluded that contribution from the higher-order terms could be significant and the use of Milstein scheme is beneficial in some cases. However, for the purposes of predicting the response of this class of gyroscopes Euler scheme offers lower computation time

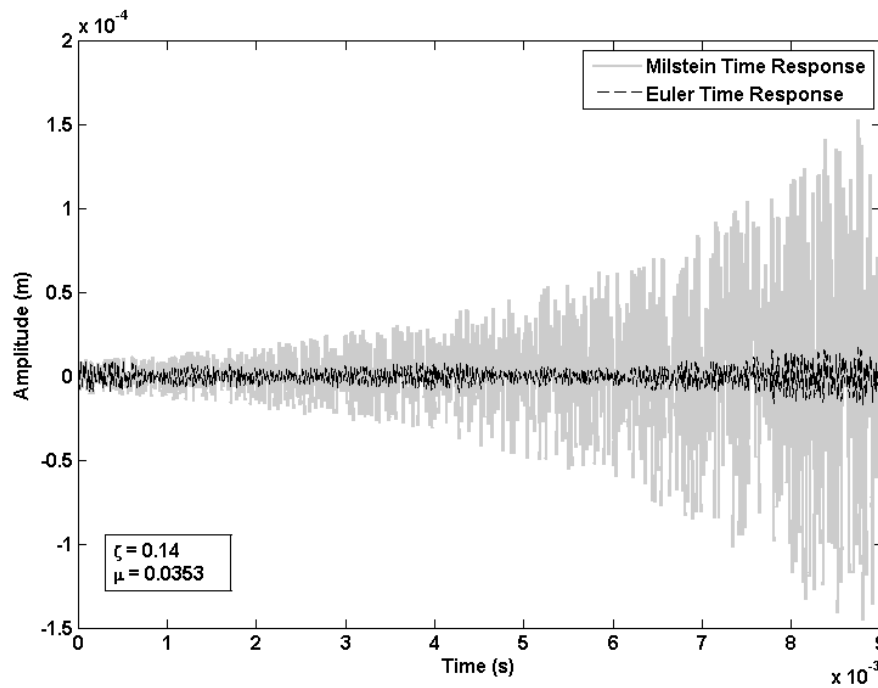


Figure 4.5: Under-prediction of results by Euler scheme in a marginally unstable case.

and resource requirements. The details of the LLE calculations are summarized in Table 4.1. It should be noted that the difference percentage is calculated by considering the difference between the LLE values obtained using Milstein and Euler schemes divided by the LLE value obtained using Euler scheme.

Damping Ratio $\zeta$	Raw noise intensity $\mu_0$	Milstein	Euler	Relative Difference
0.03	65	-1.31E+08	-1.35E+08	-3.8%
	83	-1.72E+07	-2.28E+07	-24.3%
	87	2.33E+07	2.20E+07	5.87%
0.08	129	-2.57E+08	-2.77E+08	-7.07%
	147	-1.22E+07	-3.39E+07	-64%
	152	6.36E+07	5.67E+07	12.1%
0.13	168	-4.05E+08	-4.43E+08	-8.5%
	188	-5.93E+07	-9.80E+07	-39.5%
	194	3.73E+07	4.11E+07	-9.04%

Table 4.1: Summary of LLE values for predicted time responses.

In order to further confirm that the two schemes predict approximately compatible instability thresholds for the system, six marginal points as shown in Figure 4.6 have been chosen for analysis. Three points slightly above the threshold point within the unstable region and three points slightly below within the stable region have been chosen. The LLE analysis reveals that both schemes predict the LLE value with the same sign and therefore predicting stability and instability regions correctly.

### 4.3 Parametric Study

It is known that external noise is one of the most important parameters that affect the gyroscope dynamic behavior. Such noise usually results from environment factors and the nature of the system operation and can be exerted on the system at any frequency range depending on



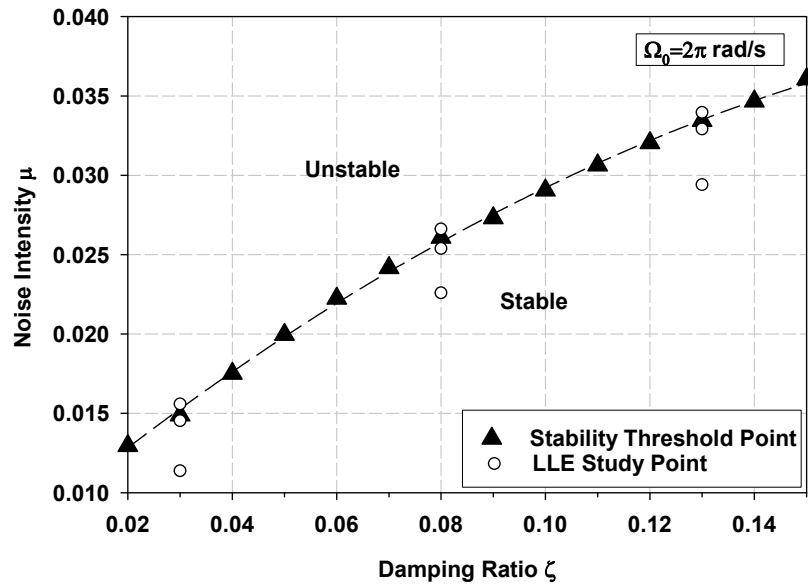


Figure 4.6: Stability boundary in the  $\mu$ - $\zeta$  space ( $\Omega = 2\pi$  rad/s).

the source. Furthermore, MEMS systems are generally designed to demonstrate low damping ratios (high quality factor) and incorporating the allowable fluctuation in the system design becomes important. Therefore, a parametric study is performed to assess the noise intensity stability threshold for a number of damping ratio values. For this purpose, the damping ratio of the system is changed with 0.01 increments and the noise stability threshold of the system is obtained by employing the bisection search method and analyzing the predicted time response. Figure 4.6 shows that noise intensity threshold is increased at higher damping ratios. In addition, studies performed on varying input angular rates of practical significance for typical gyroscope applications revealed that changes in angular velocity does not affect noise threshold significantly. Variation of system natural frequencies with typical input angular rates can be seen in Table 4.2. However, under unrealistic high angular velocities, namely values close to system natural frequencies, where the first natural frequency tends to decrease while the second natural frequency  $\mu$  increases, noise thresholds seem to increase. This behavior may be attributed to the centrifugal force component present in the stiffness matrix which increases with angular

velocity, affecting overall system stiffness. Further, it has been found that moderate changes in mass mismatch do not affect the noise threshold. However, unrealistic mass mismatch values close to 10 percent cause a reduction in the second natural frequency and as a consequence appear to contribute to a reduction in the noise threshold. It is worth noting that such values for mass mismatch and angular velocity are not of practical significance under typical gyroscope operating conditions. Variation of system natural frequencies with mass mismatch can be seen in Table 4.3. It should also be noted that increasing the mismatch only results in the reduction of the first natural frequency while the second natural frequency of the system is unaffected by the mismatch at a constant angular rate.

$\Omega_0$ (rad/s)	$\omega_{01}$ (rad/s)	$\omega_{02}$ (rad/s)	Change Relative to Stationary Ring
0	$1.9864 \times 10^5$	$1.9865 \times 10^5$	-
$2\pi$	$1.9864 \times 10^5$	$1.9865 \times 10^5$	0 %
$10\pi$	$1.9862 \times 10^5$	$1.9867 \times 10^5$	0.01%

Table 4.2: Variation of system natural frequencies with input angular rate.

$\delta m$	$\omega_{01}$ (rad/s)	$\omega_{02}$ (rad/s)	Change Relative to Stationary Ring
0	$1.9864 \times 10^5$	$1.9865 \times 10^5$	-
$10^{-4}$	$1.9864 \times 10^5$	$1.9865 \times 10^5$	0 %
$10^{-3}$	$1.9855 \times 10^5$	$1.9865 \times 10^5$	0.04%
$10^{-2}$	$1.9766 \times 10^5$	$1.9865 \times 10^5$	0.49%
$10^{-1}$	$1.8940 \times 10^5$	$1.9865 \times 10^5$	4.65%

Table 4.3: Variation of system natural frequencies with mass mismatch.

## 4.4 Closure

Time response predictions via Euler scheme as well as the Largest Lyapunov Exponents have been used for comparison of accuracy of the predictions and validation of the developed higher-

order solution. The results are found to be compatible and it is shown that while a significant difference between the two schemes is not visible using the considered system, the effect of the higher-order terms can become significant in some cases. A parametric study is performed using the higher-order method and the threshold values for noise intensity at different values of system damping ratio were predicted using the acquired system time responses. The obtained noise intensity thresholds exhibit a non-linear increasing trend with damping. Furthermore, variation in input angular velocity and mass mismatch have been found not to impose significant influence on system stability under typical gyroscope operating conditions.

# Chapter 5

## Experimental Results

### 5.1 Introduction

In this chapter, the variations in natural frequency due to angular rate as well as manufacturing imperfections are studied by employing an experimental setup. The secondary objective of the conducted experiments is to demonstrate the phenomena that might not be otherwise easily investigated through a MEMS sensor such as nonlinear behavior that arises due to the smallness of natural frequency of a macro-scale ring-type angular sensor. Phenomena such as variations in system natural frequency due to the presence of input angular rate and decreased uniform distribution of mass as well as the effect of fluctuations in angular rate on system behavior are studied.

The experiments that are conducted in the present chapter are merely a means of observation of the expected behavior and not reproduction of the numerical results presented in Chapter 4. Further validation of results against theoretical data is not feasible due to the differences in the geometries used in the analysis. The predicted numerical results are obtained using the properties of a MEMS-scale geometry while the experimental data involves a macro-scale ring. This results in a significant difference in system natural frequency and therefore the input

angular rate being relatively higher than a MEMS-scale ring. Furthermore, the vibrations in the experimental setup are of high amplitude making contact-less sensing feasible, detection of the vibrations and natural frequencies possible with the naked eye and thus, resulting in increased non-linearity of the system.

Similar to Chapter 4, an experiment has been designed in order to study the effects of fluctuations in input angular rate on system behavior. However, due to the limitations of the physical system, it is not yet possible to reproduce the obtained numerical results. Therefore, a preliminary experiment has been designed in order to reveal the effects of input fluctuation, the results of which can be used in future experiments on quantifying the effects of stochastic fluctuations in input angular rate.

## 5.2 Experimental Setup

The experimental setup consists of a long suspended C1095 blue-tempered cylindrical McMaster-Carr Supply Company steel shell with the properties summarized in Table 5.1. The shell is made by joining the two sides of a steel plate using spot welding and therefore natural variations in mass mismatch as well as damping and stiffness are expected. However, it should be noted that the analytical and numerical studies in the present thesis are performed with a micro-scale ring in mind. In order to overcome the complexities of manufacturing a MEMS ring as well as associated problems with excitation and sensing methods, the constructed long macro-scale cylinder was considered for the experimental analysis instead, due to the similarities between dynamic characteristics of a non-rotating ring structure and a non-rotating long cylindrical structure (Cho, 2009).

The dimensions of the ring were carefully chosen in order to achieve the required small thickness-to-radius ratio of a thin cylinder. Furthermore, the thickness of the ring at  $0.1016 \text{ mm}$  allows for non-linearities due to large amplitude vibration of more than four times the structure thickness.

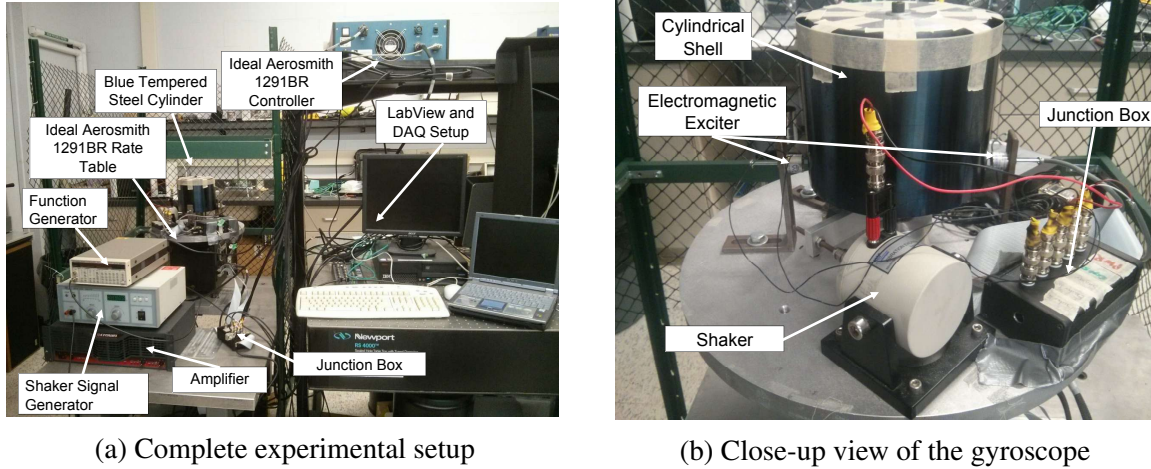


Figure 5.1: Experimental setup

The experimental setup is shown in Figure 5.1.

Property	Value
Density	$\rho = 7833.41 \text{ kg/m}^3$
Young's modulus	$E = 206.84 \times 10^9 \text{ N/m}^2$
Mean radius	$r = 92.5 \text{ mm}$
Radial thickness	$h = 0.1016 \text{ mm}$
Thickness-to-Radius Ratio	$h/r \approx 0.001$
Axial Length	$L = 150 \text{ mm}$

Table 5.1: Physical properties of the experimental ring

The top part of the shell is loosely fixed using symmetrically placed thin paper tapes to the axis of an Ideal Aerosmith 1291BR Precision Single-Axis Rate Table, while the bottom part of the cylinder is allowed to deform freely in the absence of any constraints conforming to the purpose of maximizing similarities to a thin ring. Ideal Aerosmith 1291BR Precision Rate Table is highly capable of producing constant speed angular rotation with high accuracy while employing slip-rings in order to enable signal routing to and from the rotating surface to a stationary device. Moreover, The cylindrical shell is chosen to be sufficiently long, minimizing the changes in mode shapes due to the tapes.

Excitation of the ring is made possible using a set of APW EM075-12-122 electromagnets, dis-

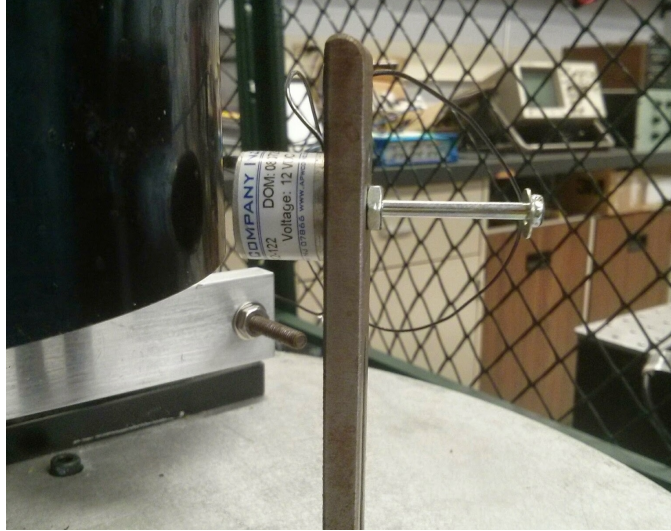


Figure 5.2: Configuration of an electromagnetic exciter.

played in Figure 5.2, and the resulting displacements are measured using two Lion Precision Eddy-Current probes. The electromagnets offer contactless excitation of vibration in the ring while offering control over the simulating signal. The external excitation signal is generated using a Stanford Research Systems DS345. The DS345 is capable of generating low frequency sinusoidal functions, as well as performing a linear frequency sweep, used for natural frequency detection. The generated signal is amplified using a Crown CE1000 amplifier while removing



Figure 5.3: Configuration of the Eddy-Current probes.

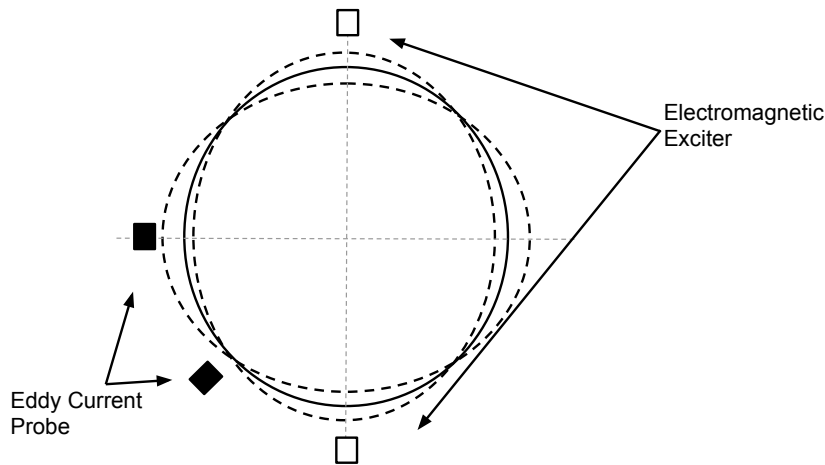


Figure 5.4: Schematic location of sensors and actuators.

the unwanted noise. Furthermore, Eddy-Current probes offer contact-less monitoring of displacement in low frequency bandwidth which allows for reduction of unnecessary constraints of the cylinder. A close-up view of the positioning of the Eddy-Current probes is displayed in Figure 5.3 and a schematic view of the location of exciters and sensors with respect to the ring mode shape is depicted in Figure 5.4. A Lion Precision ECL134 dual-channel driver is used for signal conditioning which allows for simultaneous monitoring of two probes. The output signals are routed towards a National Instruments data acquisition device and then analyzed via LabView software. Since the operating frequency of the system is observed and manually set to be about 1 Hz to 20 Hz, a sampling rate of 1 kHz is chosen in order to satisfy and exceed the requirements of Nyquist criterion by a large margin. The rate table employs slip rings which enables transmission of signal from devices on the rotating table to stationary amplifiers and data acquisition system. The details of the devices employed in the experimental setup as well as the wiring diagrams and the developed LabView scripts are discussed in Appendix C.

Initially, the positioning of sensors and exciters was assessed in the absence of angular rate with the ultimate purpose of demonstrating the natural frequency of the flexural modes as well as non-linearities of the system in mind. Complications occur when the sensors are placed



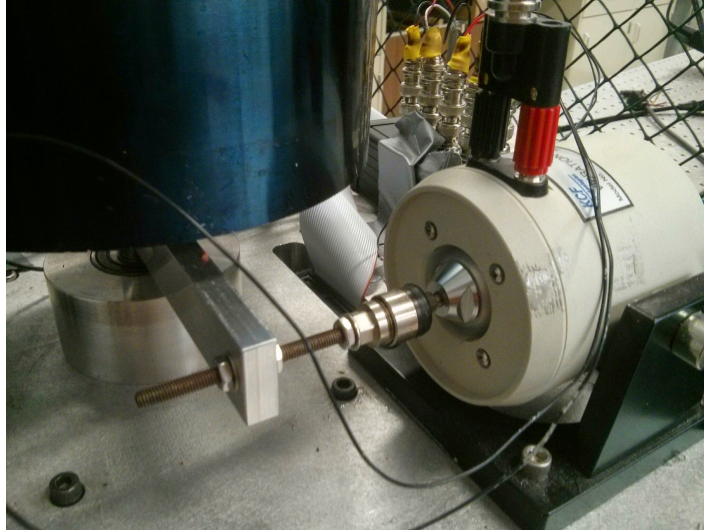


Figure 5.5: Implementation of stochastic angular rate fluctuation setup.

either too close to or too far from the cylinder. Placing the Eddy-Current sensors too close to the cylinder might result in collision of the cylindrical shell with the sensor under high amplitude vibration. On the other hand, placing the probes too far from the shell results in higher vibration amplitudes in the output signal. This is due to the fact that Eddy-Current sensors take advantage of changes in an induced magnetic field in order to detect presence of ferromagnetic material. This results in the presence of displacements that occur near the nodes on the output signal of the sensor. Therefore, the sensor location has to be optimized in order to avoid collision with the shell as well as high accuracy in detecting low amplitude vibration in sensitive points such as nodal points.

The electromagnets are placed along the diameter of the cylinder while maintaining symmetry. The excitation points correspond to anti-nodal points as the displacement of the ring is maximum at the excitation points. The eddy-current sensors are then placed accordingly at one nodal and one anti-nodal point in order to monitor the time and frequency response of the ring at different physical and nodal points. The sensor positions are referred to as nodal point and anti-nodal point from here on corresponding to nodal and anti-nodal points in the first configuration of the second flexural mode. Furthermore, excitation and measurements are performed

on the free end of the cylinder conforming to the objective of simulating a free-standing ring.

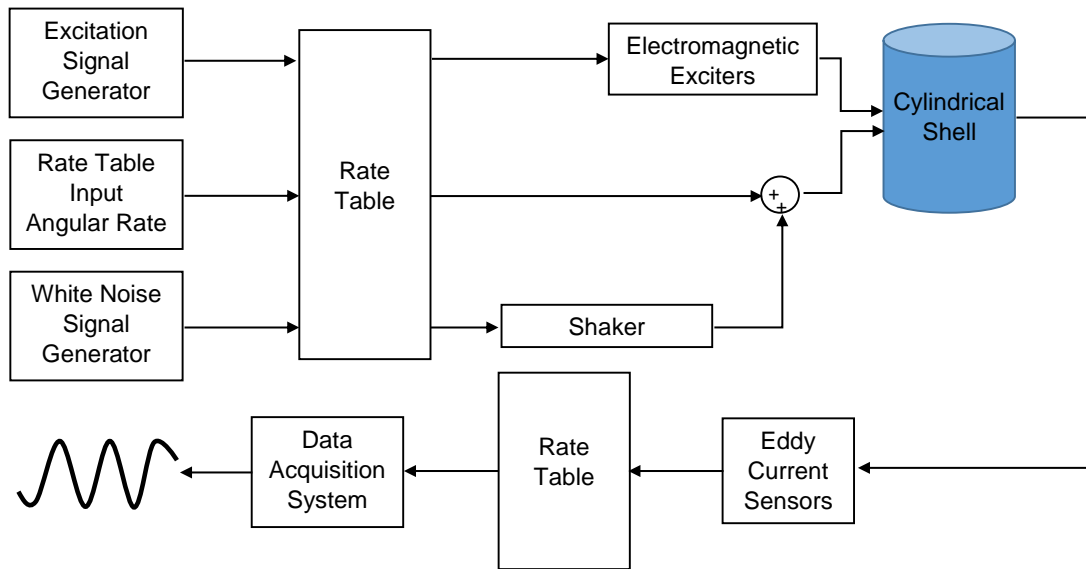


Figure 5.6: Block diagram representation of the experimental setup.

Finally, a shaker system has been employed for the purpose of simulating environmental white noise fluctuation in the angular rate. A KCF Vibration Exciter paired with a KCF PA5100 Signal Generator/Power Amplifier is used for this purpose. The PA5100 system is considered suitable for this purpose due to the capability to generate white noise as well as low-frequency sinusoidal motion. The shaker is placed on the rate table and connected to the rate table axis through a welded steel beam. This ensures that the fluctuations caused by the shaker are transferred to the ring while the desired average angular rate is maintained. The shaker as well as the fixtures connecting the output rod with the rate table axis is shown in Figure 5.5. The complete block diagram and schematic representations of the experimental setup can be seen in Figures 5.6 and 5.7. The details of the system wiring along with more details on the experimental setup can be found in Appendix C.

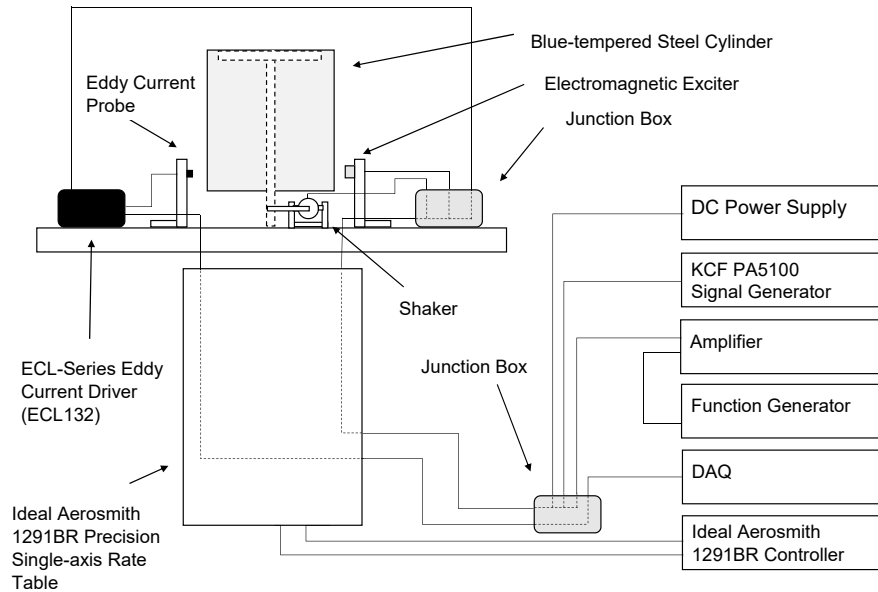


Figure 5.7: Schematic representation of the experimental setup.

### 5.3 Experimental Results and Discussion

In the initial phase of experiments, the bifurcation of the two flexural configurations due to angular rate was studied. To this end, the ring was excited using a linear sinusoidal wave frequency sweep. The correlation of the resulting ring response was then found against the exciter signal. The results are displayed in Figure 5.8.

The peak in Figure 5.8 corresponds to the natural frequency of the ring for the first flexural configuration. As it is shown in Figure 5.8, the resonance frequency of the ring is reduced in the rotating ring when compared to a stationary ring conforming to the expected result from the frequency analysis in Chapter 2. The natural frequency of the second configuration is increased in return resulting in a bifurcation in natural frequencies of the second mode shape. However, the two natural frequencies take close values under low angular velocities to which gyroscopes

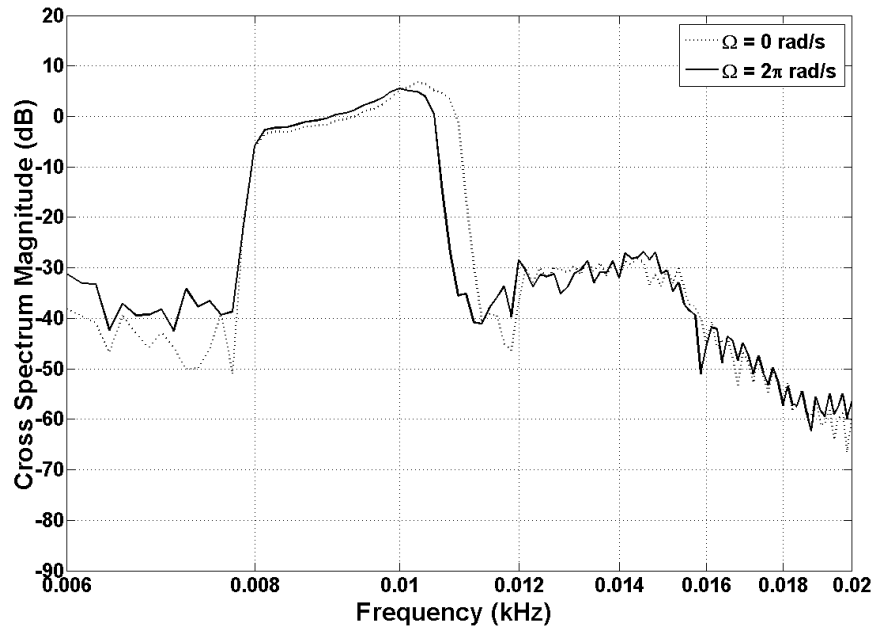


Figure 5.8: Natural frequency shift in the Cross Spectrum Magnitude diagram due to angular rotation.

are typically subjected. In addition, the effects of other mode shapes that are not accounted for in the present research can also contribute to the detection of the natural frequencies, making the bifurcation difficult to observe.

Following the study of frequency shift due to angular rate, the non-linear characteristic of the sensor response were analyzed by monitoring the energy transfer between the two second mode flexural configurations as a result of Coriolis force. The vibration amplitude at a nodal point and at an anti-nodal point are recorded and compared for this purpose. The natural frequency of the ring in Figure 5.8 was chosen as the excitation frequency, warranting large vibration amplitude. Figure 5.9 shows the variations of vibration amplitude at nodal and anti-nodal points with angular rate with the structure being excited at the stationary resonance frequency.

It can be seen that the vibration amplitude does not exhibit an apparent trend at low angular rates. However, the energy transfer from the first configuration to the second becomes apparent

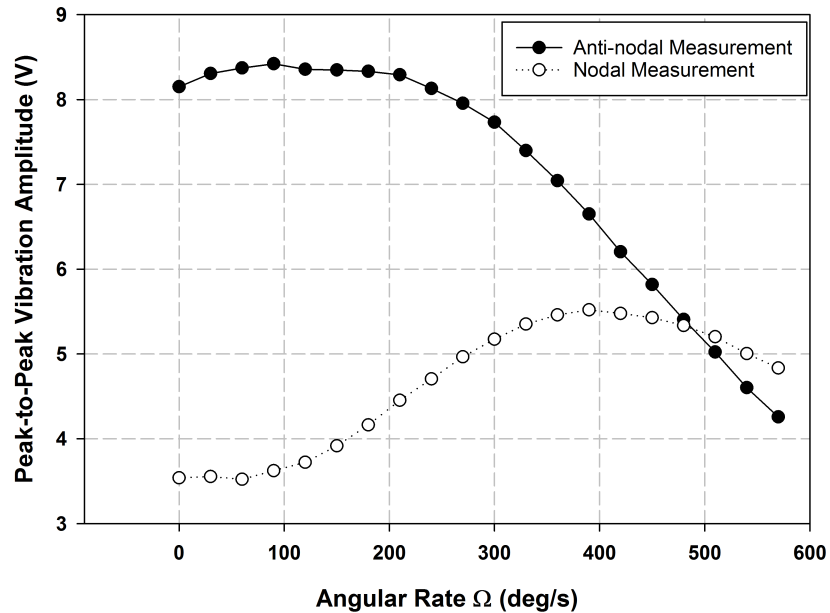


Figure 5.9: Linearity of nodal and anti-nodal measurements.

in the anti-nodal point at angular velocities of about  $210 \sim 240^\circ/s$ . It is interesting to note that the increase in vibration at the node is detected at lower angular velocities of about  $90^\circ/s$ .

Measurements made at the anti-nodal point exhibit acceptable linearity for input angular rates of up to  $500^\circ/s$  while linearity is drastically decreased at the nodal point at  $300^\circ/s$ . It was found that the linearity of the device is highly dependent on the excitation frequency, as expected from the preceding analysis. The non-linearity of the devices may be attributed to high vibration amplitudes as well as the low natural frequency of the device, recorded at 10.4 Hz. This results in a high angular rate to natural frequency ratio as opposed to typical MEMS sensors which are designed with high natural frequencies in the  $kHz$  range and detection angular rates of  $0 \sim 2\pi$  rad/s. Furthermore, the usage of eddy-current sensors for the current setup presents difficulties in accurate measurement of vibration at nodal points due to their measurement technique. Eddy-current sensors operate by creating a magnetic field close to the sensor and detecting the disturbance in the created field caused by an object. Therefore, any vibration in the proximity of the node will also contribute to the measured signal.

Manufacturing defects play an important role in the discussed non-linearities as well as frequency analysis of the ring. Increased non-uniformity in mass distribution of the ring could

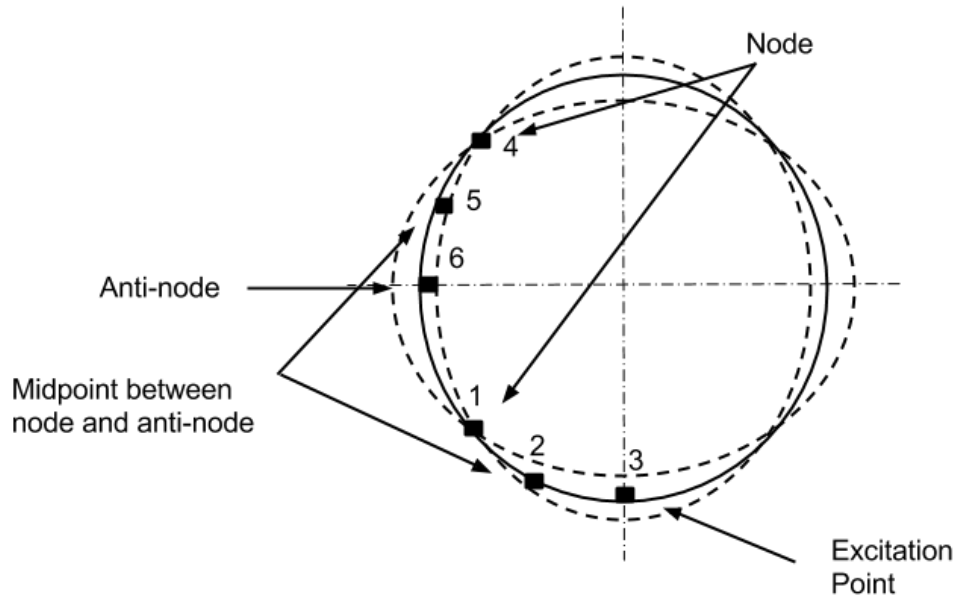


Figure 5.10: Suggested locations for mass anomaly.

result in further bifurcation and variation in system natural frequencies as demonstrated in Figure 2.3. The occurrence of defects can be controlled by employing accurate manufacturing and machining processes. However, it is necessary to study the effects of non-uniformity in mass on ring performance since such defects cannot be completely prevented during the manufacturing process. For this purpose, mass anomalies were placed on the ring and the peak-to-peak amplitude of the sensor output was measured at a range of frequencies in order to determine the natural frequency of the first flexural configuration.

In addition to investigating the quantity of the mass anomaly, the significance of the position of the anomaly with respect to the second flexural mode shape was also assessed. Figure 5.10 shows a schematic of the locations considered for investigation relative to the mode shape. Two nodal points, one anti-nodal point and the excitation point as well as an arbitrary point located at the mid-point between the nodes and anti-nodes were chosen for this purpose.

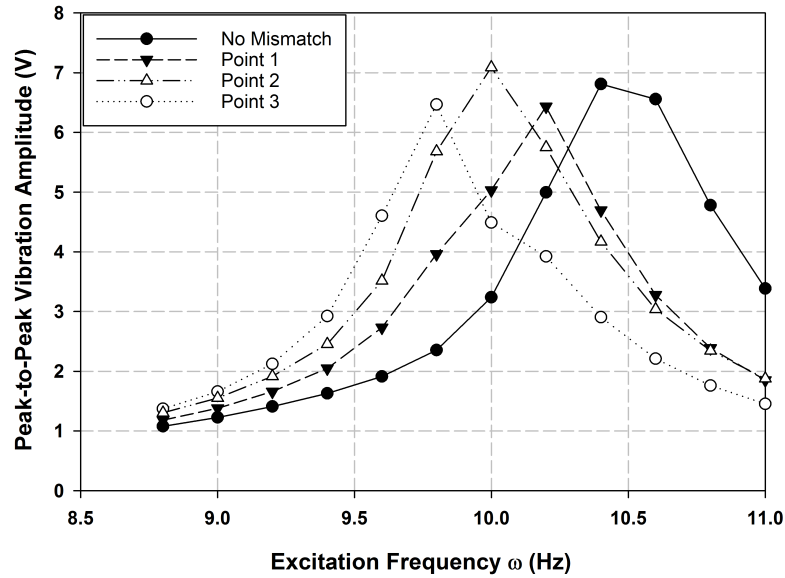


Figure 5.11: Anti-nodal measurements of time response for 2.5% mass mismatch located at points 1 to 3.

Initial study of the remaining nodal and anti-nodal points did not reveal noticeable deviation of natural frequency when compared to the axially symmetrical counterparts. Therefore, it is sufficient to study the points on one quarter of the ring surface due to symmetry. However, in the current study, the results from the the second quarter of the ring surface are also considered in order to demonstrate the effects of placing the mass anomaly at symmetrical points on the ring.

Figure 5.11 shows the variation of peak-to-peak vibration amplitude due to 2.5% mass mismatch relative to total mass of the ring at points 1, 2 and 3 along the ring circumference using the measurements made at the anti-nodal point. It can be seen that an increase in non-uniformity in mass distribution results in a reduction of the first natural frequency of the second flexural mode. Analytical study performed in Chapter 2 suggests that the second natural frequency is increased as a result of reduced mass uniformity. However, the second natural frequency is not easily detectable in the present macro-scale ring-type gyroscope. Further analysis

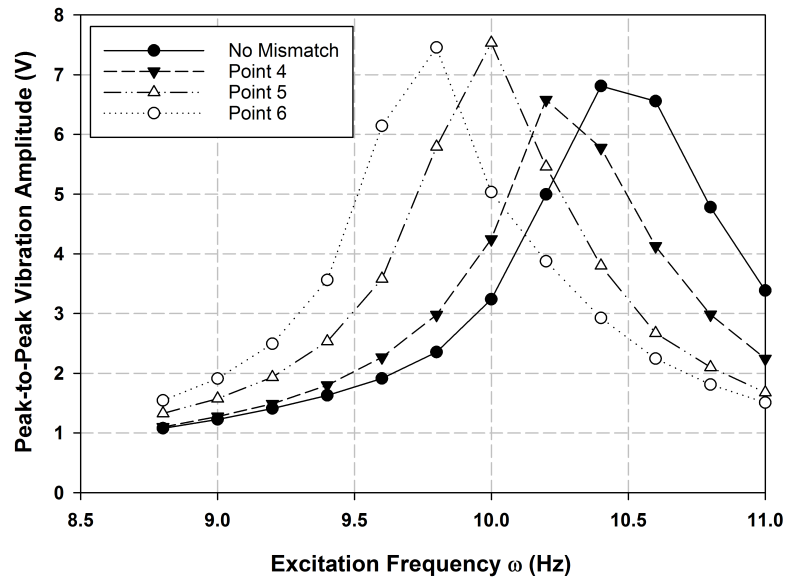


Figure 5.12: Anti-nodal measurements of time response for 2.5% mass mismatch located at points 4 to 6.

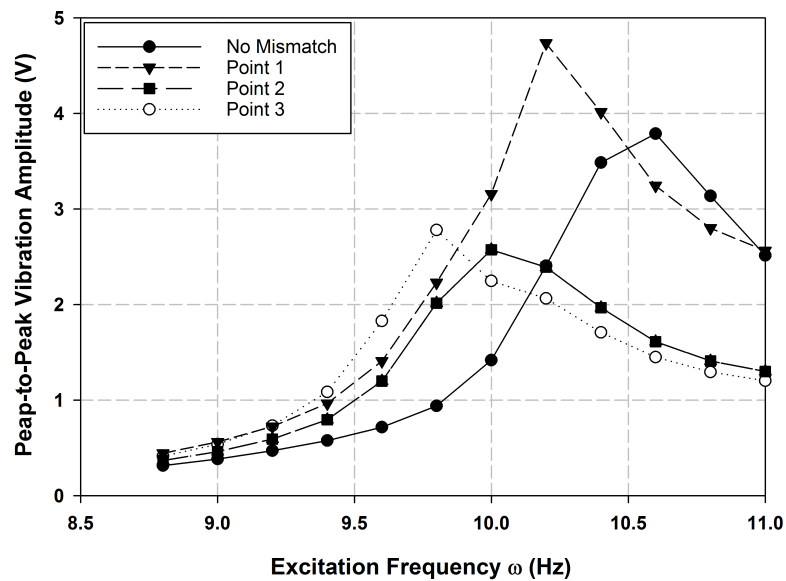


Figure 5.13: Nodal measurements of time response for 2.5% mass mismatch.



of Figure 5.11 reveals that the location of mass anomaly has significant effect on the decrease in natural frequency. It can be seen that while the first natural frequency of the non-rotating ring is  $10.6 \text{ Hz}$ , when the  $2.5\%$  mass mismatch is placed at the nodal point the frequency is reduced to  $10.2 \text{ Hz}$ . Furthermore, the natural frequency is decreased further when the mass is moved away from the nodal point and closer to the anti-nodal point. The minimum natural frequency of  $9.8 \text{ Hz}$  occurs when the mass is placed at one of the anti-nodal points.

Symmetrical counterparts of points 1,2 and 3 reveal similar natural frequencies. Peak-to-peak measurements at the anti-node for anomaly locations 4,5 and 6 can be seen in Figure 5.12.

Figure 5.13 shows the nodal measurements for variation of the first natural frequency for different locations of the  $2.5\%$  mass mismatch. It can be seen that the measurements from the nodal point and anti-nodal point demonstrate similar natural frequencies with negligible error due to high measurement error from unwanted vibration near the node as well as high frequency signal noise and averaging error. Hence, the anti-nodal measurements are chosen for further mass mismatch analysis due to the larger peak-to-peak amplitude of vibration and minimal effect of

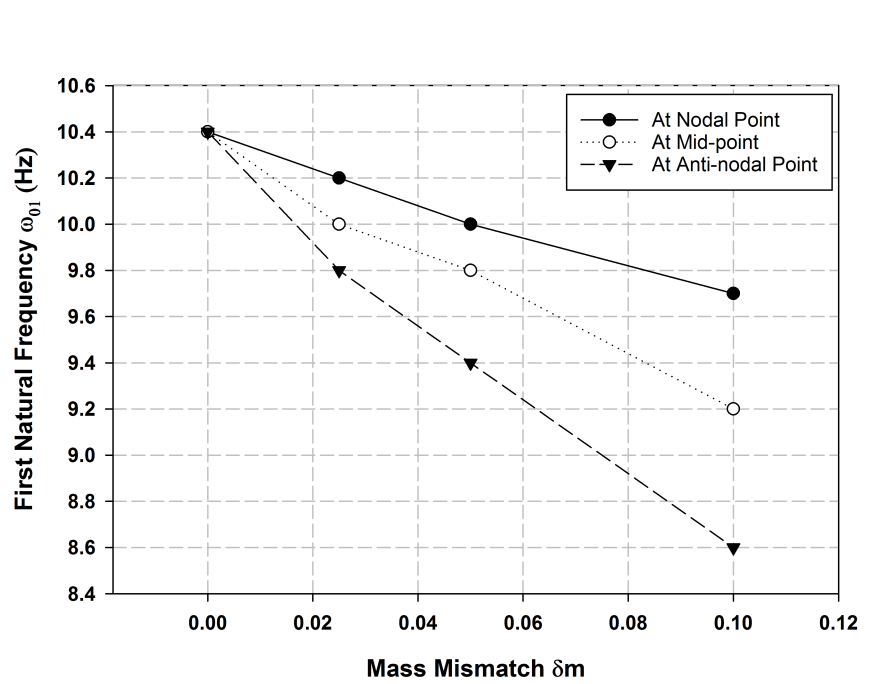


Figure 5.14: Variation of natural frequency with mass mismatch - experimental results.

nearby vibration on the anti-nodal measurement. Summary of the obtained resonance frequencies can be seen in Table 5.2. It should be noted that the resonance frequencies are found by manually changing the excitation frequency of the system and making observations based on peak-to-peak voltage of the output signal. Figure 5.14 displays the effects of the quantity of

Concentrated Mass Location	Resonance Frequency Using Nodal Probe (Hz)	Resonance Frequency Using Antinodal Probe (Hz)
No mismatch	10.6	10.4
Point 1	10.2	10.2
Point 2	10.0	10.0
Point 3	9.8	9.8
Point 4	10.4	10.2
Point 5	10.2	10.0
Point 6	9.8	9.8

Table 5.2: Summary of measurements with concentrated mass located at different points on the ring.

localized mass at different locations on the ring. Experiments have been conducted by placing localized mass anomalies of 2.5%, 5% and 10% of total ring mass and the natural frequency of the first configuration for the second flexural mode of the ring has been found through peak detection on peak-to-peak amplitude versus excitation frequency curves.

It can be seen that increasing the mass of the anomaly results in a decrease in the natural frequency of the first configuration of the second flexural mode. Furthermore, the figure shows that the effect of mass concentration is larger when the mass is located in the vicinity of anti-nodal points. Results suggest that a concentrated mass of 10% the mass of the ring can result in a 0.7 Hz drop in natural frequency when placed at a nodal point and a 1.8 Hz decrease when located at an anti-nodal point.

## 5.4 Stochastic Fluctuation in Angular Rate

Analytical and numerical studies show that environmental fluctuations in angular rate affect the dynamic stability of MEMS ring-type gyroscopes. This proposes the question whether these fluctuations continue to have a significant effect on macro-scale systems as well. To this end, a shaker system was considered in order to simulate environmental fluctuations and study the resulting effects on system stability. Environmental fluctuations demonstrate stochastic behavior. Hence, as discussed in Chapter 3, white noise can be used for studying the effects of fluctuations while covering a large spectrum of frequencies. Figure 5.15 demonstrates the effect of fluctuations on vibration of the stationary ring while showing the output of both nodal and antinodal probes.

It can be seen that high frequency fluctuation has a significant influence on the stationary ring under pure fluctuation. However, low frequency fluctuation does not seem to have visible effect on the system. This interesting observation can be contrasted with a rotating ring under fluctuation. Effects of fluctuation on the output signals of a rotating ring can be seen in Figure 5.16.

It can be seen that with a rotating ring, the effects of high frequency fluctuation is less visible

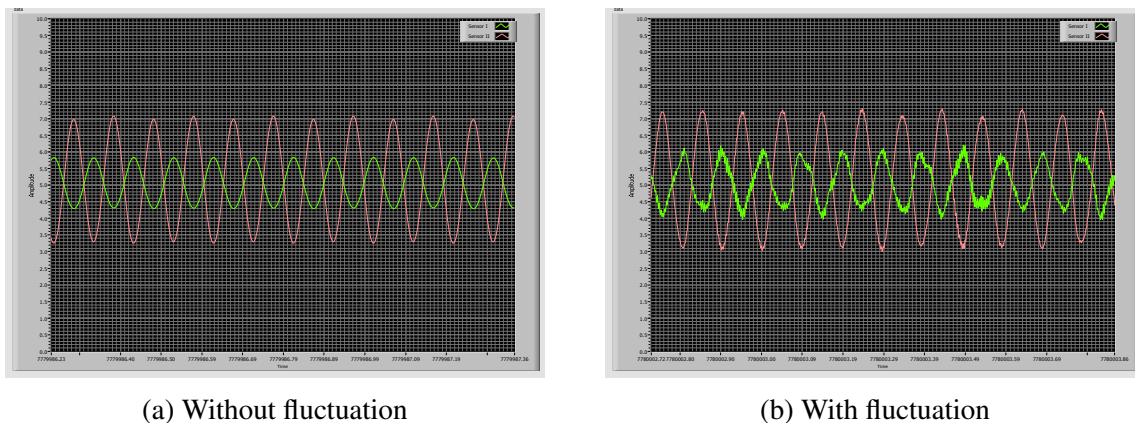


Figure 5.15: Effects of fluctuations in angular rate on raw sensor measurements,  $\Omega = 0$  rad/s.

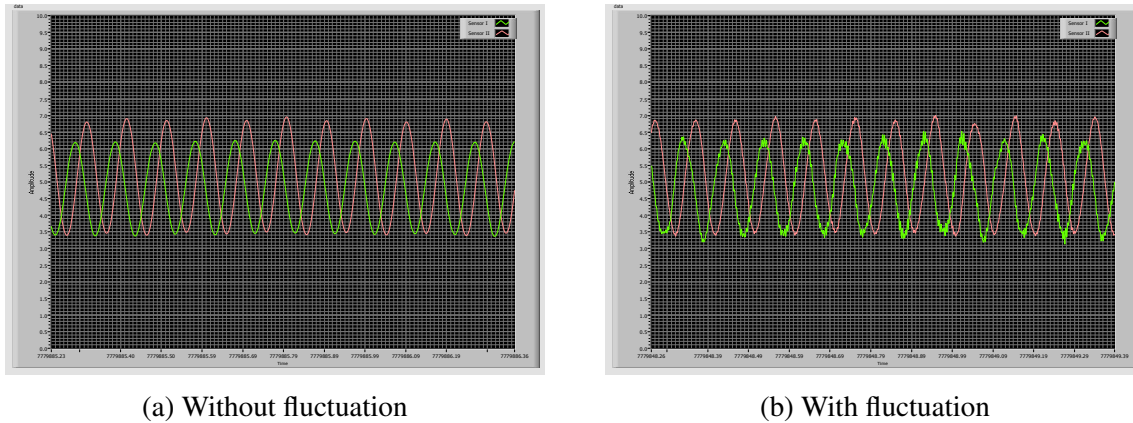


Figure 5.16: Effects of fluctuations in angular rate on raw sensor measurements,  $\Omega = 2\pi$  rad/s.

compared to a stationary ring. This effect may be a result of the changes in system stiffness due to rotation. Furthermore, low frequency fluctuations are more visible with the absence of high frequency noise.

The preliminary noise study conducted in the present thesis can be used as a reference in order to perform a parametric study on environmental fluctuation similar to the numerical study performed in Chapter 4. For this purpose, the input angular rate to the system is subjected to uniformly distributed fluctuations through the white noise function of the shaker. The amplitude of the fluctuations is held constant while the angular rate is changed in order to monitor the ability of the system in damping unwanted fluctuations. Twenty vibration cycles are documented for each angular rate both with and without the presence of noise. The results are then subtracted in order to find the pure noise output of the system. The standard deviation of the resulting noise data is then calculated and averaged by taking ten data samples consisting of ten vibration cycles each. The samples are formulated in such a way so that the first sample includes cycles 1 through 10, the second sample includes cycles 2 through 11, the third sample includes cycles 3 through 12 and so on. This methods allows for assessment of confidence in the obtained data by using 10 data samples and examining the standard deviation of the data points as a measure of output fluctuation intensity. Having the mean standard deviation of the output data, the 95-percent confidence interval for the obtained data can also be calculated us-

ing the t-distribution table (Peters, 2001). Figure 5.17 shows the standard deviation values for different input angular rates with fixed fluctuations. The 95-percent confidence intervals for the mean standard deviation values can also be seen.

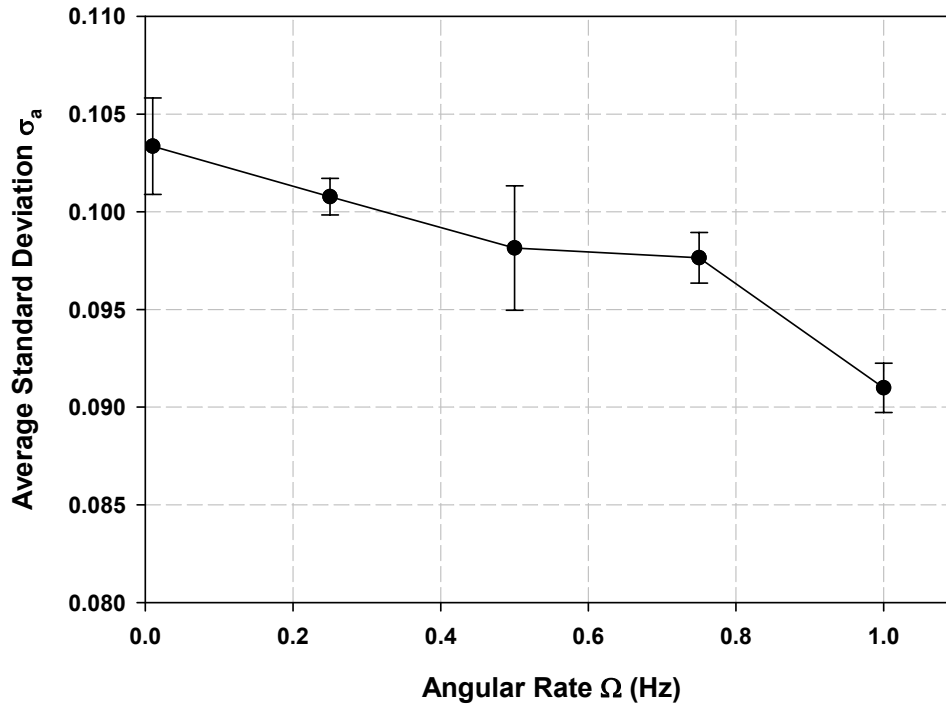


Figure 5.17: Variation of output standard deviation with angular rate.

It can be seen that by increasing the angular rate while applying constant fluctuation to the input rate, the amount of visible fluctuation on the output data of the vibratory sensor is reduced. This reduction may be associated with the reduction of relative noise-to-nominal ratio of the input angular rate as the noise is kept at a constant level. Furthermore, an increase in angular rate, as shown earlier in the chapter, results in variations in system natural frequency, as well as effective system stiffness and damping mostly due to centrifugal forces. The current system exhibits limitations on the amount of noise that can be added to the system input. This is partly due to the damping and inertia of the connecting beams and shafts between the shaker and the ring. A more direct method of noise implementation is recommended in order to reach higher noise-to-nominal ratio of input angular rate. These results can be used in order to assess

the effects of uncertainty in other input parameters such as the frequency and amplitude of the external excitation signal.

## 5.5 Closure

An experimental macro-scale ring-type gyroscope has been developed in order to study the dynamic behavior of ring-type gyroscopes as well as the non-linear behavior of the device. A long thin cylindrical shell is used for this purpose. The shell is installed on a precision rate table with the free hanging bottom part of the shell mimicking a thin ring. Electromagnetic exciters were used in order to excite forced vibration in the ring along with two eddy-current sensors at nodal and anti-nodal locations. Variation of natural frequency with angular rate has been shown to agree with theoretical results. Moreover, it was shown that the device exhibits high non-linearity which may be due to the low natural frequency of the system as well as high vibration amplitudes. Furthermore, the effects of increasing non-uniformity in mass distribution along the circumference of the ring has been studied. It was found that increasing mass mismatch reduces the natural frequency of the system when compared to a system with lower mass mismatch as predicted by the analytical results. Furthermore, effects of fluctuation in angular rate on a rotating a non-rotating ring were observed. Development of the current system as well as the preliminary study performed on fluctuations in angular rate can be used in order to assess the effects of environmental noise on dynamic behavior of this class of gyroscopes. It was found that the system exhibits a more efficient damping of fluctuations when subjected to higher angular rates.

# Chapter 6

## Conclusion

Stability of ring-based gyroscopes subjected to random fluctuation in the angular velocity is studied using a two DOF dynamic model developed for flexible circular rings. Resulting equations of motion have been shown to predict the response in the driving as well as the sensing directions of the gyroscope. The fluctuation has been assumed to be represented using standard white noise and the associated Stochastic Differential Equations have been formulated employing the Milstein scheme to predict the system response. Due to lack of analytical or experimental data in the literature, response predictions via Euler scheme as well as the Largest Lyapunov Exponents have been used for validation. The predicted threshold values for noise intensity at different values of damping exhibit a non-linear increasing trend. Variation in input angular velocity and mass mismatch have been found not to impose significant influence on system stability under typical gyroscope operating conditions.

Furthermore, an experimental macro-scale ring-based gyroscope is completed and tested in order to study the dynamic behavior and non-linearities of a macro-scale systems of this class. Variations in natural frequency of the system is documented while increasing the input angular rate as well as the non-uniform distribution of mass on the ring. It was found that higher angular rates and increased mass mismatch result in a noticeable reduction in system natural frequency, as predicted by the equations of motion and numerical simulations. In addition,

effects of fluctuations in input angular rate on the system is investigated. While the system maintains a stable behavior, the system exhibits more efficient damping of the fluctuations at higher angular rates.

## 6.1 Thesis Contributions

The original contributions of the present thesis are summarized as follows:

- The equations of motion of a MEMS ring-based vibratory sensor have been rewritten considering environmental fluctuations in input angular rate in the form of white noise. The equations have then been transformed into the standard format of a Stochastic Differential Equation and the higher-order Milstein scheme has been employed in order to develop an algorithm for numerical simulation of the equations of motion.
- The obtained numerical predictions have been validated against the more commonly used Euler scheme. Accuracy of the developed computer code in predicting system stability has been confirmed using the Largest Lyapunov Exponents method. A parametric study has been conducted in order to obtain a noise intensity threshold for systems with different damping ratio values. A non-linearly increasing trend has been found for the stability threshold of the system at higher damping ratios.
- An experimental macro-scale setup has been constructed and tested. Improvements have been made in user friendliness and ease of maintenance of the system. Safety measures and user instruction manuals have been developed in order to insure safe start-up, operation and shutdown of the devices.
- Experiments have been conducted in order to study the variations of system natural frequency while the system is subjected to increasing input angular rates. Effects of reducing the uniform distribution of mass along the circumference of the macro-scale ring



have been investigated and system behavior when subjected to stochastic fluctuations in input angular rate is documented and analyzed.

## 6.2 Recommendations for Future Research

The present thesis attempted to employ the higher-order numerical schemes used for Stochastic Differential Equations in order to investigate the dynamic behavior of MEMS ring-based gyroscopes and conduct a parametric study on effects of fluctuation intensity for the first time. Furthermore, a macro-scale ring-based gyroscope has been developed in order to study the non-linear behavior of this class of systems in larger scales. The tools and results that have been developed during this thesis can be used in order to:

- Investigate the effects of random vibration and unwanted fluctuations on other classes of vibratory angular rate sensors using the higher-order Milstein scheme as developed during the current research. And also to use the developed stochastic model in order to numerically simulate and study gyroscopic systems in real-world scenarios, therefore eliminating the need for prototype development and reducing costs.
- Conduct experimentation on the effects of higher than typical input angular rates on system behavior by enhancing the current setup for high angular rates. The typical gyroscopic system is designed in order to maintain a natural frequency in the order of kilohertz or megahertz while the system is subjected to input angular rates of lower than  $2\pi$  Hz. The low natural frequency of the current setup allows for more insight into the behavior of this class of systems at extremely high angular rates.
- Employ the obtained results and methods used in assessment of environmental fluctuations on the ring in order to conduct parametric studies on the effects of fluctuations on system stability similar to the numerical study in Chapter 4. Also, the preliminary

fluctuation study opens the way to further the experiments conducted on environmental fluctuation by considering uncertainties in the frequency and amplitude of the system excitation force. Initial investigations reveal the system exhibits different characteristics on uncertainty of the output signal when subjected to slight variations in excitation parameters.

- Investigate the effects of physical properties and inherent uncertainties of the ring, such as system stiffness on the behavior of ring-based gyroscopes as well as non-constrained cylindrical structures.

# Bibliography

Nujhat Abedin. Uncertainty quantification for a class of mems-based vibratory angular rate sensors. *University of Western Ontario - Electronic Thesis and Dissertation Repository*, 2014.

Samuel F Asokanthan and Jihyun Cho. Dynamic stability of ring-based angular rate sensors. *Journal of sound and vibration*, 295(3):571–583, 2006.

Samuel F Asokanthan and Tianfu Wang. Instabilities in a mems gyroscope subjected to angular rate fluctuations. *Journal of Vibration and Control*, 15(2):299–320, 2009.

Samuel F Asokanthan, S T Ariaratnam, Jihyun Cho, and Tianfu Wang. Mems vibratory angular rate sensors: Stability considerations for design. *Structural Control and Health Monitoring*, 13(1):76–90, 2006.

Farrokh Ayazi and Hourii Johari. Capacitive bulk acoustic wave disk gyroscopes, June 9 2009. US Patent 7,543,496.

Farrokh Ayazi and Khalil Najafi. Design and fabrication of high-performance polysilicon vibrating ring gyroscope. In *Micro Electro Mechanical Systems, 1998. MEMS 98. Proceedings., The Eleventh Annual International Workshop on*, pages 621–626. IEEE, 1998.

Gregory L Baker and Jerry P. Gollub. *Chaotic Dynamics: an Introduction*. Cambridge University Press, 1990.

- George H Bryan. On the beats in the vibrations of a revolving cylinder or bell. In *Proceedings of the Cambridge Philosophical Society*, volume 7, pages 101–111, 1890.
- Jihyun Cho. Dynamic response and stability of ring-based vibratory angular rate sensors. Master's thesis, The University of Western Ontario, 2005.
- Jihyun Cho. *Nonlinear Instabilities in Ring-based Vibratory Angular Rate Sensors*. PhD thesis, The University of Western Ontario, 2009.
- William A Clark. Micromachined z-axis vibratory rate gyroscope, November 30 1999. US Patent 5,992,233.
- R Eley, C H J Fox, and S McWilliam. Coriolis coupling effects on the vibration of rotating rings. *Journal of sound and vibration*, 238(3):459–480, 2000.
- Leon Foucault. Sur un nouvelle démonstration expérimentale du mouvement de la terre fondée sur la fixité du plan de rotation. *CR Acad. Sci*, 35:421, 1852.
- Stefan Günthner, Markus Egretzberger, Andreas Kugi, Konrad Kapser, Bernhard Hartmann, Ulrich Schmid, and Helmut Seidel. Compensation of parasitic effects for a silicon tuning fork gyroscope. *Sensors Journal, IEEE*, 6(3):596–604, 2006.
- AJ Harris, JS Burdess, D Wood, R Langford, G Williams, MCL Ward, and ME McNie. Issues associated with the design, fabrication and testing of a crystalline silicon ring gyroscope with electromagnetic actuation and sensing. *Journal of Micromechanics and Microengineering*, 8(4):284, 1998.
- Desmond J Higham. An algorithmic introduction to numerical simulation of stochastic differential equations. *SIAM review*, 43(3):525–546, 2001.
- Desmond J Higham and Peter E Kloeden. Maple and matlab for stochastic differential equations in finance. In *Programming Languages and Systems in Computational Economics and Finance*, pages 233–269. Springer, 2002.

- Shyh-Chin Huang and Werner Soedel. Effects of coriolis acceleration on the free and forced in-plane vibrations of rotating rings on elastic foundation. *Journal of Sound and Vibration*, 115(2):253–274, 1987.
- Christopher Jekeli. *Inertial Navigation Systems with Geodetic Applications*. de Gruyter, 2001.
- Daniel C Kammer and Alois L Schlack Jr. Effects of nonconstant spin rate on the vibration of a rotating beam. *Journal of Applied Mechanics*, 54(2):305–310, 1987.
- Volker Kempe. *Inertial MEMS: Principles and Practice*. Cambridge University Press, 2011.
- B Kliková and Aleš Raidl. Reconstruction of phase space of dynamical systems using method of time delay. In J Safrankova and J Pavlu, editors, *WDS'11 Proceedings of Contributed Papers: Part III - Physics*, pages 134–137, Prague, Czech Republic, 2011. Matfyzpress.
- Peter E Kloeden and Eckhard Platen. *Numerical Solution of Stochastic Differential Equations*, volume 23. Springer Science & Business Media, 1992.
- Anthony Lawrence. *Modern Inertial Technology*. Springer-Verlag, 1993.
- D Loukianov, R Rodloff, H Sorg, and B Stieler, editors. *Optical Gyros and Their Applications*. RTO/NATO, 1999.
- Augustus Edward Hough Love. *A Treatise on the Mathematical Theory of Elasticity*. Cambridge University Press, 2013.
- Nadim Maluf and Kirt Williams. *Introduction to Microelectromechanical Systems Engineering*. Artech House, 2004.
- Thomas Mikosch. *Elementary Stochastic Calculus with Finance in View*. World Scientific Publishing Co. Pte. Ltd., 1999.
- Charles T Morrow. Steady state response of the sperry rate gyrotron or vibratory gyroscope. *The Journal of the Acoustical Society of America*, 27(1):56–61, 1955.

- Catherine A Peters. Statistics for analysis of experimental data. In *Environmental Engineering Processes Laboratory Manual*. AEESP, Champaign, IL, 2001.
- William H Quick. Theory of the vibrating string as an angular motion sensor. *Journal of Applied Mechanics*, 31(3):523–534, 1964.
- Michael T Rosenstein, James J Collins, and Carlo J De Luca. A practical method for calculating largest lyapunov exponents from small data sets. *Physica D: Nonlinear Phenomena*, 65(1): 117–134, 1993.
- James Scarborough. *The Gyroscope; Theory and Applications*. Interscience Publishers, Inc., 1958.
- Thomas Schaffter. Numerical integration of sdes: a short tutorial. Swiss Federal Institute of Technology in Lausanne (EPFL), Switzerland, 2010.
- Jan Söderkvist. Micromachined gyroscopes. *Sensors and Actuators A: Physical*, 43(13):65 – 71, 1994.
- Werner Soedel. *Vibrations of Shells and Plates*. CRC Press, 2004.
- Jörg F Wagner. From bohnenbergers machine to integrated navigation systems, 200 years of inertial navigation. *Photogrammetric Week, Wichmann Verlag, Heidelberg*, 2005.
- Junbo Wang, Li Chen, Ming Zhang, and Deyong Chen. A micro-machined vibrating ring gyroscope with highly symmetric structure for harsh environment. In *Nano/Micro Engineered and Molecular Systems (NEMS), 2010 5th IEEE International Conference on*. IEEE, 2010.
- Alan Wolf, Jack B Swift, Harry L Swinney, and John A Vastano. Determining lyapunov exponents from a time series. *Physica D: Nonlinear Phenomena*, 16(3):285–317, 1985.
- Rob Yates. Micromachined gyroscopic sensors. *Sensor Review*, 19(1):43–45, 1999.

Navid Yazdi, Farrokh Ayazi, and Khalil Najafi. Micromachined inertial sensors. *Proceedings of the IEEE*, 86(8):1640–1659, 1998.

# Appendix A

## Derivation of Equations of Motion

### A.1 Introduction

In this chapter, the details of the derivation process for equations of motion as well as system natural frequencies are discussed. The complete derivation process along with analytical analysis of the system can be found in Cho (2005).

### A.2 Energy Equations

The total kinetic energy of the system consisting of the vibratory and rigid body motions of a ring rotating with angular velocity  $\Omega$  can be formulated as:

$$T = \frac{\rho A r}{2} \int_0^{2\pi} |\mathbf{v}|^2 d\theta, \quad (\text{A.1})$$

where  $\rho$  represents the density of the ring and  $A = b \times h$  denotes the cross-sectional area of the ring considering width  $b$  and thickness  $h$  as shown in Figure 2.1. The amplitude squared of the



velocity vector for a ring element can be written as: (Cho, 2005):

$$\begin{aligned} |\mathbf{v}|^2 &= (\dot{u}_r - u_\theta \Omega)^2 + (\dot{u}_\theta + u_r \Omega + r\Omega)^2 \\ &= (\dot{u}_r^2 + \dot{u}_\theta^2) + \Omega^2(u_\theta^2 + u_r^2 + 2ru_\theta) + 2\Omega(\dot{u}_\theta u_r - \dot{u}_r u_\theta + ru_\theta). \end{aligned} \quad (\text{A.2})$$

For the purpose of calculating strain energy of the ring, it is assumed that transverse shear and radial deflections can be neglected based on the thin ring assumption. Considering the nonlinearities resulting from large deformations and assuming linear elastic properties for the ring, strain energy of the ring can be formulated as:

$$\begin{aligned} U &= \int_V \left[ \frac{1}{2} \sigma_\theta \varepsilon_\theta + \frac{1}{2} \sigma_{r\theta} \varepsilon_{r\theta} + \sigma_\theta^i (\varepsilon_\theta + \varepsilon_\theta^i) \right] dV \\ &= br \int_{-h/2}^{h/2} \int_0^{2\pi} \left[ \frac{1}{2} \sigma_\theta \varepsilon_\theta + \frac{1}{2} \sigma_{r\theta} \varepsilon_{r\theta} + \sigma_\theta^i (\varepsilon_\theta + \varepsilon_\theta^i) \right] d\theta d\alpha_3, \end{aligned} \quad (\text{A.3})$$

where  $\sigma_\theta$ ,  $\sigma_{r\theta}$  and  $\sigma_\theta^i$  correspond to normal stress component in the circumferential direction, shear stress and normal stress due to centrifugal force, respectively. The potential energy associated with the eight springs supporting the ring can be written as:

$$V = br \int_0^{2\pi} \frac{1}{2} (k_r u_r^2 + k_\theta u_\theta^2) d\theta, \quad (\text{A.4})$$

where  $k_r$  and  $k_\theta$  respectively denote the stiffness in radial and circumferential directions. Finally, the energy component due to external loads can be formulated to be:

$$E_L = br \int_0^{2\pi} (f_r u_r + f_\theta u_\theta) d\theta, \quad (\text{A.5})$$

where  $f_r$  and  $f_\theta$  denote the applied forces in radial and circumferential directions, respectively. Total energy of the ring can be calculated having the energy components. Hamilton's principle can be applied to the differential variation in total energy using arbitrary time domains

$[t_0, t_1]$ , in order to obtain the equations of motion:

$$\delta \int_{t_0}^{t_1} (U + V - T - E_L) dt = 0. \quad (\text{A.6})$$

Examining the energy terms individually and carrying the equation yield the equations of motion for the ring as

$$\begin{aligned} -\frac{EA}{br^2}(u''_{\theta} + u'_r) - \frac{EI}{br^4}(u''_{\theta} - u'''_r) + \rho h \Omega^2(-2u'_r - u''_{\theta}) \\ + k_{\theta}u_{\theta} + \rho h(\ddot{u}_{\theta} + \dot{\Omega}u_r + 2\Omega\dot{u}_r) = f_{\theta}, \end{aligned} \quad (\text{A.7})$$

in the circumferential direction, and

$$\begin{aligned} \frac{EA}{br^2}(u'_{\theta} + u_r) - \frac{EI}{br^4}(u'''_{\theta} - u''''_r) + \rho h \Omega^2(2u'_{\theta} - u''_r) \\ + k_r u_r + \rho h(\ddot{u}_r - \dot{\Omega}u_{\theta} - 2\Omega\dot{u}_{\theta}) = f_r, \end{aligned} \quad (\text{A.8})$$

in the radial direction, where,  $E$  represents the Young's modulus, the area moment of inertial of the ring cross section about its neutral axis is denoted as  $I = bh^3/12$ , time derivatives are represented by  $(\dot{\quad})$  and spatial derivatives are denoted by  $(\quad)'$ .

### A.3 Natural Frequencies

Assuming periodic variations with time in  $u_r$  and  $u_{\theta}$ , the displacement components can be represented by series (Huang and Soedel, 1987):

$$u_r(\theta, t) = \sum_{n=-\infty}^{+\infty} A_n e^{j(n\theta + \omega_n t)}, \quad u_{\theta}(\theta, t) = \sum_{n=-\infty}^{+\infty} B_n e^{j(n\theta + \omega_n t)}, \quad (\text{A.9})$$

where  $n = 0, \pm 1, \pm 2, \dots$  and  $\omega_n$  represents the  $n^{\text{th}}$  natural frequency. Substituting Equation (A.9) in Equation (A.8) yields:

$$\begin{Bmatrix} M_{11} & M_{12} \\ M_{21} & M_{22} \end{Bmatrix} \begin{Bmatrix} A_n \\ B_n \end{Bmatrix} = \mathbf{0}, \quad (\text{A.10})$$

where,

$$M_{11} = \rho h \omega_n^2 - \left( \frac{K}{r^2} + \frac{D}{r^4} n^4 \right) - \rho h n^2 \Omega^2 - k_r, \quad (\text{A.11a})$$

$$M_{12} = j \left( 2 \rho h \Omega \omega_n - \frac{K}{r^2} n - \frac{D}{r^4} n^3 - 2 n \rho h \Omega^2 \right) + \underline{\underline{\rho h \dot{\Omega}}}, \quad M_{21} = -M_{12} \quad (\text{A.11b})$$

$$M_{22} = \rho h \omega_n^2 - n^2 \left( \frac{K}{r^2} + \frac{D}{r^4} \right) - \rho h n^2 \Omega^2 - k_\theta, \quad K = Eh, \quad D = Eh^3/12. \quad (\text{A.11c})$$

Calculating the determinant of Equation (A.10) and setting the determinant to zero, we can obtain the system characteristics equation:

$$\omega_n^4 + a_2 \omega_n^2 + a_1 \omega_n + a_0 = 0, \quad (\text{A.12})$$

where,

$$a_2 = -2\Omega^2(n^2 + 2) - K_1 - \frac{k_r + k_\theta}{\rho h}, \quad a_1 = \frac{4n\Omega K_1}{n^2 + 1} + 8n\Omega^3 + \underline{\underline{j(4\Omega\dot{\Omega})}}, \quad (\text{A.13})$$

$$a_0 = (n^4 - 4n^2)\Omega^4 + \frac{n^2(n^2 - 3)}{n^2 + 1}\Omega^2 K_1 + K_2 + \frac{n^2 D(n^2 k_\theta + k_r)}{\rho^2 h^2 r^4} + \frac{K(n^2 k_r + k_\theta)}{\rho^2 h^2 r^2} \quad (\text{A.14})$$

$$+ \frac{n^2 \Omega^2 (k_\theta + k_r)}{\rho h} + \frac{k_\theta k_r}{\rho^2 h^2} + \underline{\underline{\Omega^2 - j \left[ 4n\Omega^2 + \frac{2}{\rho h} \left( \frac{K}{r^2} + \frac{D}{r^4} n^3 \right) \right] \dot{\Omega}}}, \quad (\text{A.15})$$

$$K_1 = \frac{n^2 + 1}{\rho h r^2} \left( n^2 \frac{D}{r^2} + K \right), \quad K_2 = \frac{n^2 (n^2 - 1)^2}{r^6 \rho^2 h^2} DK. \quad (\text{A.16})$$

Equation (A.12) yields four natural frequencies, denoted as  $\omega_{nk}$ , where  $k = 1, 2, 3, 4$ . Two of the obtained frequencies correspond to the flexural or transverse vibration, and the other two correspond to the circumferential or extensional vibration of the ring. Here, the parameter  $n$

denotes the vibration mode for which the frequencies are derived. In the case that  $n = 0$ , the equation yields two extensional natural frequencies corresponding to the "breathing mode" and  $n = 1$  represents the rigid body motion of the ring.

Considering the natural frequency equations, the eigenfunctions can be written as:

$$u_r(\theta, t) = A_{nk}e^{j(n\theta + \omega_{nk}t)}, \quad u_\theta(\theta, t) = B_{nk}e^{j(n\theta + \omega_{nk}t)}, \quad n = 0, \pm 1, \pm 2, \dots, \quad k = 1, 2, 3, 4. \quad (\text{A.17})$$

Furthermore, the ratio between the amplitudes of circumferential vibration and flexural vibration is approximated by Huang and Soedel (1987) as:

$$j \frac{B_{nk}}{A_{nk}} = C_{nk} \approx \begin{cases} -1/n, & k = 1, 2 \quad (\text{Flexural vibrations}) \\ n, & k = 3, 4 \quad (\text{Circumferential vibrations}) \end{cases} \quad (\text{A.18})$$

Hence, mode shapes can be formulated using trigonometric functions as follows (see e.g., Huang and Soedel, 1987)

$$u_r(\theta, t) = \cos(n\theta + \omega_{nk}t), \quad u_\theta(\theta, t) = C_{nk} \sin(n\theta + \omega_{nk}t) \quad (\text{A.19})$$

## A.4 Normalized Equations of Motion

Considering the energy transfer between the mode configurations as shown in Figure 2.2, radial and circumferential displacements can be written according to the superposition principle as.

$$u_r(\theta, t) = \sum_{n=0}^{\infty} [q_1(t) \cos(n\theta) + q_2(t) \sin(n\theta)], \quad (\text{A.20a})$$

$$u_\theta(\theta, t) = \sum_{n=0}^{\infty} [q_3(t) \cos(n\theta) + q_4(t) \sin(n\theta)]. \quad (\text{A.20b})$$

Substituting Equations (A.20) into Equations (A.7) and (A.8) and applying the orthogonality of the intermediate trigonometric functions yields the equations of motion. Following the derivation process using generalized coordinates and substituting Equations (A.20) in Equations (A.7) and (A.8) yields:

$$\sum_{n=0}^{\infty} [D_{1n}(t) \cos(n\theta) + D_{2n}(t) \sin(n\theta)] = f_r(\theta, t), \quad (\text{A.21a})$$

$$\sum_{n=0}^{\infty} [D_{3n}(t) \cos(n\theta) + D_{4n}(t) \sin(n\theta)] = f_\theta(\theta, t). \quad (\text{A.21b})$$

Here,

$$D_{1n}(t) = \rho h(\ddot{q}_1 - 2\Omega\dot{q}_3) - \rho h\dot{\Omega}q_3 + \tilde{c}q_1 + n\tilde{a}q_4, \quad (\text{A.22a})$$

$$D_{2n}(t) = \rho h(\ddot{q}_2 - 2\Omega\dot{q}_4) - \rho h\dot{\Omega}q_4 + \tilde{c}q_2 - n\tilde{a}q_3, \quad (\text{A.22b})$$

$$D_{3n}(t) = \rho h(\ddot{q}_3 + 2\Omega\dot{q}_1) + \rho h\dot{\Omega}q_1 - n\tilde{a}q_2 + \tilde{b}q_3, \quad (\text{A.22c})$$

$$D_{4n}(t) = \rho h(\ddot{q}_4 + 2\Omega\dot{q}_2) + \rho h\dot{\Omega}q_2 + n\tilde{a}q_1 + \tilde{b}q_4, \quad (\text{A.22d})$$

with

$$\tilde{a} = n^2 \frac{EI}{r^4} + \frac{EA}{r^2} + 2\rho A\Omega^2, \quad (\text{A.23a})$$

$$\tilde{b} = n^2 \left( \frac{EI}{r^4} + \frac{EA}{r^2} + \rho A\Omega^2 \right) + k_\theta, \quad (\text{A.23b})$$

$$\tilde{c} = n^4 \frac{EI}{r^4} + \frac{EA}{r^2} + n^2 \rho A\Omega^2 + k_r. \quad (\text{A.23c})$$

Applying the orthogonality of trigonometric functions to Equation (A.21a),

$$\begin{aligned}
& \int_0^{2\pi} f_r(\theta, t) \cos(n\theta) d\theta \\
&= \int_0^{2\pi} \sum_{n=0}^{\infty} [D_{1n}(t) \cos(n\theta) + D_{2n}(t) \sin(n\theta)] \cos(n\theta) d\theta \\
&= \sum_{n=0}^{\infty} \left[ \int_0^{2\pi} D_{1n}(t) \cos^2(n\theta) d\theta + \int_0^{2\pi} D_{2n}(t) \sin(n\theta) \cos(n\theta) d\theta \right] \\
&= \sum_{n=0}^{\infty} \pi D_{1n}(t).
\end{aligned} \tag{A.24}$$

Substituting Equation (A.22a) into Equation (A.24) yields the first equation of motion:

$$(\ddot{q}_1 - 2\Omega\dot{q}_3) - \dot{\Omega}q_3 + \frac{1}{\rho h}(\tilde{c}q_1 + n\tilde{a}q_4) = \frac{1}{\pi\rho h} \int_0^{2\pi} f_r(\theta, t) \cos(n\theta) d\theta. \tag{A.25}$$

The second equation of motion can be obtained by applying a similar procedure to Equation (A.21b).

# Appendix B

## Matlab Codes

### B.1 Introduction

In this Chapter, the computer codes used for time response simulation and stability analysis are presented in detail. Matlab programming language was used in the present research in order to simplify the algorithm implementation using matrices. However, other programming languages may also be used for the developed algorithm.

### B.2 Time Series Simulation

The following code implements the Euler and the higher order Milstein numerical schemes in order to simulate the free vibration time response of the gyroscopic system to an initial disturbance:

```
% Ring Parameters

E = 210e9; ro = 8800; r = 500e-6; h = 12.5e-6; b = 30e-6;
A = b*h; I = b*h^3/12;
a = 4*E*I/r^4 + E*A/r^2;
b = 4*(E*I/r^4 + E*A/r^2);
c = 16*E*I/r^4 + E*A/r^2;
k1 = (b*c - 4*a^2)/(ro*A*(a + b));
k2 = (4*(b + c - 4*a))/(a + b) - (6*(b*c - 4*a))/((a + b)^2);
gamma = (b+4*a)/(2*(a + b));

% Initialization
```

```

N = 150000; % Number of steps
h = 0.009/N; % time step
intensity = 199; % noise intensity
zeta = 0.14; % damping ratio
t = [0:h:(h*N)]'; % store time
z = [1e-5,0,0,0]'; % initial condition
results = z;

% Generate Brownian Motion

rng('default'); % Initialize random number generator

DW = normrnd(0,1,1,N)*sqrt(h);
W = cumsum(DW); W = [0,W];
dW = diff(W);

% In order to study the effects of angular rate on
% system response, the natural frequencies can be
% calculated via the eigenvalue equation as follows

p = 4*(2*pi)^2*gamma^2;
s = k1 + k2*(2*pi)^2;
NaturalFrequencies = roots([1 0 (p+2*s) 0 s^2]);

w01 = imag(NaturalFrequencies(1)); % 1st natural frequency
w02 = imag(NaturalFrequencies(3)); % 2nd natural frequency

% In order to study the effects of mass mismatch on
% system response, the natural frequencies can be
% calculated via the eigenvalue equation as follows
%
% mm=0.1;
% p=4*(2*pi)^2*gamma^2;
% s=k1+k2*(2*pi)^2;
% NaturalFrequencies=roots([1+mm 0 (p+(2+mm)*s) 0 s^2])
%
% w01=imag(NaturalFrequencies(1)) % 1st natural frequency
% w02=imag(NaturalFrequencies(3)) % 2nd natural frequency

% Simulate time response using Milstein scheme

tic
for i = 1:1:N

```



```

% Generating time varying omega

tf = 0.005;
max_omega = 2*pi;
if t(i) <= tf % smoothly varying omega
    omega = (-2*max_omega/tf^3)*t(i).^3
        + (3*max_omega/tf^2)*t(i).^2;
else
    omega = max_omega;
end

% Calculating drift and diffusion matrices

a=[0, 1, 0, 0;
   -k1-k2*omega^2, -2*zeta*w01, 0, 2*gamma*omega;
   0, 0, 0, 1;
   0, -2*gamma*omega, -k1-k2*omega^2, -2*zeta*w02];

b=[0,0,0,0;
   -2*k2*intensity*omega, 0, 0, 2*intensity*gamma;
   0, 0, 0, 0;
   0, -2*intensity*gamma, -2*k2*intensity*omega, 0];

btotal = b*z;
atotal = a*z;

% Applying Milstein scheme

for u = 1:4
    sum = 0;
    for y = 1:4
        sum = sum + btotal(y,1)*b(u,y);
    end

    xx(u,1) = z(u) + atotal(u)*h + btotal(u)*dW(1,i)
        + 0.5*(sum)*((dW(1,i))^2 - h);

    z(u) = xx(u);
end

results = [results, xx];
end

leg1 = ['\mu=' num2str(intensity)];
leg2 = ['\zeta=' num2str(zeta)];

```

```

leg = [leg1 leg2];

x = results(3,:);
plot(t,x,'r')
legend(leg);
hold on

toc

% Simulating time response using Euler scheme

% Reinitializing the state variables

z = [1e-5,0,0,0]'; % initial condition
results = z;

tic
for i = 1:1:N

    % Generating time varying omega

    tf = 0.005;
    max_omega = 2*pi;
    if t(i) <= tf % smoothly varing omega
        omega = (-2*max_omega/tf^3)*t(i).^3
            + (3*max_omega/tf^2)*t(i).^2;
    else
        omega = max_omega;
    end

    % Calculating drift and diffusion matrices

    a=[0, 1, 0, 0;
        -k1-k2*omega^2, -2*zeta*w01, 0, 2*gamma*omega;
        0, 0, 0, 1;
        0, -2*gamma*omega, -k1-k2*omega^2, -2*zeta*w02];

    b=[0,0,0,0;
        -2*k2*intensity*omega, 0, 0, 2*intensity*gamma;
        0, 0, 0, 0;
        0, -2*intensity*gamma, -2*k2*intensity*omega, 0];

    btotal = b*z;
    atotal = a*z;

```

```

% Applying Euler scheme

xx =z+atotal*h+btotal*dW(1,i);

z=xx;
results=[results ,xx];
end

x = results(3,:);
plot(t,x);
legend(leg);

xlabel('Time (s)')
ylabel('Amplitude (m)')
toc

```

## B.3 Largest Lyapunov Exponent Calculation

Having the time response, stability of the system may be analyzed considering rate of growth or decay of the system response. The Largest Lyapunov Exponent method is developed in order to assess the rate of growth or decay of a system response. This method requires a number of initial parameters including the time delay and the mean period which contain information about the nature of the response. These parameters are later used in order to reduce the number of calculation and increase the accuracy of the algorithm.

### B.3.1 Calculating Mutual Average Information

The following code block demonstrates the calculation process for the Mutual Average Information:

```

function v=mai(x,lag)
%Syntax: v=mai(x,lag)
%-----
%
% Calculates the mutual average information of
% a time series x for some time lag.
%
% v is the the value of the mutual average information.
% x is the time series.
% lag is the time lag.
%
% Author: Alexandros Leontitsis
% Institute of Mathematics and Statistics

```

```

% University of Kent at Canterbury

if nargin<1 | isempty(x)==1
    error('You should provide a time series. ');
else
    % x must be a vector
    if min(size(x))>1
        error('Invalid time series. ');
    end
    x=x(:);
    % n is the time series length
    n=length(x);
end
display('check')
if nargin<2 | isempty(lag)==1
    lag=0:min(n/2-1,20);
else
    % lag must be a vector
    if min(size(lag))>1
        error('The time lag must be a scalar or a vector. ');
    end
    % lag must contain integers
    lag=round(lag);
    % lag values must be between 0 and n/2-1
    lag=lag(find(lag>=0 & lag<n/2));
    % lag must not be empty
    if isempty(lag)==1
        error('You must give another set of values for lag. ')
    end
end
display('check')

% The mutual average information
x=x-min(x);
x=x/max(x);
display('check')
for i=1:length(lag)
    i
    % Define the number of bins
    k=floor(1+log2(n-lag(i))+0.5);

    % If the time series has no variance then the MAI is 0
    if var(x,1)==0

```

```

        v(i)=0;
    else
        v(i)=0;
        for k1=1:k
            for k2=1:k
                ppp=find((k1-1)/k<x(1:n-lag(i)) & x(1:n-lag(i))<=k1/k ...
                    & (k2-1)/k<x(1+lag(i):n) & x(1+lag(i):n)<=k2/k);
                ppp=length(ppp);
                px1=find((k1-1)/k<x(1:n-lag(i)) & x(1:n-lag(i))<=k1/k);
                px2=find((k2-1)/k<x(1+lag(i):n) & x(1+lag(i):n)<=k2/k);
                if ppp>0
                    ppp=ppp/(n-lag(i));
                    px1=length(px1)/(n-lag(i));
                    px2=length(px2)/(n-lag(i));
                    v(i)=v(i)+ppp*log2(ppp/px1/px2);
                end
            end
        end
    end
end
end
end
end

```

### B.3.2 Calculating Mean Period

System response to an initial disturbance exhibits a constant frequency owing to the constant natural frequency of the system. The system natural frequency can be used for estimation of the mean period of system response. However, the following algorithm calculates the mean period of a system based on the time response, eliminating the need for any additional information about the system. Furthermore, another advantage of this algorithm is calculation of mean period which accounts for the variations in natural frequency due to additional noise.

```
function [meanp] = meanperiod(x)
```

```
% Calculates and returns mean period of time series 'x'
% By : Soroush Arghavan
```

```
buf = zeros(1,length(x));
i = 1;
j = 1;
trap = 1;
```

```
while i <= numel(x) - 1
    while x(i) <= x(i+1)
        buf(j) = i;
```

```

        if i == numel(x) - 1
            break;
        end

        i = i+1;
        trap = 0;
    end

    if buf(j) ~= 0
        j = j+1;
    end

    if trap == 1;
        i = i+1;
    end

    trap = 1;

    if i == numel(x)-1
        break
    end
end

for i = 1:numel(buf)-1
    if buf(i+1) ~= 0
        diff(i) = buf(i+1) - buf(i);
    end
end

meanp=round(mean(diff));
end

```

### B.3.3 Calculating Lyapunov Exponents

Having the necessary initial information, the Lyapunov characteristic exponents of the system time response can be calculated and can be used to determine the Largest Lyapunov Exponent of the response:

```

function d = lyarosenstein(x,m,tao , meanperiod , maxiter)
% d:divergence of nearest trajectoires
% x: signal
% tao:time delay
% m:embedding dimension

```

```

N=length(x);
M=N-(m-1)*tao;
Y=psr_deneme(x,m,tao);

for i=1:M

    x0=ones(M,1)*Y(i,:);
    distance=sqrt(sum((Y-x0).^2,2));
    for j=1:M
        if abs(j-i)<=meanperiod
            distance(j)=1e10;
        end
    end
    [neardis(i) nearpos(i)]=min(distance);
end

for k=1:maxiter

    maxind=M-k;
    evolve=0;
    pnt=0;
    for j=1:M
        if j<=maxind && nearpos(j)<=maxind
            dist_k=sqrt(sum((Y(j+k,:)-Y(nearpos(j)+k,:)).^2,2));
            if dist_k~=0
                evolve=evolve+log(dist_k);
                pnt=pnt+1;
            end
        end
    end
    if pnt > 0
        d(k)=evolve/pnt;
    else
        d(k)=0;
    end

end

%figure
%plot(d)

%% LLE Calculation
%fs=2000;%sampling frequency
%tlinear=15:78;
%F = polyfit(tlinear,d(tlinear),1);

```

```

%lle = F(1)*fs

function Y=psr_deneme(x,m,tao ,npoint)
%Phase space reconstruction
%x : time series
%m : embedding dimension
%tao : time delay
%npoint : total number of reconstructed vectors
%Y : M x m matrix
% author:"Merve Kizilkaya"
N=length(x);
if nargin == 4
    M=npoint;
else
    M=N-(m-1)*tao;
end

Y=zeros(M,m);

for i=1:m
    Y(:,i)=x((1:M)+(i-1)*tao)';
end

```

### B.3.4 Finding Largest Lyapunov Exponent of The Simulated Time Series

The following code is applied to the calculated system time response in Section B.2 using the functions defined in Appendix B.3.1 to B.3.3 in order to obtain the Largest Lyapunov Exponent of the time response:

```

xm=results(3,:);
x=xm(1:44000);
plot(t(1:44000),x,'r')
hold on

tao=0:1:size(x,2)/60-1;
    display('calculating AMI')
    y=mai(x,tao);
    %plot(tao,y)

    for i=2:1:size(y,2)-1
        if (y(i-1)>=y(i) && y(i)<=y(i+1) );
            tdelay=tao(1,i); % the first minimum

```



```
                break;
            end
        end

        mperiod = meanperiod(x);
        display('finding LLE')

        %divergence of trajectories

        d = lyarosenstein(x,5,tdelay,mperiod,44000);

        %sampling frequency

        fs=N/h;
        tlinear=10:length(find(d))-50;
        F = polyfit(tlinear,d(tlinear),1);
        LLEm = F(1)*fs
    toc
```

# Appendix C

## Experimental Setup

The experimental setup consists of a long C1095 blue-tempered cylindrical McMaster-Carr Supply Company steel shell installed on an Ideal Aerosmith 1291BR Precision Single-axis Rate Table. The top part of the shell is fixed using lightweight thin tape in order to maintain the shell in a suspending position while minimizing the effects of added stiffness and mode shapes caused by the tapes. This allows the bottom part of the cylinder to deform and hence mimic a thin free-standing ring. Figures C.1 and C.2 show the details of the experimental setup.

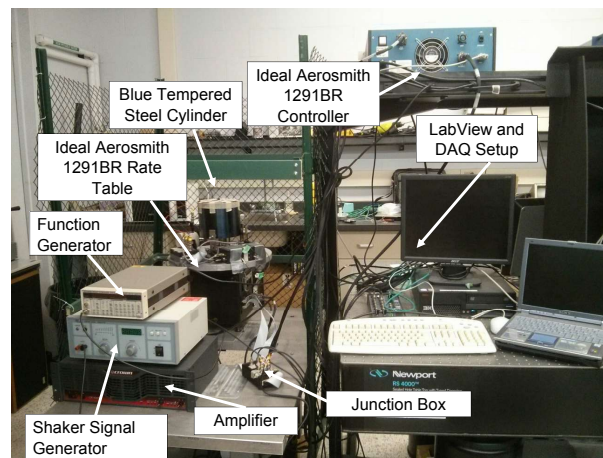


Figure C.1: Experimental setup.

Two APW Company EM075-12-122 electromagnets are employed as shown in Figure C.3 for the purpose of excitation of the ring. The electromagnets are placed along the symmetry line of the ring and are set to operate in phase relative to each other in order to force vibration in the

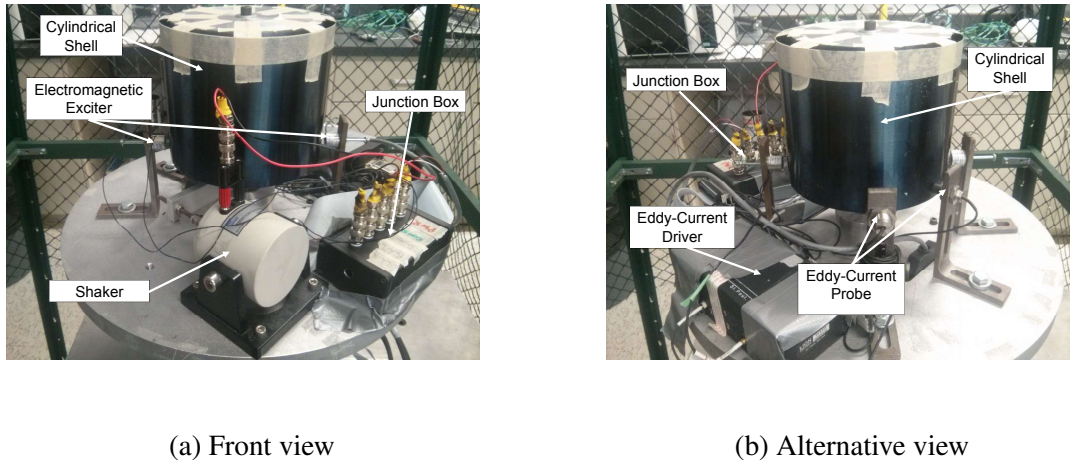


Figure C.2: Experimental setup close-up

second flexural mode.

Measurements are made possible via two Lion Precision Eddy current probes, displayed in Figure C.4 and connected to an ECL134 Eddy current sensor driver. LabView software is used for data analysis.

Slip rings in the rate table enable the input signal to the exciters and the shaker and sensor output signal as well as low-voltage power for the driver to pass through the rotating rate table to external devices. In order to facilitate the operation and maintenance of the system, two junction boxes were developed for separation of signals on both the internal and external connections of the rate table. The junction boxes divide the 37-pin connections into more manageable, plug and play individual BNC connections. Figure C.5 shows the external junction box used for separation and combination of signals between peripheral devices and the rate table. In order to clarify the experimental setup and signal flow between the devices, the block diagram and a schematic view of the setup are shown in Figures C.6 and C.7, respectively. The system wiring was refined with both single-sensor and dual-sensor operation in mind. Figures C.8 and C.9 display the wiring schematics for single-sensor and dual-sensor operation, respectively with the pin layout of the connectors summarized in Tables C.1, C.2 and C.3.



Figure C.3: Configuration of an electromagnetic exciter.

Finally, the sensor measurement data is sent to LabView for monitoring and analysis. A LabView script has been developed for reading the data from the data acquisition (DAQ) card. The data is then filtered using a band-pass filter to remove low-frequency and high-frequency noise on the two extremes of the measurement spectrum. The developed script is shown in Figures C.10 and C.11.



Figure C.4: Configuration of the Eddy-Current probes.

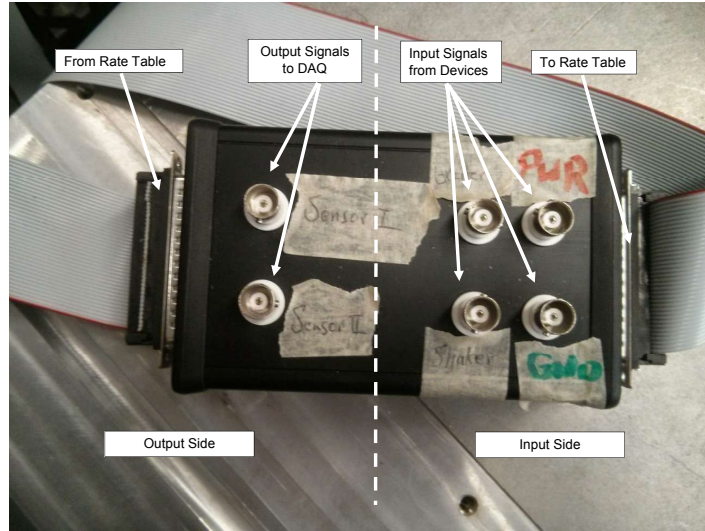


Figure C.5: Layout of a junction box.

## C.1 Startup Procedure

1. Determine whether single-sensor or dual-sensor operation is required for the experiment.
2. Use the Phoenix Contact 2938756 DC Power Supply for single-sensor operation and the Total Power International TPSPU45E-210 switching power supply for dual-sensor operation.
3. Use Lion Precision ECL100 for single-sensor operation and ECL134 for dual-sensor operation.
4. Connect the probe(s) to the Eddy-Current driver.
5. Plug in the necessary BNC connections i.e. exciter, power and sensors on both junction boxes and make sure the unused BNC connections are disconnected. **IMPORTANT NOTE: MAKE SURE THAT THE POWER AND GROUND CONNECTIONS ARE CONNECTED CORRECTLY BEFORE MOVING FURTHER. INCORRECT POWER AND GROUND CONNECTIONS CAN CAUSE SERIOUS DAMAGE TO EQUIP-**

## MENT AND USER.

6. Enable function generation and switch on the amplifier.
7. Switch on the power supply and enable the data acquisition script.
8. At this point the cylindrical shell should be excited and the sensor data should be visible.
9. Turn on the KCF PA5100 Signal Generator in case the shaker is used in the experiment. Otherwise, keep the generator off. Note: Using any other type of signal generation or amplifier device other than the designated device may result in incorrect operation of the shaker.
10. Double check the rate table connections to make sure there are no faulty connections.
11. Switch on the Ideal Aerosmith 1291BR Controller using the circuit breaker switch located on the back of the controller and the switch on button located on the front. IMPORTANT NOTE: Make sure that the "servo" switch is "OFF" and the physical brake on the rate table is engaged before turning the controller on.
12. Make sure that the emergency brake knob on the controller is disengaged.
13. Disengage the physical brake located on the side of the ring table.
14. Switch "servo" to "ON". The green "active" LED should be visible on the controller. If the red "brake engaged" LED is on, make sure that the physical brake is fully disengaged.
15. Use the designated Ideal Aerosmith application to control the rate table.

### **C.1.1 Rate Table Initial Startup**

In order to ascertain safe operation of the rate table and preventing damage to the equipment of injury of personnel, the following initial startup procedure is recommended:

IMPORTANT NOTE: BE PREPARED TO USE THE EMERGENCY BRAKE KNOB LOCATED ON THE IDEAL AEROSMITH 1291BR CONTROLLER AT ALL TIMES. DO NOT LEAVE THE DEVICE UNATTENDED WHEN ON.

1. Type SRV1 in the command input section to turn the software controller on.
2. Use DIR1 for clockwise and DIR0 for counterclockwise rotation.
3. Set the maximum allowable velocity using MXV command, e.g. MXV500 for maximum  $500^\circ/s$ .
4. Velocity and acceleration for the closed loop position control function can be set using VEL and ACL commands. These steps can be ignored for constant-speed angular rotation. Use the VEL command to set the velocity for closed-loop position control, e.g. VEL50 for  $50^\circ/s$  maximum angular velocity in the trapezoidal velocity function.
5. Set the acceleration for the trapezoidal velocity function using the ACL command, e.g. ACL50 for  $50^\circ/s^2$ .
6. Type PPO in the command input. The software should return the current angular position of the table.
7. Rotate the device  $180^\circ$  by hand.
8. Type PPO in the command input. The new position value should be different than the previous value by  $180^\circ$ .
9. Use RMO to move the table to a new position relative to the current location and check the accuracy using PPO and comparing with the previous value, e.g. RMO10 moves the table  $10^\circ$  in the defined direction.
10. Use the JOG command to start rotation with constant angular velocity. e.g. JOG360 results in the table rotating at  $360^\circ/s$  or 1 Hz.

11. Verify the current angular velocity by using the PVE command.
12. Stop the system at any point by using the STO command.

## **C.2 Shutdown Procedure**

1. Stop the rate table using the STO command.
2. Switch "servo" to "OFF" and make sure the "active" light is off.
3. Turn the Ideal Aerosmith 1291BR Controller off using the front switch and the circuit breaker located on the back.
4. Engage the physical brake located on the side of the ring table.
5. Turn the driver power supply off.
6. Turn the signal generators and the amplifier off.
7. Unplug the devices.
8. Disconnect all BNC connections.



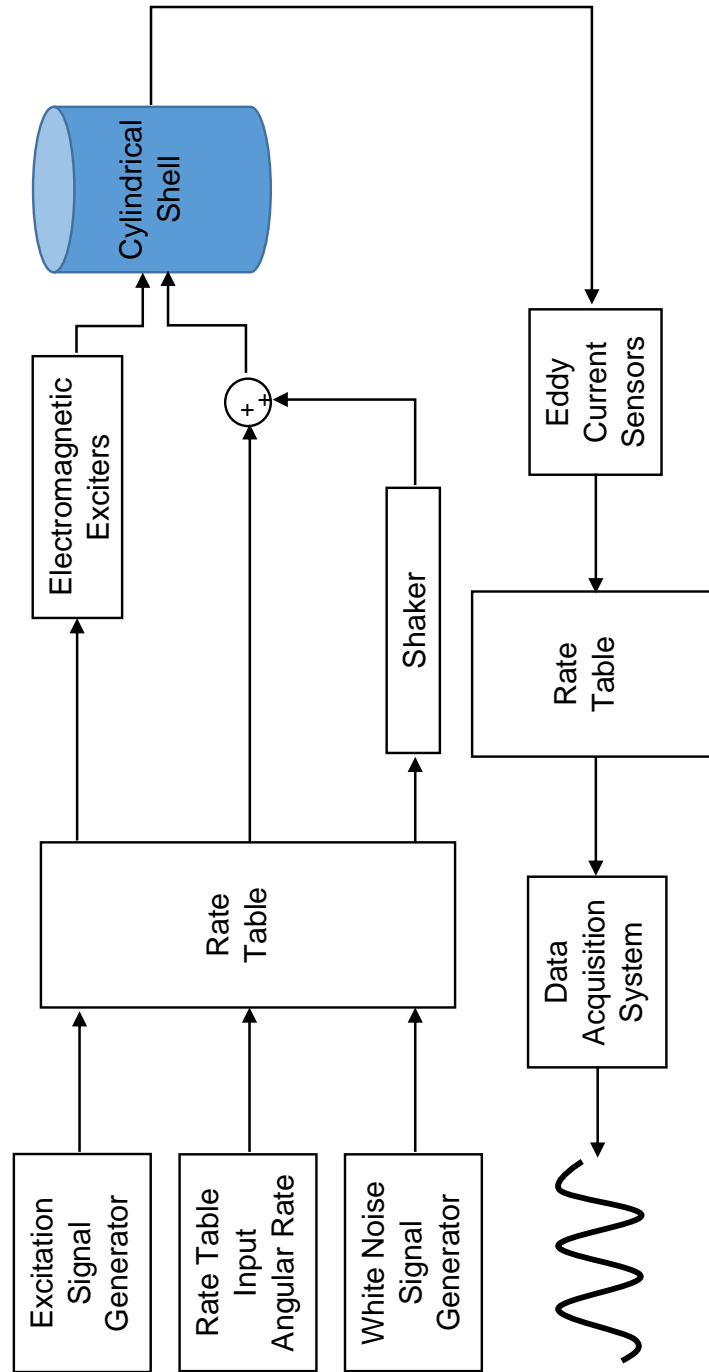


Figure C.6: Block diagram representation of the experimental setup.

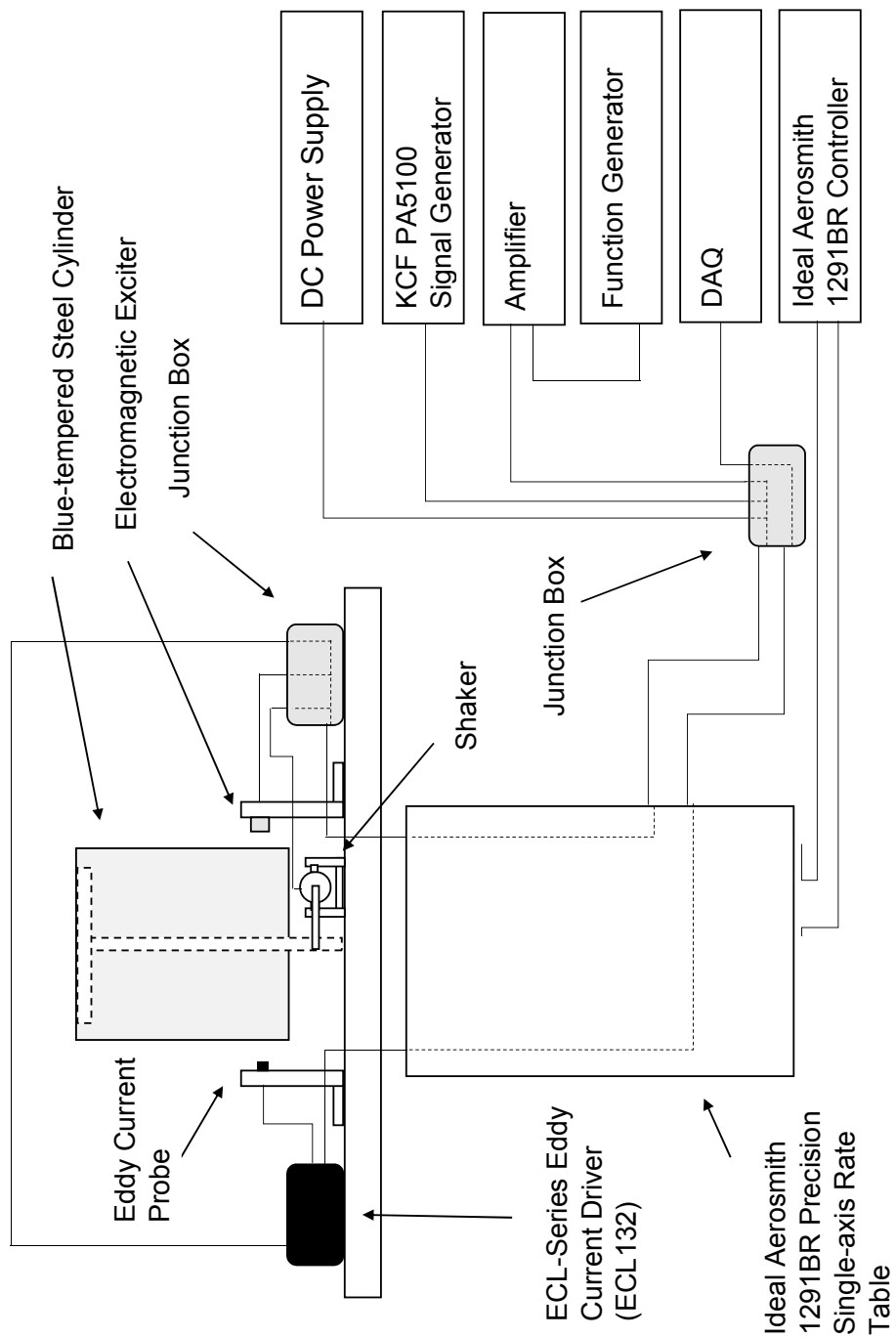


Figure C.7: Schematic view of the experimental setup.





Pin	Description	Color
1	Not Connected	Not Connected
2	Not Connected	Not Connected
3	Not Connected	Not Connected
4	Not Connected	Not Connected
5	Ground	White
6	Shaker +	Green (Outer Wire)
7	Power -	Black
8	Power +	Red
9	Shaker -	Blue
10	Exciter +	Green (Inner Wire)
11	Exciter -	Orange/Yellow/Brown
12	Not Connected	Not Connected
13	Not Connected	Not Connected
14	Not Connected	Not Connected
15	Not Connected	Not Connected
16	Not Connected	Not Connected
17	Not Connected	Not Connected
18	Not Connected	Not Connected
19	Not Connected	Not Connected
20	Not Connected	Not Connected
21	Not Connected	Not Connected
22	Not Connected	Not Connected
23	Not Connected	Not Connected
24	Not Connected	Not Connected
25	Not Connected	Not Connected
26	Not Connected	Not Connected
27	Not Connected	Not Connected
28	Not Connected	Not Connected
29	Not Connected	Not Connected
30	Not Connected	Not Connected
31	Not Connected	Not Connected
32	Not Connected	Not Connected
33	Not Connected	Not Connected
34	Not Connected	Not Connected
35	Not Connected	Not Connected
36	Not Connected	Not Connected
37	Not Connected	Not Connected

Table C.1: Input 37-pin connection pinout (Rate table J100 and J101)

Pin	Description	Color
1	Not Connected	Not Connected
2	Not Connected	Not Connected
3	Not Connected	Not Connected
4	Sensor 2 +	Brown/Orange
5	Sensor 2 -	Green
6	Ground	White
7	Sensor 1 -	Black
8	Sensor 1 +	Red
9	Not Connected	Not Connected
10	Not Connected	Not Connected
11	Not Connected	Not Connected
12	Not Connected	Not Connected
13	Not Connected	Not Connected
14	Not Connected	Not Connected
15	Not Connected	Not Connected
16	Not Connected	Not Connected
17	Not Connected	Not Connected
18	Not Connected	Not Connected
19	Not Connected	Not Connected
20	Not Connected	Not Connected
21	Not Connected	Not Connected
22	Not Connected	Not Connected
23	Not Connected	Not Connected
24	Not Connected	Not Connected
25	Not Connected	Not Connected
26	Not Connected	Not Connected
27	Not Connected	Not Connected
28	Not Connected	Not Connected
29	Not Connected	Not Connected
30	Not Connected	Not Connected
31	Not Connected	Not Connected
32	Not Connected	Not Connected
33	Not Connected	Not Connected
34	Not Connected	Not Connected
35	Not Connected	Not Connected
36	Not Connected	Not Connected
37	Not Connected	Not Connected

Table C.2: Output 37-pin connection pinout (Rate table J102 and J103)

Pin	Description	Color
1	Sensor 1 +	Red
2	Sensor 2 +	Brown/Orange
3	Not Connected	Not Connected
5	Not Connected	Not Connected
6	Not Connected	Not Connected
7	Not Connected	Not Connected
8	Not Connected	Not Connected
9	Sensor 1 -	Black
10	Sensor 2 -	Green
11	Not Connected	Not Connected
12	Not Connected	Not Connected
13	Not Connected	Not Connected
14	Not Connected	Not Connected
15	Ground	White

Table C.3: ECL134 15-pin output connection pinout

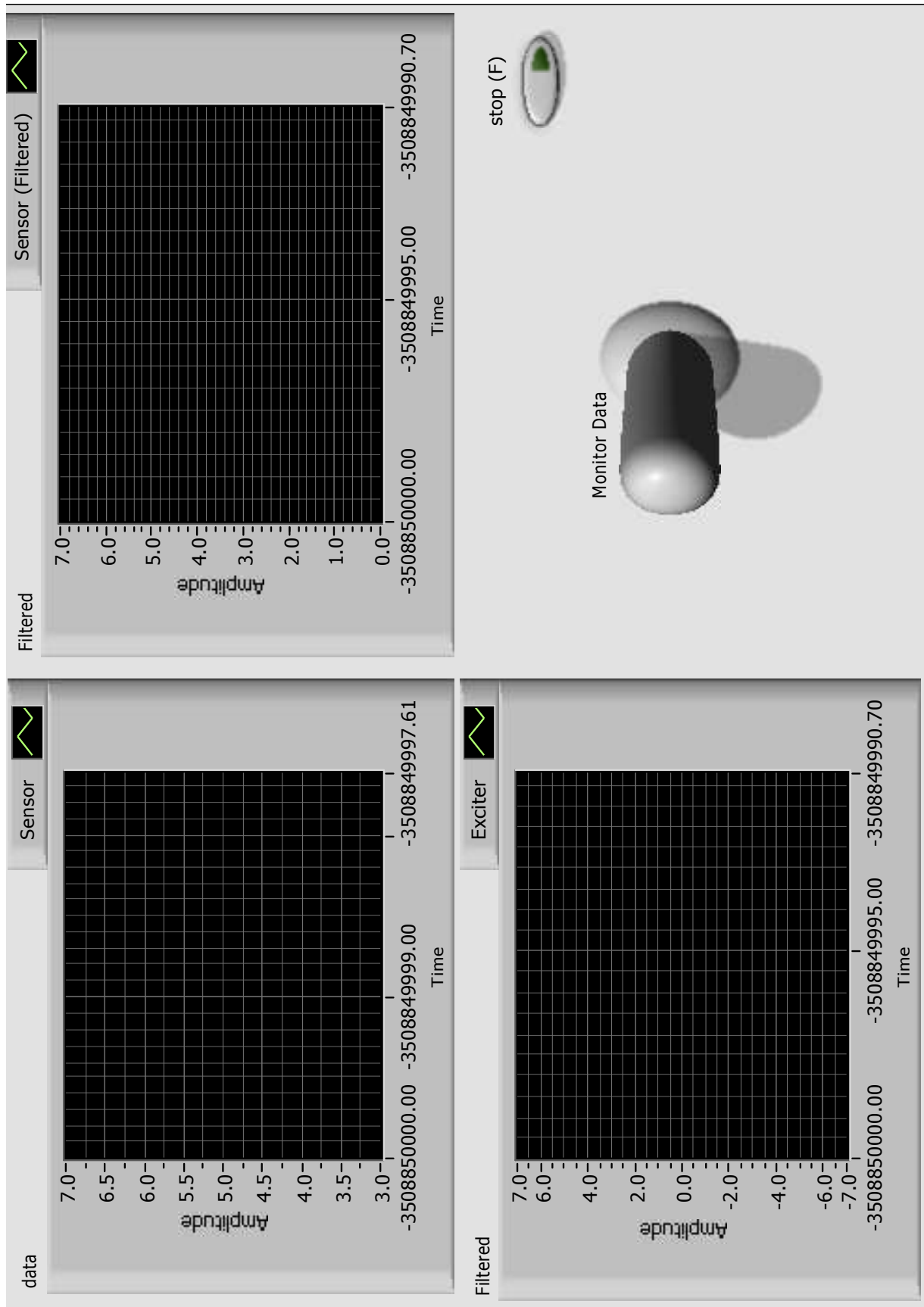


Figure C.10: Front panel of the LabView script.



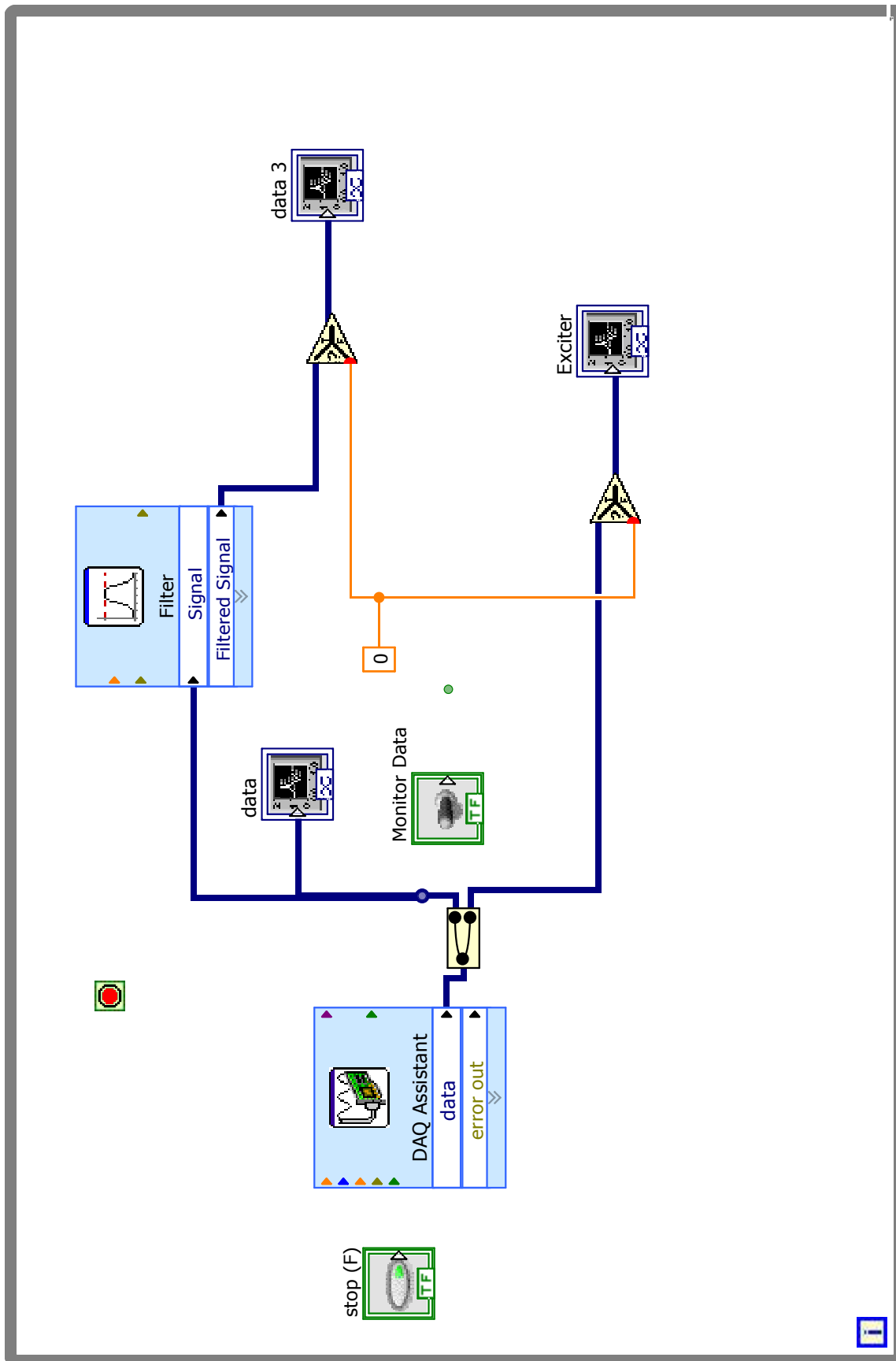


Figure C.11: Block diagram view of the LabView script.

# Curriculum Vitae

**Name:** Soroush Arghavan

**Post-Secondary Education and Degrees:** The University of Western Ontario  
London, Canada  
2013 - 2015 M.E.Sc

Shiraz University  
Shiraz, Iran  
2009 - 2013 B.Sc.

**Honours and Awards:** Western Graduate Research Scholarship (WGRS)  
2013-2015

**Related Work Experience:** Research Assistant  
The University of Western Ontario  
2013 - 2015

Teaching Assistant  
The University of Western Ontario  
2013 - 2015

Teaching Assistant  
Shiraz University  
2010 - 2012

## Publications:

Arghavan S, Asokanthan S F, Bognash M, Stability of Ring-type MEMS Gyroscopes subjected to Stochastic Angular Speed Fluctuation. *Journal of Probabilistic Engineering Mechanics* (Under Review)

Arghavan S, Bognash M, Asokanthan S F. *Stochastic Dynamics and Stability of a Class of MEMS Gyroscopes, Proceeding of the 25th Canadian Congress of Applied Mechanics (CAN-CAM 2015)*, Pages 820-823, London, Canada

Arghavan S, Akbari M. *A New Design for the Improvement of Uniform Cooling in Air-Cooled Li-Ion Battery Stacks, Proceeding of the 25th Canadian Congress of Applied Mechanics (CAN-CAM 2015)*, Pages 739-743, London, Canada